Electrons from decays of open charm and beauty hadrons in p-Pb collisions at $\sqrt{s_{\mathrm{NN}}} = 5.02\,\mathrm{TeV}$

Elektronen aus Zerfällen von offenen Charm- und Beauty-Hadronen in p-Pb Kollisionen bei $\sqrt{s_{\mathrm{NN}}} = 5.02\,\mathrm{TeV}$
Zur Erlangung des Grades eines Doktors der Naturwissenschaften (Dr. rer. nat.)
genehmigte Dissertation von M.Sc. Jan Wagner aus Groß-Gerau
Tag der Einreichung: 12.07.2016, Tag der Prüfung: 17.10.2016
Darmstadt 2016 — D 17

1. Gutachten: Prof. Dr. Tetyana Galatyuk
2. Gutachten: Priv. Doz. Dr. Anton Andronic

TECHNISCHE
UNIVERSITÄT
DARMSTADT

Fachbereich Physik
Institut für Kernphysik

Electrons from decays of open charm and beauty hadrons in p-Pb collisions at $\sqrt{s_{\mathrm{NN}}} = 5.02\,\mathrm{TeV}$
Elektronen aus Zerfällen von offenen Charm- und Beauty-Hadronen in p-Pb Kollisionen bei $\sqrt{s_{\mathrm{NN}}} = 5.02\,\mathrm{TeV}$

Genehmigte Dissertation von M.Sc. Jan Wagner aus Groß-Gerau

1. Gutachten: Prof. Dr. Tetyana Galatyuk
2. Gutachten: Priv. Doz. Dr. Anton Andronic

Tag der Einreichung: 12.07.2016
Tag der Prüfung: 17.10.2016

Darmstadt 2016 — D 17

Bitte zitieren Sie dieses Dokument als:
URN: urn:nbn:de:tuda-tuprints-57101
URL: http://tuprints.ulb.tu-darmstadt.de/5710

Für meine Eltern Ute und Gerald
und meine Schwester Maike

Abstract

Charm and beauty quarks serve as a probe to study the deconfined medium of a quark-gluon plasma observed in A-A collisions. Due to their large mass they are produced in the first moments of the collision and interact with the expanding medium. Cold nuclear matter effects such as the modification of the nuclear Parton Distribution Functions in the Pb nuclei, parton momentum (k_{T}) broadening from soft scattering processes and initial- and final-state parton energy loss play a role in nuclear collisions. These effects can be studied by a reference measurement in p-A collisions, where an extended medium is not believed to be formed.

In this work the measurement of the production of electrons from semi-leptonic decays of heavy-flavor hadrons as function of the transverse momentum in p-Pb collisions at $\sqrt{s_{\mathrm{NN}}} = 5.02\,\mathrm{TeV}$ with ALICE at the LHC is presented. The measurement of electrons from heavy-flavor hadron decays requires a precise determination of the electron background. For the first time in this kind of measurement with ALICE the main contribution to the electron background is estimated by tagging electrons from $e^{+}e^{-}\gamma$ Dalitz decays and γ-conversions, leading to a substantial reduction of the relative systematic uncertainties compared to previous measurements in pp collisions. A reference measurement for pp collisions at $\sqrt{s} = 5.02\,\mathrm{TeV}$ was interpolated from measurements in pp collisions at $\sqrt{s} = 2.76\,\mathrm{TeV}$ and $\sqrt{s} = 7\,\mathrm{TeV}$. The determined nuclear modification factor of electrons measured in the p_{T}-range $0.5 < p_{\mathrm{T}} < 8\,\mathrm{GeV}/c$ and rapidity range $-1.065 < y_{\mathrm{cms}} < 0.135$ suggests binary-scaling of the production cross-section measured in p-Pb collisions. The result for the R_{pPb} suggests small cold nuclear matter effects for electrons from heavy-flavor hadron decays in agreement with predictions from different model calculations.

An investigation of the multiplicity dependence of heavy-flavor production leads to linear increase of the self-normalized yields of electrons from heavy-flavor hadron decays as function of the charged-particle multiplicity estimated at mid-rapidity and backward rapidity in p-Pb collisions at $\sqrt{s_{\mathrm{NN}}} = 5.02\,\mathrm{TeV}$. The self-normalized yields show no p_{T}-dependence as function of the multiplicity, which indicates small or no differences between the charm and beauty production as function of multiplicity.

Zusammenfassung

Charm- und Beautyquarks können benutzt werden um das Quark-Gluon Plasma, das in A-A Kollisionen beobachtet wird, zu untersuchen. Wegen ihrer großen Masse enstehen sie in den ersten Momenten einer Kollision und interagieren mit dem sich ausdehnenden Medium. “Kalte-Materie Effekte”, wie zum Beispiel eine Modifizierung der Kern-Partonenverteilungsfunktionen, eine Vergrößerung der relativen Breite des Parton-Transversalimpulses (k_{T}) durch weiche Stoßprozesse sowie Energieverlust des Partons im Eingangs- und Ausgangszustand spielen in Kollisionen von Kernen eine Rolle. Diese Effekte können durch eine Referenzmessung in p-A Kollisionen untersucht werden, für die angenommen wird, dass in diesen kein ausgedehntes Medium entsteht.

Diese Arbeit beschäftigt sich mit der Produktion von Elektronen aus semileptonischen Zerfällen von Charm- und Beautyhadronen als Funktion des Tansversalimpulses in p-Pb Kollisionen bei einer Schwerpunktsenergie von $\sqrt{s_{\mathrm{NN}}} = 5.02\,\mathrm{TeV}$, gemessen mit dem ALICE Detektor am LHC. Die Messung von Elektronen aus semileptonischen Zerfällen von Charm- und Beautyhadronen erfordert eine genaue Bestimmung des Elektronenuntergrundes. Zum ersten Mal wurde

für diese Art von Messung in ALICE der Hauptanteil des Elektronenuntergrundes durch Identifizierung von Elektronen aus $e^+e^-\gamma$ Dalitz-Zerfällen und γ-Konversionen bestimmt, was, im Vergleich zu vorhergehenden Messungen in pp Kollisionen, zu einer deutlichen Verminderung der relativen systematischen Unsicherheiten führt. Eine Referenzmessung für pp Kollisionen bei einer Schwerpunktsenergie von $\sqrt{s} = 5.02\,\text{TeV}$ wurde aus Messungen in pp Kollisionen bei $\sqrt{s} = 2.76\,\text{TeV}$ und $\sqrt{s} = 7\,\text{TeV}$ interpoliert. Der nukleare Modifizierungsfaktor R_{pPb} von Elektronen wurde im p_{T} Bereich $0.5 < p_{\text{T}} < 8\,\text{GeV}/c$ und im Rapiditätsbereich $-1.065 < y_{\text{cms}} < 0.135$ bestimmt. Das Ergebnis lässt auf eine Skalierung des Produktions-Wirkungsquerschnittes mit der Anzahl der Nukleon-Nukleon Kollisionen schließen. Dies deutet darauf hin, dass Kalte-Materie Effekte für Elektronen aus Charm- und Beautyhadronenzerfällen klein sind, was mit Vorhersagen von verschiedenen theoretischen Modellrechnungen übereinstimmt

Weiterhin wurde die Multiplizitätsabhängigkeit der Produktion von Charm- und Beautyhadronen untersucht. Eine linearen Vergrößerung der normierten Ausbeute von Elektronen aus Charm- und Beautyhadronenzerfällen in p-Pb Kollisionen bei $\sqrt{s_{\text{NN}}} = 5.02\,\text{TeV}$ als Funktion der relative Multiplizität von geladenen Teilchen wurde festgestellt. Die normierten Ausbeute als Funktion der Multiplizität zeigen keine Abhängigkeit vom Transversalimpuls, woraus man schließen kann, dass sich der Produktionsmechanismus von Charm- und Beautyteilchen als Funktion der Multiplizität nicht oder nur sehr gering unterscheidet.

Contents

List of Figures

List of Tables

1 Introduction

Particle physics is trying to grasp nature by formulating fundamental laws describing the elementary building blocks of the universe and their interaction. Up to now four different types of interaction have been discovered (in order of their relative strength): Gravitation (10^{-38}), the weak interaction (10^{-13}), the electromagnetic interaction (10^{-2}) and the strong interaction (10^{0}). The standard model of particle physics (SM) is a theory incorporating the weak, electromagnetic and strong force and has proven successful in describing particle bound states and their interactions. Part of the theory are the gauge bosons mediating the forces. The electromagnetic force acts through photon exchange, the weak force through the $W^{\pm}$ and Z^0 bosons and the strong force through eight different gluons. As part of the standard model a boson was predicted which give the quarks and charged leptons their mass [1, 2]. The boson was named "Higgs boson" and was discovered only recently by the ATLAS and CMS Collaborations at the LHC [3, 4].

1.1 Quantum Chromo Dynamics

Quantum Chromo Dynamics (QCD) is a non-abelian gauge theory in the SU(3) group describing the strong interaction between particles with 3 charges and 3 anti-charges, called color. It includes six different types or flavors of quarks (up, down, strange, charm, beauty, top) each carrying the color charge. Also it includes eight different gluons with linearly independent combinations of color-anticolor charges as result of the SU(3) gauge group. The QCD Lagrangian density is used to describe the quark and gluon interaction:

$$\mathscr{L}_{\mathrm{QCD}} = -\frac{1}{2} G^a_{\mu\nu} G_a^{\mu\nu} + \sum_q \bar{q} \left(i\gamma^\mu D_\mu - m_q \right) q \tag{1.1}$$

$$\text{where } D_\mu = \partial_\mu - i g_S A_\mu \tag{1.2}$$

$$\text{and } G^a_{\mu\nu} = \partial_\mu A^a_\nu - \partial_\nu A^a_\mu - g_S f^{abc} A^b_\mu A^c_\nu \tag{1.3}$$

The first part of $\mathscr{L}_{\mathrm{QCD}}$ represents the gluon self-interaction with the gluon field strength tensor $G^a_{\mu\nu}$, the structure constants f^{abc} of SU(3) and the dimensionless coupling constant $g_S = \sqrt{\alpha_S 4\pi}$. The second part describes the field interaction of a quark spinor q (of mass m_q) with itself and with the gluon field A_μ.

The coupling constant α is a fundamental property of each interaction theory. For the electromagnetic interaction, the coupling is nearly constant for small momentum transfers Q^2 and approximated by $\alpha(Q^2 = 0) = \frac{e^2}{4\pi\epsilon_0} \approx 1/137$. Due to vacuum polarization it is only nearly constant up to very small distances or very large momentum transfers Q^2. Since $\alpha \ll 1$, perturbative theories can be used to calculate states and interaction rates for electromagnetic processes to very good precision. In QCD the strong coupling constant α_S is about 100 times larger than α. The first order for the expansion of α_S on the energy scale is given by:

$$\alpha_S\left(Q^2\right) = \frac{12\pi}{(33 - 2N_f)\ln(Q^2/\Lambda_{\mathrm{QCD}})}, \tag{1.4}$$

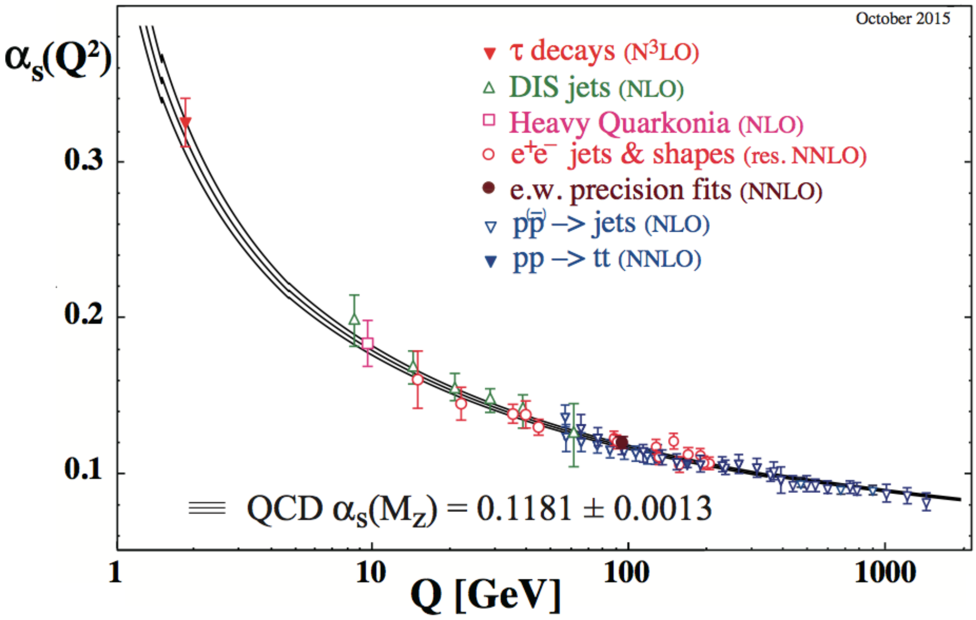

Figure 1.1: Scale dependence of the strong coupling constant α_S as function of the energy transfers Q. Figure taken from [7].

where Q is the momentum transfer in the interaction, N_f is the number of active quark flavors and $\Lambda_{\mathrm{QCD}} \approx 200\,\mathrm{MeV}$ is the QCD scale parameter. This scaling behavior of α_S results in the so called asymptotic freedom for large momentum transfers Q^2, meaning that at large enough energy quarks behave as quasi free particles. The asymptotic freedom was shown by Gross, Wilczek and Politzer [5, 6] in the vanishing of α_S for $Q^2 \to \infty$. The scaling dependence is verified by various measurements [7] as shown in Figure 1.1. The quasi free behavior of quarks and gluons can be resolved in the nucleon parton distribution function $f(x, Q^2)$ by Deep-Inelastic Scattering (DIS) of high energetic electrons. It was found that the evolution of the nucleon structure functions $\mathrm{F}_2(x)$ with Q^2 can be well described by perturbative QCD calculations using the so called Dokshitzer-Gribov-Lipatov-Altarelli-Parisi (DGLAP) equation [8–10]. Perturbative QCD calculations use the small value of α_S to expand the equations in orders of α_S at high Q^2.

On the other side α_S becomes large for small momentum transfers or large distances. Hence the perturbative approach to QCD calculations cannot be used. Another feature of the QCD, the confinement of quarks and gluons into color-neutral objects, is yet to be proven by theory. Experimentally, only color neutral objects consisting of quarks and gluons ("hadrons") have been observed. In addition currently only quark-antiquark pairs and (anti)quark triplets are found, although QCD does not necessarily forbid other structures. Recent measurements for charmonium-like states (containing a $c\bar{c}$ pair) indicate the formation of more exotic multi-quark states [11, 12].

The potential of a $q\bar{q}$ pair can be described in a phenomenological model with Cornell potential V as function of the distance r [13]:

$$V(r) = \sigma\, r - \frac{4\alpha_S(r)}{3r} \tag{1.5}$$

with asymptotic freedom for $r \to 0$ as $\alpha_S(r) \to 0$ and a linear rise for $r \to \infty$ with the string tension $\sigma \approx 1\,\mathrm{GeV/fm}$ resulting from the gluon self-interaction and inhibiting free color charges.

A prediction from QCD [14] is the existence of another state of matter consisting of deconfined quarks and gluons at very high temperatures or baryo-chemical potential. This state of matter is called the Quark-Gluon Plasma (QGP) [15]. The QGP existed in an early phase of the universe until about 10^{-5} s after the big bang.

The phase diagram of QCD can be divided into a hadron gas region, a QGP region and exotic phases at large μ_B. Phase transitions between the regions are predicted to be of cross-over type for zero baryo-chemical potential [16] and of first order for finite baryo-chemical potential [17]. Thus a critical point with a second-order phase transition may exist. A schematic QCD phase diagram is shown in Figure 1.2. Since perturbative QCD calculations are not applicable for the temperatures of the QGP, a successful way of solving the QCD equations numerically is called "Lattice QCD" and uses euclidean space-time on a discrete space-time lattice [19]. However, the current calculations only work for vanishing baryo-chemical potential μ_B. With lattice QCD the critical temperature T_C marking the cross over between the QGP phase and the hadron gas phase was calculated as $T_\mathrm{C} = 154 \pm 9\,\mathrm{MeV}$ at an energy density of $\epsilon_\mathrm{C} \approx 0.34 \pm 0.16\,\mathrm{GeV/fm^3}$ [20]. In Figure 1.3 the normalized energy density ϵ/T^4, the pressure $3p/T^4$ and entropy density $3s/4T^4$ is shown as functions of the temperature T in a 2+1 quark model assuming two equal-mass light quarks and one heavier quark. The model calculations feature a rapid increase at T_C which indicates a change in the state of matter by a change in the degrees of freedom. It is followed by a flattening marking the region of the QGP. The dotted line shows the Stefan-Boltzmann limit for a non-interacting gas of quarks and gluons, the deviations of the model calculations indicate that the quarks and gluons in the QGP are still interacting. The Lattice QCD calculations below T_C are in good agreement with results from Hadron Resonance Gas (HRG) model calculations, which are expected to describe the thermodynamic quantities at low temperatures [21].

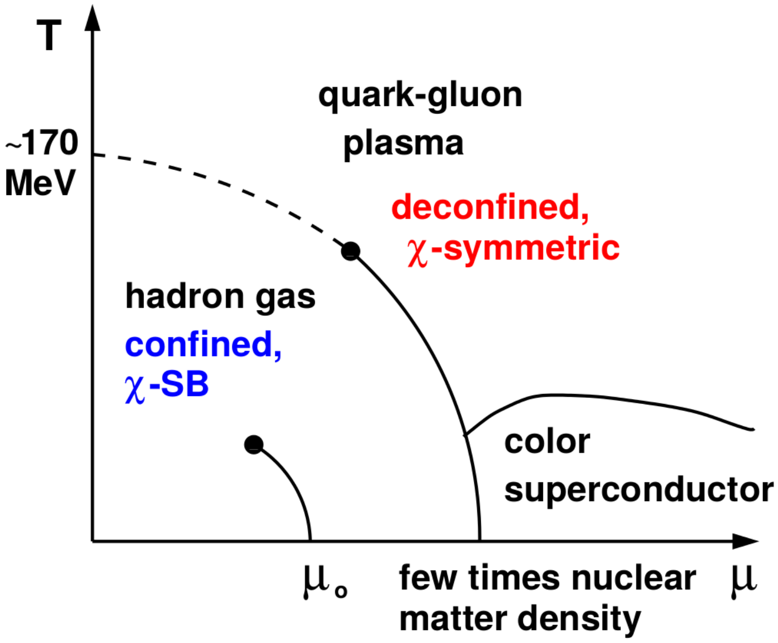

Figure 1.2: Phase diagram as function of temperature T and baryo-chemical potential μ_B. Figure taken from [18].

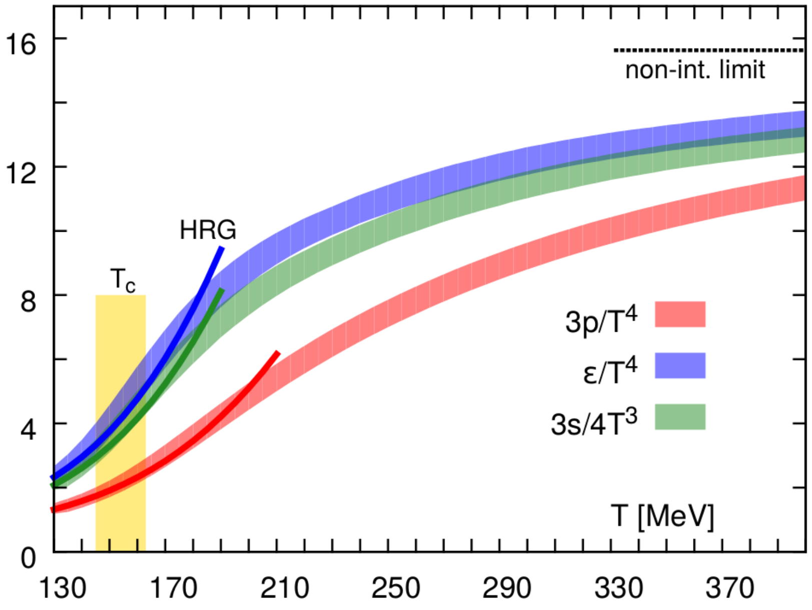

Figure 1.3: Lattice QCD calculation of the energy density (blue), the pressure (red) and entropy density (green) dependence on temperature for 2+1 quark flavors. Results from the Hadron Resonance Gas (HRG) are also shown. Figure taken from [20].

1.3 Heavy-ion collisions

Various experiments have tried to find proof for the existance of the QGP by measuring collisions of accelerated heavy ions. Experiments at the Super Proton Synchrotron (SPS) [22], the Relativistic Heavy Ion Collider (RHIC) [23] and the Large Hadron Collider (LHC) [24] have found evidence supporting the creation of a QGP in the collision of heavy ions at relativistic energies.

Collision geometry

The evolution of the system in heavy-ion collisions is dependent on the collision geometry. Different geometrical variables are defined which can be calculated by various theoretical models and related to experimental observables.

The impact parameter b is defined as the distance between the centers of two colliding nuclei as shown in Figure 1.4. Central collisions are head on with an impact parameter of $b \approx 0$ between the centers of both ions in the plane perpendicular to the beam axis. The interaction region in non-central collisions with $0 < b < 2R$, with R being the radius of each colliding nucleus, is of lenticular shape (indicated in Figure 1.4). The collision geometry can be described using the reaction plane Φ_{RP} which is spanned by the beam axis and the impact parameter axis. The number of nucleons participating in interactions N_{part} (Figure 1.4 red circles) in a collisions and the number of binary nucleon-nucleon interactions N_{coll} is dependent on the impact parameter b which can be translated to a nuclear overlap function $T_{\mathrm{AB}}(b)$. Different models are available to calculate the geometrical variables as function of b (an overview is given in [25]). Two prominent models are the optical Glauber model and the Monte Carlo Glauber model [26].

The optical Glauber model uses area density profiles for each nucleus $T_A(\mathbf{s}) = \int \rho_A(\mathbf{s}, z)\mathrm{d}z$ in the xy plane perpendicular to the beam axis. The nuclear overlap function is calculated by inte-

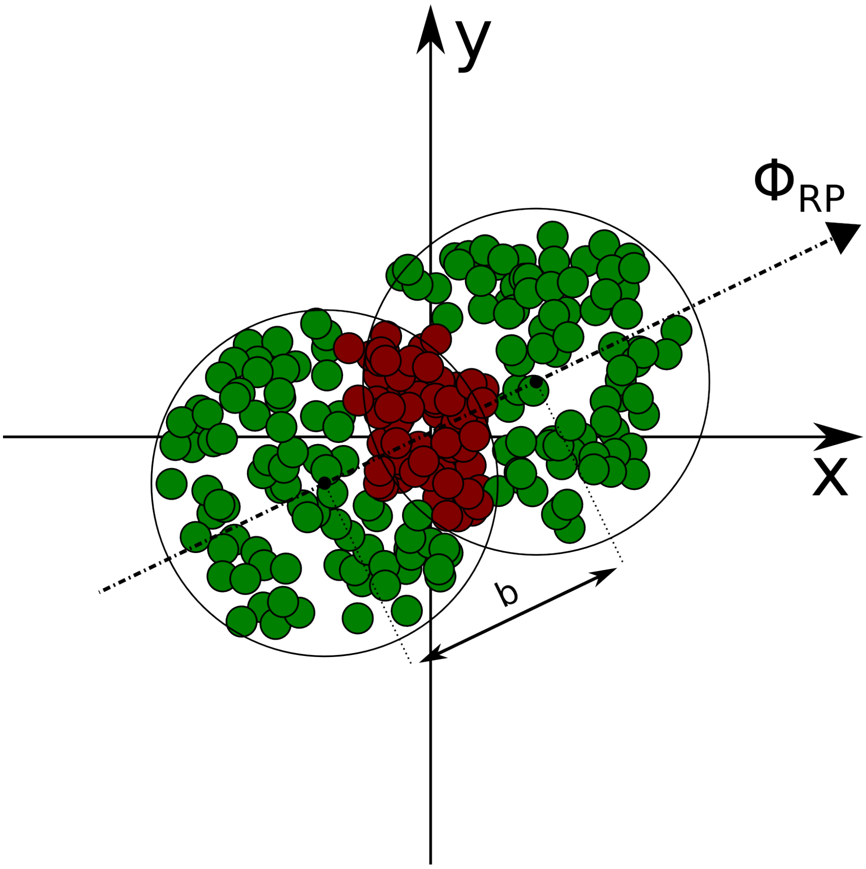

Figure 1.4: Collision of nuclei with reaction plane Φ_{RP} spanned by the impact parameter b and the beam axis (perpendicular to the xy plane).

grating over the density profiles of the nuclei A and B: $T_{\mathrm{AB}}(b) = \int T_A(\mathbf{s})T_B(b - \mathbf{s})\mathrm{d}^2\mathbf{s}$. The nuclear overlap function is related to N_{coll} using the nucleon-nucleon cross section $\sigma_{\mathrm{NN}} T_{\mathrm{AB}}(b) = N_{\mathrm{coll}}(b)$.

In the Monte Carlo Glauber approach nucleons are randomly distributed in each nuclei according to a nuclear density profile (e.g. a Woods-Saxon distribution [27]). An impact parameter is chosen randomly and a collision is simulated by moving the virtual nuclei through each other. Collisions within a distance determined by the square-root of the nucleon-nucleon cross section ($d < \sqrt{\sigma_{\mathrm{NN}}\pi}$) are counted as interactions. All permutations of nucleons pairs are tested for the interaction criterion in order to count N_{coll} and N_{part}. The procedure is repeated to obtain a statistical distribution of N_{coll} and N_{part} as function of b.

The geometrical observables can be averaged over the total range of b or being subdivided in centrality classes defined as percentages of the the impact parameter density distribution. Experimentally, it is not possible to determine the impact parameter directly. Therefore, the collision geometry variables are calculated indirectly via observables which are monotonically increasing as function of the centrality. The detectors to determine the event centrality used by ALICE are described in Chapter 2.2.

1.3.1 Signatures of a quark-gluon plasma

The life time of a QGP is of a few fm/c before harmonization [28]. The time evolution of a QGP produced in heavy-ion collision can be divided into several stages. The Lorentz-contracted nuclei pass each other and produce strong color fields leading to an interacting medium. The strongly interacting medium thermalizes rapidly ($\tau \approx 0.1 - 1\,\mathrm{fm}/c$ [28]) and expands collectively. The expansion leads to a decrease of the medium temperature. At the critical temperature T_C the partons in the QGP transforms into a hadron gas. The process begins with the chemical freeze-out, which marks the point where inelastic scattering stops and hadron abundances are fixed. The process ends after the kinetic freeze-out, where elastic collisions between hadrons stop and the momenta are fixed.

Due to the short time scales, specific indicators have to be used to probe different steps of the medium evolution.

Flow

The radial flow can be measured through the fixed transverse-momentum spectra of hadrons after the kinetic freeze-out. Experimentally, ALICE has observed a collective transverse expansion velocity $\langle \beta_\mathrm{T} \rangle = 0.65 \pm 0.02$, which is obtained by fitting thermal models to different hadron spectra ($\pi^\pm$, $\mathrm{K}^\pm$, $\mathrm{p}/\bar{\mathrm{p}}$) [29].

The spatial asymmetry of interacting constituents in non-central collisions leads to asymmetric pressure gradients in the reaction plane and perpendicular to it, respectively. As a consequence, an azimuthal anisotropy develops in momentum space, called anisotropic flow. The momentum distribution of emitted particles are modulated as function of the azimuthal angle φ with respect to Φ_RP as can be expressed via a Fourier expansion. The anisotropic energy density profile of the elliptic interaction region translates into an asymmetric pressure gradient between the major and minor axis. This asymmetric collective behavior is called flow and the Fourier coefficients v_n can be obtained from a Fourier expansion of the azimuthally-dependent particle yield:

$$E\frac{\mathrm{d}^3N}{\mathrm{d}^3p} = \frac{1}{2\pi}\frac{\mathrm{d}^2N}{p_\mathrm{T}\mathrm{d}p_\mathrm{T}\mathrm{d}y}\left(1 + \sum_{n=1} 2v_n \cos\left(n(\varphi - \Phi_\mathrm{RP})\right)\right), \tag{1.6}$$

with $v_n = \langle \cos[n(\varphi - \Phi_\mathrm{RP})] \rangle$. These flow coefficients v_n are measured as function of p_T and y via the distribution of the azimuthal angles of particles with respect to the reaction plane Φ_RP. The direct flow v_1 is a measure for an asymmetry between the particle yields in the direction parallel to the reaction plane and anti-parallel to it. The elliptic flow v_2 measures the anisotropy between the yields in the reaction plane and perpendicular to it and depends on the collision centrality. Viscous hydrodynamic calculations for an expanding QGP agree with elliptic flow measurements in Au-Au collisions at $\sqrt{s_\mathrm{NN}} = 200\,\mathrm{GeV}$ and Pb-Pb collisions at $\sqrt{s_\mathrm{NN}} = 2.76\,\mathrm{TeV}$ [22]. Hydrodynamic models describe the matter created in Au-Au collisions with a strongly interacting fluid with shear viscosity to entropy density ratio η/s close to the quantum limit $1/4\pi$ indicating that the QGP behaves nearly like a “perfect liquid” [23, 30].

Jet quenching

In heavy-ion collisions and proton-proton collisions the invariant yield for particle production in hard scattering processes can be written according to the factorization theorem [31]. It consists of non-perturbative parton distribution functions (nPDFs) for each of the colliding partons, an interaction term describing the parton-parton scattering process and a Fragmentation Function (FF) representing the non-perturbative fragmentation process of the partons into hadrons. The scattering process can be calculated with perturbative QCD if the momentum transfer is large ($Q^2 \gg \Lambda_\mathrm{QCD}$). The parton itself can radiate gluons before the fragmentation process, leading to a “shower” of secondary partons in a confined cone around the leading parton. The sum of the shower is called jet and the leading parton specifies the jet-type. Historically, gluon jets were first observed in three-jet-events [32].

In heavy-ion collisions high energetic partons are created early in hard scattering processes ($\tau \propto Q^{-1}$) and interact with the evolving QGP through collisional and radiative energy-loss processes. More details concerning the energy-loss mechanisms are discussed in Section 1.5. The energy loss results in a softening of the $p_{\rm T}$-differential yield and can be measured experimentally as a $p_{\rm T}$-dependent suppression through the nuclear modification factor $R_{\rm AA}$ which is calculated from the $p_{\rm T}$-dependent particle yields normalized to a reference measurement in proton-proton collisions where no medium effects are present:

$$R_{\rm AA} = \frac{{\rm d}N_{\rm AA}/\,{\rm d}p_{\rm T}}{\langle N_{\rm coll}\rangle\,{\rm d}N_{\rm pp}/\,{\rm d}p_{\rm T}} = \frac{{\rm d}N_{\rm AA}/\,{\rm d}p_{\rm T}}{\langle T_{\rm AA}\rangle\,{\rm d}\sigma_{\rm pp}/\,{\rm d}p_{\rm T}}, \tag{1.7}$$

using the $p_{\rm T}$-differential particle yields in nucleus-nucleus (AA) collisions and pp collisions and scaled by the average number of binary collisions $\langle N_{\rm coll}\rangle$. In Figure 1.5 $R_{\rm AA}$ is shown as function of $p_{\rm T}$ for charged particles and direct photons and as function of the mass for $W^{\pm}$ and Z^{0} bosons. Since the bosons do not interact strongly and are only produced in initial hard parton-parton scattering processes (for $p_{\rm T}$ or mass $\gg \Lambda_{\rm QCD}$), their yields scale with $\langle N_{\rm coll}\rangle$ (so-called "binary-scaling") which results in $R_{\rm AA} = 1$ within the uncertainties of the measurements. Measurements by ALICE and CMS show a strong suppression of charged-particle yields in Pb-Pb collisions consistent with energy loss of partons in the strongly interacting QGP. However, the particle yields can also be modified by effects related to the nucleus, independent of the produced

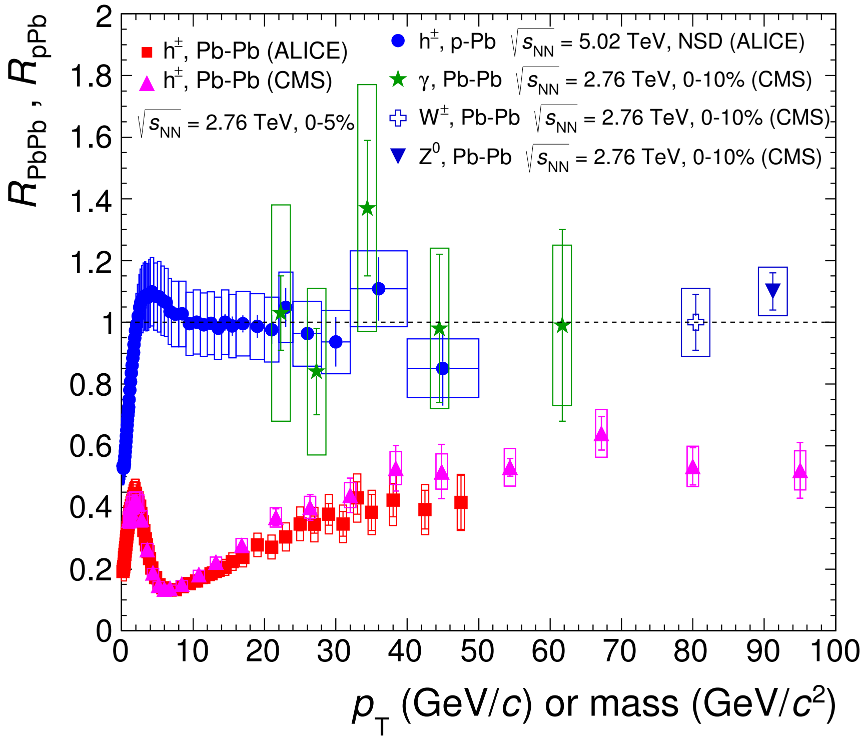

Figure 1.5: The nuclear modification factor for charged particles measured with ALICE and CMS in Pb-Pb and p-Pb collisions at the LHC. Also shown is the $R_{\rm AA}$ of direct photons, $W^{\pm}$ and Z^{0} bosons. Figure taken from [33]

medium. These Cold Nuclear Matter (CNM) effects are investigated in proton-nucleus collision which is also shown in Figure 1.5 and is described in the next section.

1.4 Cold nuclear matter effects

In the discussion of the nuclear modification of particle yields due to interaction of partons with the medium an important point has to be considered: that is the presence of a nucleus in the collision system. Initial state effects such as the modification of the nuclear PDFs or scattering processes before and after the hard interaction need to be studied in systems where no creation of an extended QGP is expected. In proton-nucleus collisions the energy densities necessary to form a QGP in an extended volume is not expected to be reached and CNM effects can be studied. Deep inelastic scattering of leptons on nuclei provide insight about the parton distribution via structure functions. The ratio $R^A_{F_2}(x, Q^2)$ is defined as the nuclear structure function $F^A_2(x, Q^2)$ divided by the proton structure function $F^p_2(x, Q^2)$ as function of the parton momentum x for a given momentum transfer Q^2. In Figure 1.6 different regions for deviations of $R^A_{F_2}(x, Q^2)$ from unity are shown [34]. The Fermi motion of nucleons in the nuclei enhances the nuclear PDF in the limit $x \rightarrow 1$. The depletion in the region $0.4 < x < 1$ is called EMC-effect. After being measured first by the European-Muon-Collaboration (EMC) the origin of this effect is still not well understood [35]. A so-called anti-shadowing region is located at intermediate x (0.04–0.4) resulting in an enhancement of the parton density in nuclei. The shadowing regime of $x < 0.04$ results in a depletion of the parton density. Heavy-flavor production at LHC energies measured at mid-rapidity is in this regime ($x \sim m_{\mathrm{Q\overline{Q}}}(\mathrm{GeV})/\sqrt{s}(\mathrm{TeV}) \approx 10^{-3}$) and might be affected by shadowing of the nuclear PDF resulting in a reduced heavy-flavor production cross section. However, other effects such as gluon saturation at very small x might also lead to a depletion of the gluon density in nuclei with respect to protons due to the Lorentz contraction of ultra-relativistic heavy ions [36]. However, shadowing of the nuclear PDF is not the only effect which needs to be considered. Multiple soft scattering of the parton in the nucleus prior to the hard scattering (k_{T}-broadening) is an interpretation for an observed enhancement of the hadron cross section called the Cronin effect [37]. Energy loss through multiple soft scattering of the scattered parton also plays a role [38, 39].

1.5 Heavy quark production and energy loss

Heavy quarks, i.e. charm and beauty quarks are a unique probe for the QGP. Due to their large mass ($m_c \approx 1.3$ GeV$/c^2, m_b \approx 4.2$ GeV$/c^2$ [7]) charm and beauty quarks are almost exclusively produced in hard scattering processes. Leading order processes for the production of charm and beauty quarks are gluon-gluon fusion processes ($\mathrm{gg} \rightarrow \mathrm{Q\overline{Q}}$) or quark-antiquark-annihilation processes ($\mathrm{q\overline{q}} \rightarrow \mathrm{Q\overline{Q}}$) on timescales much shorter than the formation time of the QGP ($\tau \propto \left(2m_Q\right)^{-1} < 0.1\,\mathrm{fm}/c$) [28]. This means that heavy quarks experience the full evolution of the medium while traversing and interacting with it.

In pp collisions the measurement of heavy-flavor production provides a crucial test for pQCD calculations. Due to the large initial masses of charm and beauty quarks, perturbative calculations of production cross sections are feasible down to zero p_{T}. However, the total cross sections of charm and beauty hadrons still depend on the Parton Distribution Functions (PDFs) and Fragmentation Functions (FF) which cannot be treated perturbatively. In the case of heavy

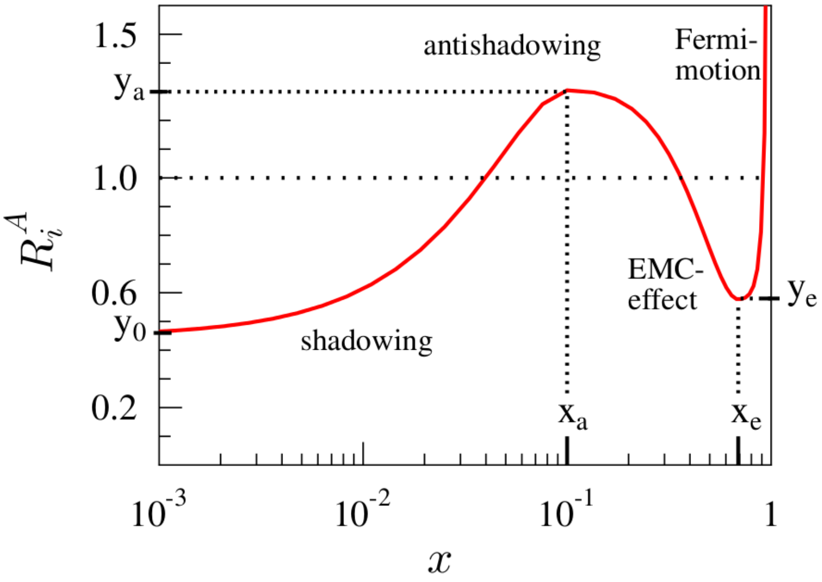

Figure 1.6: Schematic view of the nuclear parton distribution function normalized to a nucleon parton distribution function. Figure taken from [34].

quarks, the partons can fragment separately into hadrons with open heavy flavor or form a quark-antiquark bound state (quarkonia, $Q\overline{Q}$).

In 1986 Matsui and Satz proposed the idea of a screening of the quarkonium color charge in a deconfined QGP medium [40], similar to Debye screening in an electromagnetic plasma. Due to different binding strengths, “sequential melting” was proposed to occur for the quarkonium bound states depending on the medium temperature. Thus the measurement of the suppression of quarkonium yields in A-A collisions was proposed as a “thermometer” to measure the QGP temperature. However, it turned out that other effects also modify the quarkonium yields. While J/ψ suppression was observed at SPS [41], the results were also compatible with other effects [42] and thus inconclusive. At RHIC and LHC energies, the charm cross sections in A-A collisions is large enough to regenerate charmonium states in the medium [43] or at the phase boundary [44].

However, quarkonium production in hadron collisions is only a 1-2% fraction of the total heavy-flavor cross section essentially independent of $\sqrt{s}$ [45]. The largest part of the produced heavy-flavor quarks hadronize into open heavy-flavor mesons and baryons. Current leading models of describing heavy quark production in hadron collisions are FONLL (Fixed-Order Next-To-Leading-Log resummation [46–48]) and GM-VFNS (General-Mass Variable-Flavor-Numbering-Scheme [49].

Beside providing a test for the perturbative description of heavy-flavor production in QCD, the measurement of charm and beauty hadrons provides a baseline for measurements in Pb-Pb collisions. The interaction of high momentum heavy quarks with the medium is supposed to be different compared to that of light quarks or gluons [50]. Gluon radiation processes have different color coupling factors for quarks (C_F) and gluons (C_A) depending on the number of flavors N_c. While for quarks the color factor is $C_F = (N_c^2 - 1)/(2N_c) = 4/3$, the color factor for gluons is $C_A = N_c = 3$. This results in an ordering of the energy loss for radiative and collisional energy loss processes in the medium: $\Delta E_g > \Delta E_q$. Because of their large mass,

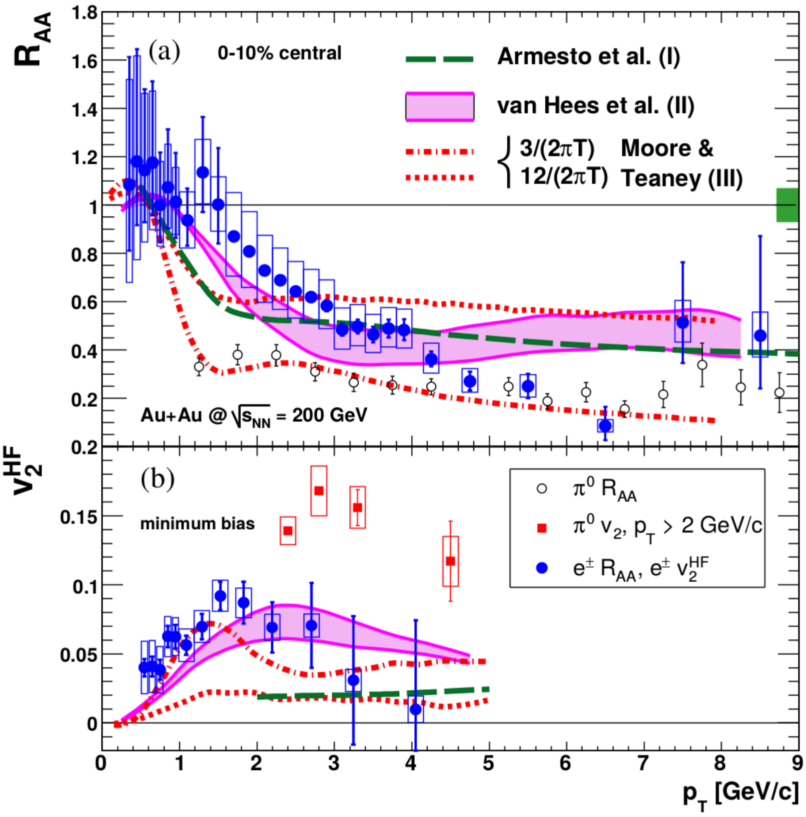

Figure 1.7: Nuclear modification factor R_{AA} and the elliptic flow coefficient v_2 for electrons from heavy-flavor hadron decays together with model calculations [56–58]. Figure taken from [55].

soft gluon radiation is suppressed at small/forward angles for charm and beauty quarks. This so-called dead-cone effect [51, 52] results in a decreasing radiative energy loss for increasing quark mass. However, theoretical model calculations suggest that collisional energy loss for heavy-flavor quarks plays an equally important role especially in the low p_T region [53, 54]. Together, the energy loss for different partons is decreasing from light-flavor quarks to heavy-flavor quarks due to their different masses. This deviations for the energy loss leads to a difference in the softening of the p_T-differential spectra of different hadron species which would result in a difference for the nuclear modification factor: $R^{\pi}_{AA} < R^{c}_{AA} < R^{b}_{AA}$. However, the R_{AA} is not only dependent on the energy loss but also on the fragmentation. The p_T-differential yields of light-flavor particles are dominated by soft scattering processes at low p_T which do not scale with N_{coll} but rather with N_{part}. In addition the p_T-distribution is influenced by a radial flow of the expanding medium. For light-flavor particles many modifications of the R_{AA} need to be taken into account. Also for the R_{AA} of heavy-flavor hadrons the collective flow plays a role. RHIC has measured the R_{AA} and elliptic flow for electrons from heavy-flavor hadron decays in Au-Au collisions at $\sqrt{s_{NN}} = 200\,\text{GeV}$ [55] observing a non-zero v_2 as shown in Figure 1.7, which indicates the participation of heavy-flavor quarks in the collective flow. A difference in R_{AA} as function of N_{part} of D mesons with ALICE [59] and non-prompt J/ψ (J/ψ coming from B meson decays) with CMS [60] is observed. The R_{AA} shown in Figure 1.8 includes model calculations with radiative and collisional energy-loss by Djordjevic *et al.* [61]. The measurements indicate a mass-dependent energy-loss ordering of heavy-flavor quarks which is

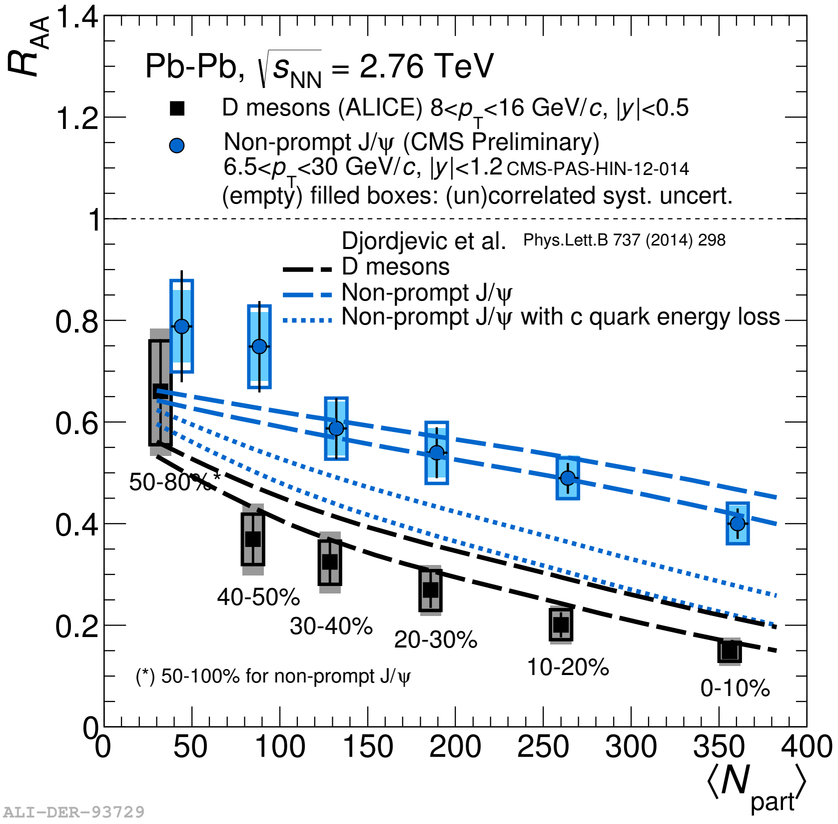

Figure 1.8: R_{AA} as function of $\langle N_{part} \rangle$. Figure derived from the ALICE measurements for D mesons[59], the non-prompt J/ψ from CMS [60] and theoretical model calculations by Djordjevic *et al.* [61].

successfully described by theoretical model calculations. However, in general the description of the p_T-differential suppression of heavy-flavor production in A-A collisions is still a challenge for models when compared to the non-vanishing elliptic flow v_2 as shown in Figure 1.7. The measurement is compared to the R_{AA} of π^0 and indicates less suppression of heavy-flavor yields for $p_T < 4\,\mathrm{GeV}/c$, in agreement with the energy-loss picture. At the same time a non-zero v_2 could indicate the participation of low p_T heavy-flavor quarks in the collective expansion of the medium. Model calculations including radiative energy loss by Armesto *et al.* [56] are able to describe the R_{AA} but not the v_2. Model calculations from van Hees *et al.* [57] and Moore and Teaney [58] including elastic scattering are able to qualitatively describe the data.

1.6 Measurement of heavy-flavor production

Open heavy-flavor hadrons decay weakly, resulting in a decay length of 100–300 μm for D mesons and 400–500 μm for B mesons [7]. Thus, the average decay vertex of heavy-flavor hadrons is displaced from the main interaction (collision) vertex. This characteristics can be used in the direct reconstruction of heavy-flavor hadron decays. The branching ratio for hadronic decays into kaons and pions is e.g. $D^+ \rightarrow K^+\pi^-\pi^- \approx 9.1\%$ and $D^0 \rightarrow K^+\pi^- \approx 3.9\%$. Generally, pions and kaons are produced abundantly in fragmentation processes and soft scatterings, which results in a challenge in A-A collisions, where many of these processes happen. The invariant mass spectrum for D mesons is dominated by background of uncorrelated pion-kaon combinations. By using a vertexing detector the secondary vertex of the displaced D meson decay can be identified and a large part of the combinatorics can be reduced. However, these topological selections suffer from large efficiency loss especially at low momentum [62]. The identification of B mesons with ALICE is rather limited by rate than through the large combinatorial background.

An alternative approach to the full reconstruction of D mesons is the measurement of the inclusive heavy-flavor hadron cross section via their semi-leptonic decay channel. Charm and beauty hadrons have a large branching ratio to electrons ($c \rightarrow e\overline{\nu}_e X \approx 10.3\%$ and $b \rightarrow e\overline{\nu}_e X \approx 10.9\%$). In these decays combinatorics does not play a role since the electrons are measured inclusively. However, all other sources of electrons coming not from heavy-flavor hadrons have to be identified and subtracted from the inclusive yield. Also, by measuring the electrons from heavy-flavor hadron decays, the kinematics of the charm and beauty quarks are folded additionally with the decay kinematics resulting in a loss of information. Using the difference in the decay length from D and B mesons, it is possible to extract the yield of electrons coming from beauty-hadron decays. ALICE has measured the fraction of electrons from beauty hadron decays in pp collisions at $\sqrt{s} = 2.76\,\mathrm{TeV}$ [63] and $\sqrt{s} = 7\,\mathrm{TeV}$ [64]. The yield of electrons from decays of open heavy-flavor hadrons above $p_{\mathrm{T}} > 4\,\mathrm{GeV}/c$ is dominated by the decay of beauty hadrons.

The estimation of the electron background not coming from heavy-flavor hadron decays is crucial for the precision of the measurement of the electrons from heavy-flavor hadron decays. There are different approaches to estimate the yield of background electrons which have been used by the PHENIX Collaboration [65, 66] and the STAR Collaboration [67, 68]. In Section 3 the methods, used by ALICE for the first time in the measurement of electrons from heavy-flavor hadron decays and developed in this work, are described in detail. The results are already published in [69].

1.7 Multiplicity dependence

The question whether in small collision systems a medium exhibiting collective behavior is formed has become a major topic of research in the last years. ALICE, ATLAS and CMS have observed in high-multiplicity events of p-Pb collisions a “double-ridge” structure in $\Delta\eta$–$\Delta\varphi$ particle correlations [70–72] similar to results seen in Pb-Pb collisions [73]. The results in p-Pb collisions could be interpreted as collective behavior and are described by hydrodynamic model calculations which would suggest the formation of a medium in high-multiplicity events. However, also Color Glass Condensat (CGC) model calculations are able to describe the observed results, which would suggest initial state effects responsible for the observations [74].

For the measurement of the nuclear modification factor R_{pPb} of electrons from heavy-flavor hadron decays these high-multiplicity effects are not visible due to the small cross section of high-multiplicity events [75]. Studies of self-normalized yields as function of the relative charged-particle multiplicity are used to investigate these rare high-multiplicity events and the influence on heavy-flavor production. ALICE has measured the self-normalized D-meson yield as function of the relative charged particle multiplicity in p-Pb collisions which exhibit a more-than-linear increase for the yield as function of the relative charged-particle multiplicity [76]. To provide further constraints to the dependence of heavy-flavor production on the event multiplicity in p-Pb collisions, the self-normalized yield of electrons from semi-leptonic heavy-flavor hadron decays as function of the relative charged-particle multiplicity in p-Pb collisions at $\sqrt{s_{\mathrm{NN}}} = 5.02\,\mathrm{TeV}$ is measured and discussed in Section 4 of this work. The inclusive yield of electrons from charm and beauty-hadron decays enables the measurement of the dependence of beauty production in high-multiplicity events due to the large contribution of electrons from beauty-hadron decays for $p_{\mathrm{T}} > 4\,\mathrm{GeV}/c$.

1.8 Outline

Within this thesis the measurement of the production cross section of electrons from heavy-flavor hadron decays in p-Pb collisions with ALICE at the LHC is described. The calculation of the nuclear modification factor R_{pPb} is presented and discussed with theoretical models which include CNM effects. Furthermore, the multiplicity dependence of heavy-flavor production is studied through the measurement of self-normalized yields of electrons from heavy-flavor hadron decays as function of the charged-particle multiplicity, estimated at mid-rapidity and at backward rapidity.

This thesis is organized as follows: In the next Chapter a short introduction to the Large Hadron Collider and the ALICE apparatus is given. In Chapter three the procedure of the measurement of the production cross section and R_{pPb} is explained. In Chapter four the measurement of the self-normalized yield of electrons from heavy-flavor hadron decays as function of the charged-particle multiplicity is presented. The conclusion and an outlook is given in Chapter five.

2 LHC and ALICE

2.1 The Large Hadron Collider (LHC)

The data analyzed in this work was measured with A Large Ion Collider Experiment (ALICE) at the LHC. ALICE is one of the four major experiments at the LHC. The LHC [77–79] is located in a circular tunnel of 26.7 km circumference beneath Switzerland and France. The tunnel was build between 1984 and 1989 to host the Large Electron-Positron (LEP) collider. LEP was disassembled in 2001 to start building the LHC project [80]. Due to the small cross section of the tunnel of about 3.7 m diameter, the beam pipes and bending magnets had to be designed in a unique way to fit in the tunnel. The beams share the same dipole magnets and thus have the same rigidity (p/z) for each beam. In asymmetric collision systems such as proton-lead this results in a boosted nucleon-nucleon center-of-mass frame by $\beta_\mathrm{B} = (1 - Z/A)/(1 + Z/A) = 0.435$ (for p-Pb) with respect to the laboratory frame. The center-of-mass energy per nucleon-nucleon pair $\sqrt{s_\mathrm{NN}}$ is give by the kinetic energy of the proton multiplied with $2\sqrt{\frac{\mathrm{Z}}{\mathrm{A}}}$ for a p-A collision system.

The design center-of-mass energy for the complete accelerator is 14 TeV at a peak luminosity of $\mathscr{L}_\mathrm{pp} = 10^{34}\mathrm{cm}^{-2}\mathrm{s}^{-1}$ for proton-proton collisions and 5.5 TeV at a peak luminosity of $\mathscr{L}_\mathrm{pp} = 10^{27}\mathrm{cm}^{-2}\mathrm{s}^{-1}$ for collision of fully ionized lead nuclei.

As shown in Figure 2.1, the acceleration of protons starts with the LINear ACcelerator 2 (LINAC2) where the protons are accelerated to 50 MeV and split into bunches. They are further accelerated to 1.4 GeV in the Proton Synchrotron Booster (PSB) before being injected into the Proton Synchrotron (PS). The procedure is slightly different for lead ions. Lead metal is evaporated, ionized and accelerated to 4.2 MeV per nucleon in the LINear ACcelerator 3 (LINAC3). After the complete ionization in a stripper the lead ions are injected into the Low Energy Ion Ring (LEIR). The LEIR accelerates the ions further to 72 MeV per nucleon before injecting them to the Proton Synchrotron. Here protons are accelerated to 25 GeV and lead ions to 5.9 GeV per nucleon. After reaching the full energy the protons/lead ions are injected into the Super Proton Synchrotron (SPS) and further accelerated to 450 GeV for protons and 177 GeV per nucleon for lead nuclei. Afterwards they are injected into the LHC in opposite directions for both beam pipes and accelerated up to the designed energy. The LHC is a ring like structure with eight arcs and eight straight sections. The locations on the surface are named in a ascending numerical fashion (“Point 1-8”). There are four major experiments (ALICE, ATLAS, CMS, LHCb) and two smaller experiments (LHCf and TOTEM) located at the LHC. The ALICE apparatus will be discussed in the following section in detail. A Toroidal LHC ApparatuS (ATLAS) [82] is a multi-purpose detector located at Point 1. The Compact Muon Solenoid (CMS) [83] is located at the newly created Point 5. Both experiments are optimized to measure proton-proton collisions with maximum interaction rate and can trigger on rare physics signals as demonstrated by the (successful) search for the Higgs Boson. The physics goal of the LHCb experiment is to measure details of the CP violation and rare decay modes of hadrons containing beauty quarks. The TOTal Elastic and diffractive cross section Measurement (TOTEM) [84] is located at Point 5, ±147 m and ±220 m away from the interaction point. It is designed to measure the elastic proton-proton scattering cross section at a very forward angle in collaboration with CMS. The

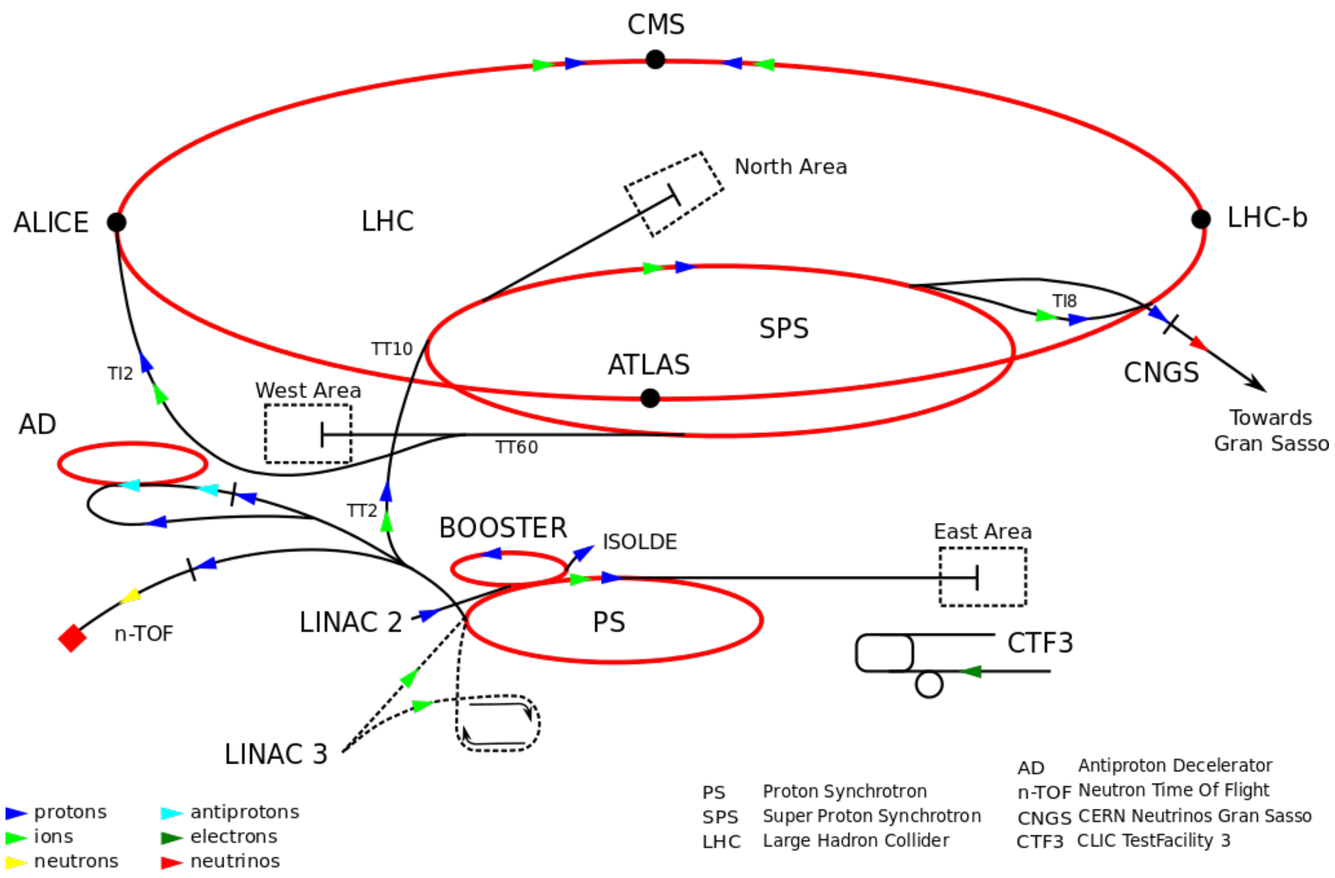

Figure 2.1: LHC injection process [81].

LHC forward (LHCf) experiment [85] is located at Point 1, about 140 m from the interaction point in both directions. It is used to study neutral particle production at a very forward angles to constrain cosmic shower models.

2.2 The ALICE apparatus

The ALICE apparatus is a multi-purpose detector designed to operate in a high particle-multiplicity environment (up to $dN_{ch}/d\eta \approx 4000 - 8000$) which was expected in central Pb–Pb collisions at 5.5 TeV [86, 87]. However, the multiplicities turned out to be only of the order $dN_{ch}/d\eta \approx 1000 - 2000$ for Pb-Pb collisions at 2.76 TeV [88]. ALICE is located at Point 2. The magnet is reused from the previous L3 experiment for the ALICE apparatus. ALICE includes many different detector technologies to cover a wide range in momentum and rapidity to detect particles produced in hadron-hadron collisions. It consists mainly of two parts, a central barrel to measure particles at mid-rapidity and a muon spectrometer arm to measure muons at forward rapidity. The arm is pointing in the direction of the CMS detector[1]. In the following a brief overview of the installed detectors will be given. The ALICE coordinate system is a right handed system centered in the middle of the ALICE barrel. The x-axis is pointing to the center of the LHC ring and the y-axis is pointing vertically upwards. Thus the z-axis points along the LHC beam in the opposite direction of the ALICE muon arm. The Cartesian coordinate system

---

[1] The direction is referred as the “C-side”; respectively the opposite side pointing to the ATLAS detector is called “A-side” (see Figure 2.2)

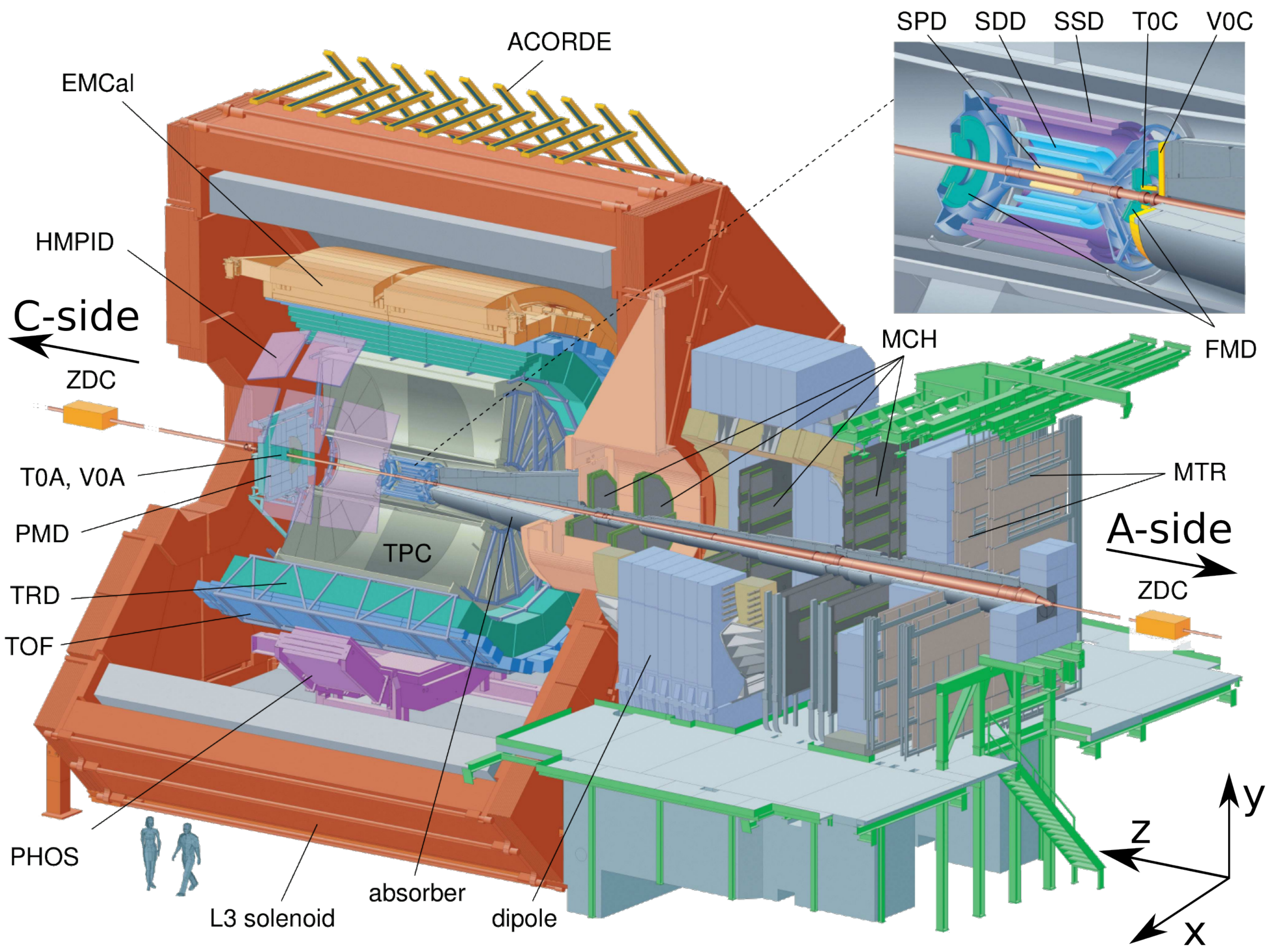

Figure 2.2: The ALICE apparatus. Figure taken from [89].

is shown in Figure 2.2. In addition, ALICE also uses a polar coordinate system with φ defined as the azimuthal angle in the xy-plane and the pseudo-rapidity η, which is defined in terms of the polar angle θ:

$$\eta = -\ln\left[\tan\frac{\theta}{2}\right], \tag{2.1}$$

The detector subsystems of the ALICE central barrel are embedded into the L3 magnet which creates a solenoidal magnet field of up to 0.5 T inside the active detection area. The magnetic field lines are parallel to the z-axis and thus charged particles are deflected perpendicular to the z-axis in the azimuthal direction. Particles propagating through the detector interact with the detector material. The time and space dependent information from the detectors is used to reconstruct the trajectories of these particles. The momentum component transverse to the beam axis (p_{T}) can be extracted by measuring the track curvature in the xy plane.

Inner Tracking System

The Inner Tracking System (ITS) has six detector layers. The ITS covers the full azimuth and $|\eta| < 2$ in pseudo-rapidity for the first layer, $|\eta| < 1.4$ for the second layer and $|\eta| < 0.9$ for the other four layers. The ITS extends radially from 3.9 cm to 43 cm. The Silicon Pixel Detector

(SPD) comprises the two innermost layers of the ITS. The third and fourth layers constitute the Silicon Drift Detector (SDD) and the fifth and sixth layers are Silicon Strip Detectors (SSD).

The main purpose of the ITS is to provide a vertex resolution better than 100 μm, secondary vertex determination, precise particle tracking to very low p_T (<100 MeV) and support for the tracking with the TPC. The ITS is designed to have a very low material budget with a radiation length of about 1.1% X_0 per layer for the active detector material. The thickness of the whole ITS including supporting structures is about 10%X_0 [89].

The ITS also serves an important role to match tracks from the TPC. By matching of the tracks between different detectors the momentum resolution can be increased with respect to the resolution of the individual detectors.

SPD

The SPD consists of two layers of silicon pixel detectors with digital read-out. In total about 10^6 pixels are installed to reach the design goal of the track resolution and track separation. The high number of read-out channels is needed to keep the occupancy of the detector small, since track densities of $\sim 50\,\text{cm}^{-2}$ are expected. The SPD extends from 3.9 cm to 7.6 cm and is therefore very close to the beam pipe (3 cm). The two layers of the SPD have a pseudo-rapidity coverage of $|\eta| < 2.0$ and $|\eta| < 1.4$ to give information about the charged particle multiplicity in an extended pseudo-rapidity range.

SDD

The SDD extends from 15 cm to 23.9 cm and has an analogue read-out of 133 thousand channels. Particle dependent energy loss $\mathrm{d}E/\mathrm{d}x$ in the detector can be measured and, thus, information about the particle species can be obtained. The main purpose is to provide tracking and particle identification (PID).

SSD

The SSD is equipped with strips of silicon sensors with an analogue read-out of about $\sim 2.6 \cdot 10^6$ channels. It spans from 38 cm to 43 cm in radius with a pseudo-rapidity $|\eta| < 1.0$, and it provides tracking and PID information.

Time Projection Chamber

The Time Projection Chamber (TPC) is a cylindrical detector which has an inner radius of 85 cm and outer radius of 247 cm in the full azimuthal range. It is split horizontally by a central electrode in two chambers of 250 cm length in the ALICE central barrel. The active volume of 88 m^3 is filled by a slightly over-pressurized gas mixture of Ne-CO_2-N_2 (85.7–9.5–4.8). A −100 kV electrical potential is applied on the central electrode to provides an electric field of 400 V/cm between the central electrode and the end caps of the field cage which are kept at ground potential. The electric field lines are parallel to the magnetic field lines generated by the surrounding solenoid magnet. The material budget in radiation lengths is about 3.5% X_0 at $\eta = 0$.

Charged particles moving through the active volume of the TPC leave ionization traces by interaction with the gas. While positive ions drift to the central electrode, electrons drifts to the end caps where Multi Wire Proportional Chambers (MWPC) with cathode pad read-out are installed. Here the electrons have to pass a gating grid which is synchronized with a central read-out trigger (L1). The trigger fires when certain conditions are met (depending on the selected trigger). It is closed after the maximum drift time of 88 μs to minimize the drift of positive charge from the MWPCs amplifying region into the active volume and distort the linear electric field. The drift velocity is strongly dependent on the temperature and pressure of the gas. Cooling systems for the high voltage and read-out electronics are necessary to assure a thermal stability of the gas within $\Delta T \leq 0.1$ K. During LHC operations with high rate proton-proton collisions up to 60 interactions can happen during this drift time. Tracks are assigned to the respective collision by software using the TPC and ITS for tracking and vertex finding.

The read-out of the TPC is split into 18 azimuthal sectors on each end cap. Each sector is split radially into two read-out chambers comprising 159 stacked rows of read-out pads. The track density in the TPC decreases with larger radius and thus a lower spatial resolution is necessary in the outer region. In total the TPC is equipped with 557568 read-out pads. The TPC is calibrated using a laser system with mirrors, which fires predefined laser beams inside the volume. The TPC is designed for tracking of up to 20000 charged primary and secondary particles in the pseudo-rapidity range $|\eta| < 0.9$. The tracks need a minimum p_{T} of 100 MeV to reach the TPC. The TPC is not only used for precise tracking and momentum determination but also for particle identification. The amplified read-out signal in the pads is proportional to the gas ionization charge through the specific energy loss $\mathrm{d}E/\mathrm{d}x$ of charged particles depending on their Lorentz β.

Transition Radiation Detector

The Transition Radiation Detector (TRD) extends radially between 290 cm and 368 cm in $|\eta| < 0.84$. The fully equipped TRD has 540 modules arranged in 18 super-modules which are aligned to the TPC sectors. Each super-module comprises five horizontally aligned stacks of six detector modules. A module consists of a 4.8 cm thick fiber radiator followed by MWPC. The MWPCs are filled with a Xe-CO$_2$ (85–15) gas mixture. The TRD has about 1.18 Million read-out pads to provide tracking information in (η, φ) direction. Particles ionize the gas while penetrating the detector modules. The charge from the ionization is amplified and produces an analogue signal in the read-out pads. Additional charge is created by transition radiation, which intensity is dependent on the Lorentz γ. This results in larger transition radiation from electrons traversing the radiator compared to hadrons at the same momentum which have a much larger mass ($\gamma \approx p/m$). The rejection factor of the TRD for pions is 100 for an electron efficiency of 90% in a high occupancy situation. This means at least 90% of all electrons are detected and less than 1% of all electrons are misidentified pions. The TRD can be used to create a hardware electron trigger and it improves the tracking resolution of the ITS and TPC.

Only 7 TRD super-modules were installed at the start of the run in 2009. The number was increased to 13 in 2012 and completed to the full stack of 18 super-modules during the shutdown in 2014. Due to the limited acceptance during the p-Pb collision in 2013, the TRD is not used for this analysis.

Time-Of-Flight detector

The Time-Of-Flight (TOF) detector is able to separate particles of different species with the same momentum by the time difference of their arrival due to their different velocity. The TOF uses

Multi-gap Resistive-Plate Chambers (MRPCs) in 18 segments on top of the TRD super-modules. The MRPCs produce an immediate amplified signal of single ionization passing through the active detector material. The time resolution is 90 ps–120 ps including the resolution of the T0 (see below) for the start time. The TOF has 157248 read-out pads and covers the full azimuth in $|\eta| < 0.9$ and extends radially from 370 cm to 399 cm. The TOF is able to distinguish pions and kaons with a resolution of 3σ (99.7%) up to 2.5 GeV/c. The same separation is achieved for kaons and protons up to 4 GeV/c.

HMPID

The High-Momentum Particle Identification Detector (HMPID) is designed to extend PID capabilities of the TOF for charged particles in the region 3-5 GeV/c. It covers $|\eta| < 0.6$ in pseudo-rapidity and $1.2° < \varphi < 58.8°$ in azimuth. The HMPID is based on a Ring Imaging Cherenkov (RICH) counter. Charged particles emit Cherenkov photons in a C_6F_{14} radiator with a specific opening angle dependent on the particle momentum. The Cherenkov photons are emitted in a cone around the charged particle trajectory, and they are measured with a MWPC filled with CH_4.

PHOS

The PHOton Spectrometer (PHOS) is electromagnetic calorimeter consisting of 3584 lead-tungstate crystals ($PbWO_4$). It is split into 5 horizontally separated modules and will cover $|\eta| < 0.12$ in pseudo-rapidity and $220° < \varphi < 320°$ in azimuth. However, only 3 out of 5 modules are installed currently. It is designed to measure direct photons and decay photons of π^0 and η decays via the electromagnetic showers they deposit in the detector. A high energy resolution is achieved by using very dense lead-tungstate crystals with a thickness of 20 X_0. The PHOS has a Charged-Particle Veto (CPV) on top to discard signals created by charged particles.

EMCAL

The Electro-Magnetic CALorimeter (EMCal) is a Pb-scintillator calorimeter which covers $|\eta| < 0.7$ in pseudo-rapidity and $80° < \varphi < 187°$ in azimuth. It is able to measure high momentum electrons and photons. It has a dense structure with a thickness of 20 X_0. The energy resolution of the EMCAL is better than 5% for deposited energies larger than 10 GeV.

V0

The V0 detector has two scintillator rings located 340 cm (V0A, on the A-side) and -90 cm (V0C, on the C-side) away from the interaction point. They cover the full azimuth and $2.8 < \eta < 5.1$ and $-3.7 < \eta < -1.7$ in pseudo-rapidity respectively. Each ring is segmented into four sub-rings of increasing radius, while each sub-ring is split into 8 uniform modules in φ. Thus in total 32 modules are read out for each the V0A and V0C. The V0 detector is used to trigger on minimum bias (MB) events and for multiplicity measurements. The measured V0 multiplicity can be used to calculate the event centrality. The V0 scintillators have a good time resolution (< 1 ns). They are used to discriminate beam–beam collisions from beam-gas interactions by comparing the time of arrival between a signal in the V0A and the V0C for a registered event.

T0

The T0 detectors have a similar setup as the V0 detectors. The T0 detectors are two Cherenkov counter arrays located 375 cm (T0A) and -72.7 cm (T0C) away from the interaction point. They cover the full azimuth and $4.61 < \eta < 4.92$ and $-3.28 < \eta < -2.97$ in pseudo-rapidity respectively. Each array is equipped with 12 Cherenkov counter modules with a time resolution around 50 ps. Each counter consists of a quartz converter with attached photomultiplier tube. The T0 is used to provide a timing trigger for the collision which provides the start time for the time-of-flight measurement in the TOF detector. The vertex position in z is determined with a resolution of 1.5 cm by measuring the difference of the time signal in T0A and T0C. In addition, the T0 has similar capabilities as the V0 detector in terms of measuring the event multiplicity and discrimination of beam-gas events.

ZDC

The Zero Degree Calorimeters (ZDCs) are two calorimeters placed 112.5 m away from the ALICE interaction point in opposite z directions. The ZDCs are split into a proton (ZP) and neutron (ZN) calorimeter. The ZDCs are designed to measure the number of spectator nucleons in the non-overlapping region of a nucleus-nucleus collision. The ZN is placed between the diverging beam pipes, while the ZP is placed off-center according to the deflection of the protons in the magnetic fields of the LHC bending magnets. The detectors consists of a passive absorber and active quartz fibers. The absorber is made of tungsten for the ZN and brass for the ZP. Initial nucleons produce particle showers in the absorber which induces Cherenkov light in quartz fibers. The Cherenkov radiation is measured with photomultiplier tubes. Because of the very high radiation levels around the beam pipes, the ZDC are mounted on a vertical lifting platforms which can be lowered if needed.

FMD

The Forward Multiplicity Detector (FMD) is a setup of 5 silicon semiconductor detector rings along the beam line. Their pseudo-rapidity range ($-3.4 < \eta < -1.7$ and $1.7 < \eta < 5.0$) overlaps with and extends the pseudo-rapidity range of the ITS to provide additional information about the charged particle distribution. Two rings are placed -62.8 cm and -75.2 cm away from the IP on the C-side and three rings are placed 75.2 cm 83.4 cm and 320 cm away from the IP on the A-side. Due to the MUON spectrometer on the C-side an additional ring is not possible here.

PMD

The Photon Multiplicity Detector (PMD) is an array of gas proportional counters placed 364 cm away from the interaction vertex on the A side and covers $2.3 < \eta < 3.7$ in pseudo-rapidity over the full azimuth. It is used to measure photon production at forward rapidity and give information about the reaction plane of the colliding lead ions event by event. Because of the high particle density at forward pseudo-rapidity photons can not be easily identified by the calorimeter shower profile. The PMD consists of two detector planes between a 2 cm thick converter (lead+stainless steel). Each plane is equipped with 110592 hexagonal gas proportional counters cells. The first plane is used as a veto for charged particles while the second plane measures the energy of photons producing a shower in the converter.

MUON

The MUON spectrometer is a detector setup designed to measure muons from e.g. charmonium (J/ψ, ψ') and bottomonium (Υ, Υ', Υ'') decays or semi-leptonic heavy-flavor hadron decays. It is placed in negative z direction and covers $-4 < \eta < -2.5$ in pseudo-rapidity in the full azimuth. The MUON spectrometer has five tracking stations with two cathode pad planes each for two dimensional tracking. The tracking stations are preceded by a 413 cm long front absorber ($60\,X_0$) made of carbon and concrete to suppress hadrons from the interaction. A dipole magnet with a field strength of 0.67 T is placed around the third tracking station to measure the momentum of the muons. After the tracking stations a second iron absorber of 120 cm thickness is installed. Also the beam pipe is shielded with an absorber consisting of tungsten, lead and stainless steel. Two trigger chambers are installed behind the second shielding to trigger the read-out.

Due to the two absorbers, the minimal measurable muon momentum is $4\,\mathrm{GeV}/c$. The MUON spectrometer is designed to reach a mass resolution of $0.1\,\mathrm{GeV}/c^2$ at $10\,\mathrm{GeV}/c^2$ for the invariant mass of a $\mu^+\mu^-$ pair.

ACORDE

The ALICE COsmic Ray DEtector (ACORDE) is a scintillator detector array designed to trigger on cosmic rays. It has 60 modules placed on the three upper faces of the hexagonal L3 magnet and extends to $|\eta| < 1.3$ in pseudo-rapidity and $-60° < \varphi < 60°$ in azimuth. Each module consists of two combined scintillator counters with two photomultiplier tubes at the end to assure a detection rate higher than 90%. It is used as a trigger for cosmic muon measurements together with other detectors of ALICE. The high-energetic cosmic rays are used to determine the alignment between the detectors.

2.3 Data acquisition and reconstruction

Trigger

The detectors are triggered for read-out depending on the current running conditions. Inelastic collisions with only a few produced particles can occur. The triggering signal with the smallest bias to measure a collision is called “minimum bias”, MB. This can be to collect as many inelastic processes as possible using a triggering signal with the smallest bias (called “minimum bias”, MB). In ALICE the MB trigger is set as the requirement of a signal in either one of the V0 detectors (MBOR) or both of them (MBAND). The MBOR trigger has a higher trigger efficiency and was used in runs with low interaction rate, while for higher interaction rate the MBAND is used to increase purity. In addition there are various specific trigger setups to increase the statistics of rare physics processes. A complete list can be found in [89].

Data acquisition

In case of a triggered event the Central Trigger Processor (CTP) initiates the read-out of all detectors from the Frond End Electronics (FEE) to the Data AcQuisition System (DAQ) and to the High Level Trigger (HLT). The FEE is part of each detector converting and buffering the analogue detector signals until a signal from the CTP triggers the readout by the DAQ. The DAQ collects and combines all detector signals into an "event", which is send to a data storage facility. The HLT is able to pre-analyze detector signals such as the signals from the TPC. The HLT can form a decision for the DAQ whether to accept the event and also compress the detector signals to save bandwidth, depending on the mode of the HLT and DAQ. Upon acceptance of an event the DAQ sends all (compressed) detector signals to the storage.

Calibration

The condition of all detectors and addition parameters such as temperature and pressure is stored in a database called Offline Condition Database (OCDB) to assure proper calibration of all detectors. For the reconstruction of short data taking periods (runs) the parameters in the OCDB are used to do a first preliminary reconstruction of the events and tracks as described in the next paragraph. From this preliminary results the run specific calibration parameters are tuned for the detectors and updated in the OCDB. Then, the events are reconstructed in a "second pass" using the fully calibrated detectors.

Track reconstruction

The reconstruction of trajectories from charged particles is done in several steps as shown in Figure 2.3. The detector information is converted into "clusters", a digitization of the analogue signals. These clusters contain information about amplitude, time, and position of the signals measured in the detectors. Clusters from the two SPD layers are combined to "tracklets" that are used to determine a preliminary interaction vertex by finding the smallest distance between all tracklet vectors pointing inwards. Afterwards track candidates are searched at the outer edge of the TPC and propagated inwards. For this the Kalman filter technique [90] is used. The track is matched with tracklets in the ITS at the border of the ITS and propagated to the preliminary primary vertex. In a second step the track is propagated outwards to match all other possible detectors in the prolongation of the track path. A final inward propagation is done, where the track is refit to all associated clusters to obtain the best global fit for each track. Based on the reconstructed tracks the primary interaction vertex is determined.

Once the track finding is complete an automatic search for secondary vertices from photon conversions and weak decays of strange hadrons ($K^0_S, \Lambda, \Xi^\pm, \Omega^\pm$) is done.

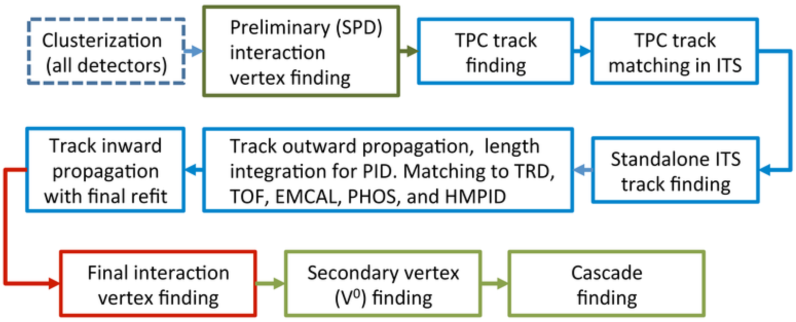

Figure 2.3: Steps of the track reconstruction process. Figure taken from [89].

3 Electrons from heavy-flavor hadron decays

The goal of this analysis is to measure the p_T-differential cross section of electrons from semi-leptonic charm- and beauty-hadron decays from p-Pb collisions at $\sqrt{s_{NN}} = 5.02\,\text{TeV}$ with ALICE at the LHC. After selecting events used for the measurement (Section 3.2) the tracks have to be selected according to specific criteria (Section 3.3) and the electrons are identified using the TPC and TOF detectors and the residual hadron contamination is estimated (Section 3.4). Finally, to extract the heavy-flavor decay signal, the background contributions, mainly electrons coming from Dalitz decays of light neutral mesons and γ-conversions, have to be subtracted (Section 3.5).

3.1 Data sample and Monte Carlo simulations

Data sample

In this section the data samples are described which have been used in this analysis to measure a yield of electrons from heavy-flavor hadron decays. Collisions between proton ($A = 1, Z = 1$) and lead ions ($A = 208, Z = 82$) at a center of mass energy (cms) of $\sqrt{s_{NN}} = 5.02\,\text{TeV}$ were recorded by the ALICE detector in the year 2013. The magnet design of the LHC enforces the same rigidity for both rotating beams, thus the beam energy of the proton (4 GeV) and the per-nucleon energy of the lead ion ($4 \cdot 82/208 = 1.58\,\text{TeV}$) differ. For this analysis data samples of collisions are used in which the proton beam is moving in direction to the C-side and the lead beam is moving in direction to the A-side (seen from the origin of the ALICE coordinate system). In ALICE a positive rapidity is defined in direction of the proton beam which results in a shift of the center-of-mass frame by $\Delta y = -0.465$ with respect to the lab frame. This means that particles measured perpendicular to the z axis in the ALICE acceptance do not have the rapidity ≈ 0 but are measured at slight backward rapidity.

In this analysis a data sample of about 10^8 events, corresponding to an integrated luminosity $L_{\text{int}} = (48.6 \pm 1.6)\,\mu\text{b}^{-1}$, is selected from the recorded p-Pb collision using a minimum bias (MB) trigger condition. The MB trigger for the p-Pb data taking required at least one hit in both of the backward/forward scintillator arrays V0A and V0C [89]. The data sample is split up into two data taking periods which has technical reasons due to changing of the detector conditions. ALICE has named the data samples “LHC13b” and “LHC13c”, which will be used in the following for reference to the two recording periods.

Simulations

To verify the analysis methods and correct for detector inefficiency and geometric acceptance Monte Carlo simulations were used. They include a simulation of the full detector material and detector response. The same reconstruction algorithms were used for the simulated detector response and the actual experimental data. Thus, the simulated MC sample is analyzed in the same way as the data sample: the same selection criteria for track candidates as for the experimental data are applied, which is described in the following section. The simulation uses the Heavy-Ion Jet Interaction Generator (HIJING [91]) as event generator and GEANT3 [92] for the particle propagation and detector response simulation. In the MC production a charm and beauty hadron sample is embedded in order to increase the statistics of heavy-flavor decay electrons. In each event generated by HIJING an event from the PYTHIA [93] event generator (with a special tuning set called "Perugia0" [94]) is embedded. In the sample half of the events are forced to include a $c\bar{c}$ or $b\bar{b}$ pair with at least one electron from the decay of a heavy-flavor hadron.

3.2 Event selection

The data sample consists of 121 million events selected with the minimum bias trigger. Not only p-Pb collisions but also beam-gas collisions and multiple beam-beam interactions can lead to a minimum bias trigger. To remove these types of events the following event selection criteria are applied:

- One of the most important quantities is the position of the primary interaction vertex. Global tracks, reconstructed in the TPC and ITS, are used to locate the interaction vertex with high precision. Only events with at least two tracks and a vertex found within 10 cm from the center of the detector along the beam line are used in the analysis ($|z_{\mathrm{vtx}}| < 10$ cm). The value of the primary vertex cut is chosen to ensure a uniform reconstruction efficiency of charged particles.
- The primary interaction vertex can also be estimated using the two innermost layers (SPD) of the ITS. If the absolute difference between the primary vertex estimated in the two strategies is larger then 0.5 cm the event is rejected.

The distributions of the z-vertex position and the selection applied is shown in the top panel of Figure 3.1. The distributions from both data taking periods agree reasonable with each other within the selected range as shown in the bottom panel. After this selection around 100 million events remain for the analysis.

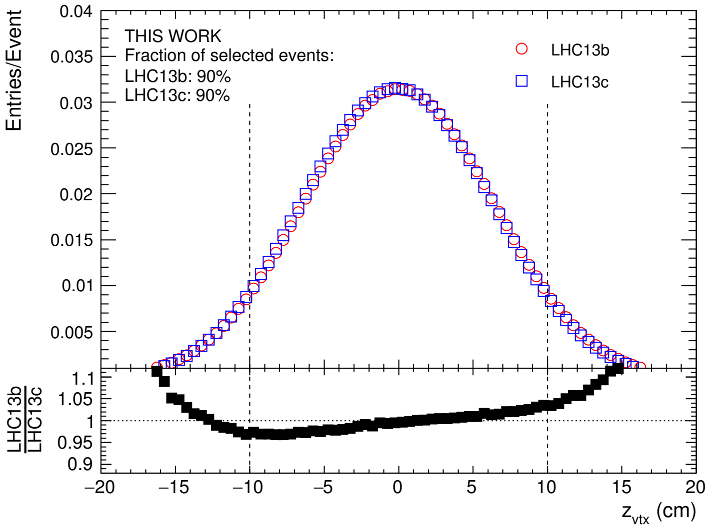

Figure 3.1: Top panel: distribution of the z-vertex position with respect to the ALICE coordinate system. The selection range of ±10 cm is indicated by the dashed lines. Bottom panel: ratio between both distributions

Table 3.1: Overview of the standard track selection criteria.

Observable	Cut value
TPC and ITS refit	required
χ^2/TPC cluster	< 4
Kink daughters	rejected
Number of ITS clusters	≥ 4
Requirement of SPD pixels	both
Number of TPC clusters	≥ 100
Number of TPC $\mathrm{d}E/\mathrm{d}x$ clusters (PID clusters)	≥ 80
Ratio found/findable TPC clusters	> 0.6
DCA to the primary vertex in radial direction	< 1 cm
DCA to the primary vertex in z-direction	< 2 cm

Electron candidate tracks are required to fulfill several track selection criteria (summarized in Table 3.1). The distributions for the track variables have been compared for experimental data and for the MC simulation and were found to be in agreement. The calibration of the pseudo-rapidity dependence of the TPC $\mathrm{d}E/\mathrm{d}x$ signal was found retain a residual bias which becomes significant for $\eta > 0.6$. Therefore, the tracks were restricted in the analysis in pseudo-rapidity to $|\eta| < 0.6$. To suppress reconstructed tracks with a large fraction of random uncorrelated clusters from other tracks the χ^2/NDF for the track fitted to all associated clusters has to be smaller than 4. Because clusters are not shared between tracks, the ratio of found over findable[1] clusters has to be larger than 60%. Particles which decay in flight or scatter on detector material are called kinks due to the discontinuity of their track path. The track is split at the kink on reconstruction level into mother and daughter tracks. Kink daughters are always rejected since these tracks are from decays and not electrons. Due to a high fraction of false-positives kink mothers are kept. The final refit of the global track with the Kalman filter back to the identified primary vertex is required to pass through the ITS and TPC for each track candidate. The track candidates are required to have a signal in both SPD pixel layers, to suppress the contribution of electrons from γ-conversions in the first layers of the ITS. Furthermore, two additional hits are required in the other 4 layers of the ITS. Since electron tracks, in the considered momentum range ($p > 0.5\,\mathrm{GeV}/c$), are already on their Fermi plateau when losing energy in the TPC, the average number of clusters per track is higher than for hadrons (the hadron Fermi plateau is at $p > 20\,\mathrm{GeV}/c$). Thus the number of clusters for tracks coming from electrons is on average higher than for other particles. By selecting 100 out of 159 clusters for the reconstruction of the track purity of the electron candidate sample is increased. Since edge effects can distort the $\mathrm{d}E/\mathrm{d}x$ measurement, clusters at the sector edges are not considered for the $\mathrm{d}E/\mathrm{d}x$ calculation. Clusters considered are called “PID clusters”. For a proper particle identification a minimum number of 80 clusters is required to compute the $\mathrm{d}E/\mathrm{d}x$. In order to reject trajectories from particles coming from decays of strange hadrons or interactions with the beam pipe, the Distance of Closest Approach (DCA) for track candidates to the primary vertex is calculated. Tracks are required to be within 2 cm of the z position and 1 cm of the radial (xy) position of the vertex.

---

[1] Findable clusters are all clusters who should give a signal according to the reconstructed trajectory.

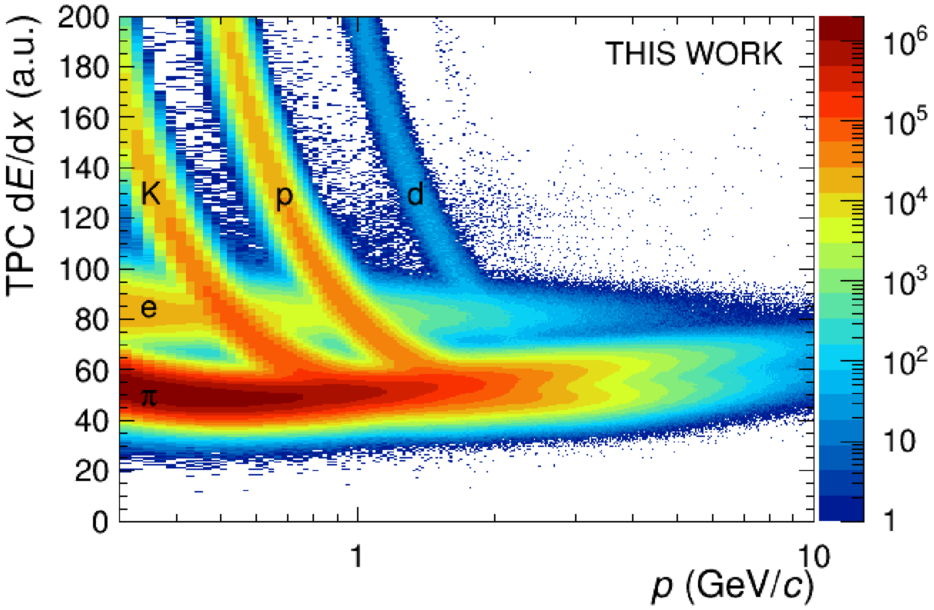

Figure 3.2: The specific energy loss $\mathrm{d}E/\mathrm{d}x$ for track candidates in the TPC as function of momentum. The bands for kaons, protons, deuterons, electrons and pions are indicated.

The removed yield of electrons from heavy-flavor hadron decays is negligible due to the much smaller decay lengths of heavy-flavor hadrons (100–500 μm).

3.4 Electron identification

ALICE has several detectors that can be used to identify electron candidates, which are efficient in different momentum regions. However, since each detector has only a limited acceptance and detection efficiency, it is necessary to optimize the usage of the detectors. Electrons are identified using the TOF detector and the TPC detector of ALICE. The energy loss $\mathrm{d}E/\mathrm{d}x$ is in general described by the Bethe-Bloch parametrization [7]. The specific energy loss for electrons is already at the Fermi plateau for the momentum scales of this measurement ($p_\mathrm{T} > 0.5\,\mathrm{GeV}/c$) and thus has no momentum dependence as it can be seen in Figure 3.2. However, the Bethe-Bloch lines of kaons, protons and deuterons cross the constant electron energy loss at momenta of 0.4–0.6 GeV/c, 0.8–1.2 GeV/c and $\sim 2\,\mathrm{GeV}/c$, respectively. As described in section 2.2, the TOF detector of ALICE can separate kaons, protons and deuterons at low momentum ($p < 2.5\,\mathrm{GeV}/c$). Figure 3.3a shows the time of flight for track candidates relative to the expected time of flight for electrons normalized to the resolution.

Therefore, the TOF detector is only used below $p < 2.5\,\mathrm{GeV}/c$ with a symmetric 3σ selection around the expected time of flight for electrons. In Figure 3.3b the TOF PID selection is applied exemplarily for the whole momentum range p . The specific energy loss $\mathrm{d}E/\mathrm{d}x$ is shown relative to the expected energy loss of electrons $\langle \mathrm{d}E/\mathrm{d}x\rangle_e$ and normalized to the TPC resolution(σ). In the following this will be abbreviated as "$\sigma_{\mathrm{e-TPC}}$". With respect to Figure 3.2 the $\mathrm{d}E/\mathrm{d}x$ bands of kaons, protons and deuterons are strongly suppressed.

In the momentum region $p < 2.5\,\mathrm{GeV}/c$, where the TOF is used, the requirement on the normalized TPC $\mathrm{d}E/\mathrm{d}x$ is $-0.5 < \sigma_{\mathrm{e-TPC}} < 3$. At higher momentum, where the pion band

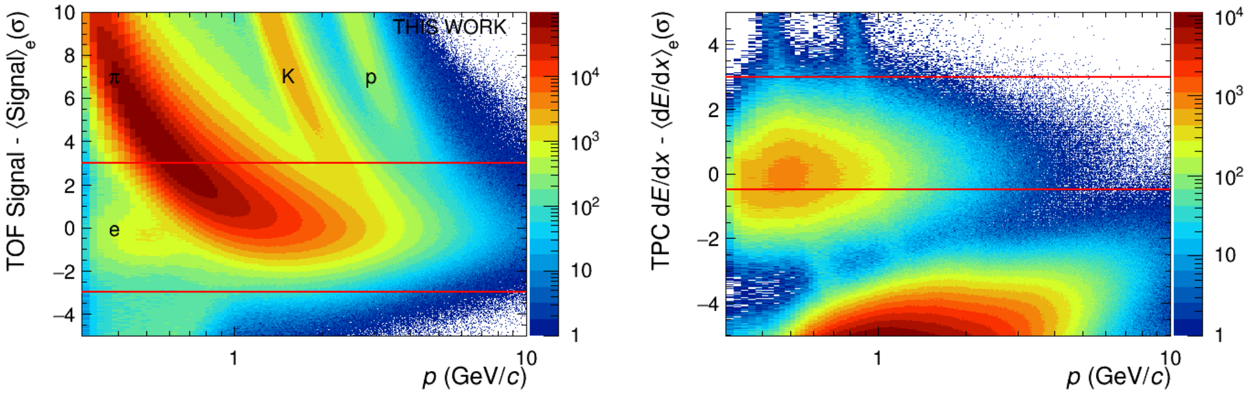

(a) Time of flight for particles relative to the expected time of flight for electrons divided by the TOF resolution as function of momentum. The bands for kaons, protons, electrons and pions are indicated. The red lines indicate the selection criteria ($-3 < \sigma < 3$) for electron candidates.

(b) The specific energy loss $\mathrm{d}E/\mathrm{d}x$ for electron candidates selected with TOF relative to the expected $\mathrm{d}E/\mathrm{d}x$ for electrons and divided by the TPC resolution as function of momentum. The red lines indicate the selection criteria ($-0.5 < \sigma < 3$). Published in [69].

Figure 3.3: Electron identification with TOF and TPC.

merges into the electron band due to the relativistic rise, a more stringent selection criterion than at low momentum is applied ($-0 < \sigma_{\mathrm{e-TPC}} < 3$).

3.4.1 Statistical removal of remaining hadron contamination

The selected electron candidate sample still contains a contribution from hadrons which cannot be separated. The hadron contribution needs to be estimated and subtracted statistically. The distribution of $\sigma_{\mathrm{e-TPC}}$ is analyzed in narrow momentum slices and shown exemplarily in the momentum range $5\,\mathrm{GeV}/c < \mathrm{p} < 9\,\mathrm{GeV}/c$ in Figure 3.4. The hadron contamination for $p < 5\,\mathrm{GeV}/c$ was found to be negligible for this measurement. To determine the momentum dependent fraction of the hadron contamination, the distributions are fitted with parametrizations of the electron, pion and kaon peak. For the electron peak a Gaussian distribution is used and a Landau function for the pion distribution [95]. The fits are shown for four momentum slices in Figure 3.4 where the peaks from the relative energy loss $\mathrm{d}E/\mathrm{d}x$ of kaons, pions and electrons are visible in each panel. The fraction of hadron contamination is calculated as the ratio of the numerically integrated peaks in the selection region. In Figure 3.5 the contamination fraction is plotted as function of the momentum. The hadron contamination as function of momentum is fitted with an error function parametrization:

$$F_{\mathrm{hadron}}[p] = p_0 + p_1 \cdot \mathrm{Erf}(p_2 * p + p_3) \tag{3.1}$$

A larger selection window for $\sigma_{\mathrm{e-TPC}}$ leads to higher systematic uncertainties on the PID due to the increasing hadron contamination. A smaller window results in higher statistical uncertainty due to a reduced number of selected tracks. The TPC selection of $-0 < \sigma_{\mathrm{e-TPC}} < 3$ was chosen to allow for a relative small fraction of hadron contamination up to $8\,\mathrm{GeV}/c$ with sizable statistics to keep the statistical and systematical uncertainty to a minimum.

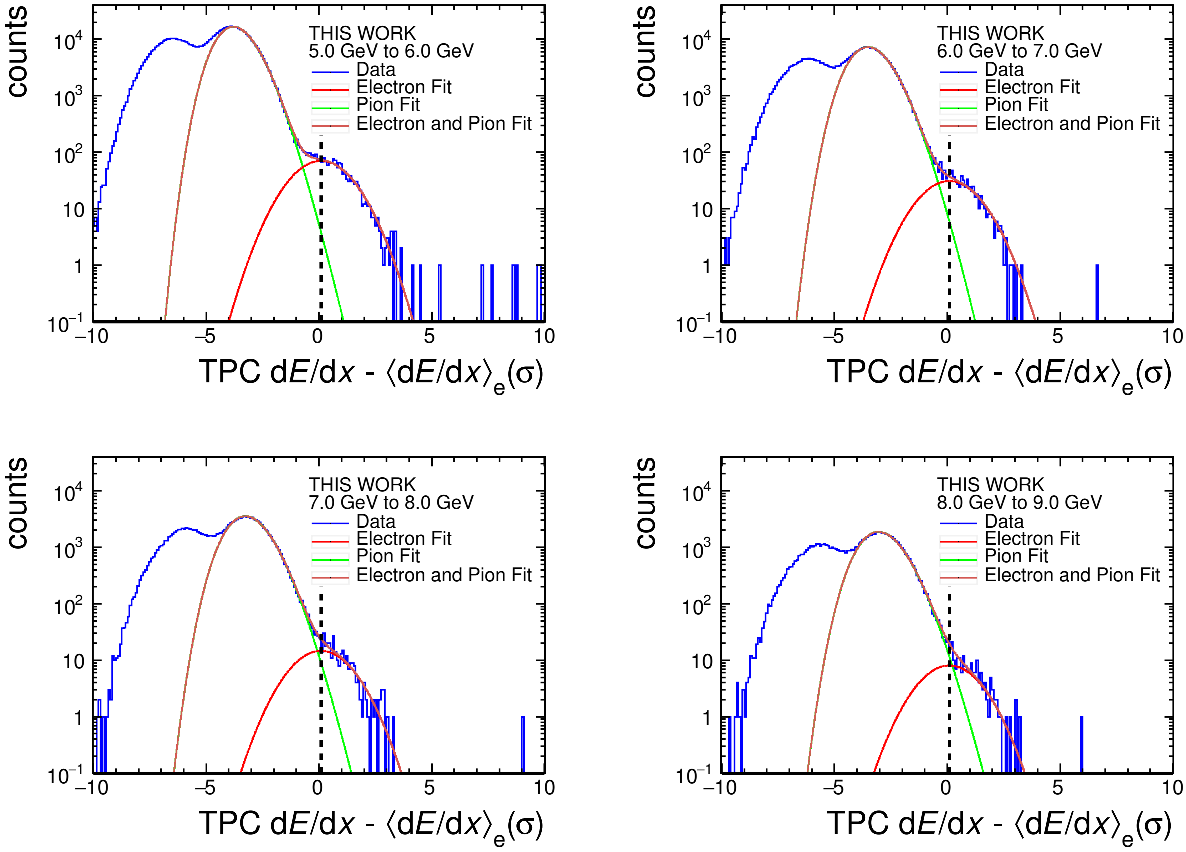

Figure 3.4: The $\mathrm{d}E/\mathrm{d}x$ relative to the average electron $\mathrm{d}E/\mathrm{d}x$ in units of σ for different momenta. The distribution of the electron $\mathrm{d}E/\mathrm{d}x$ centered around zero is fitted with a Gaussian. The middle peak reflects the pion $\mathrm{d}E/\mathrm{d}x$ and is moving towards the electron peak for increasing momentum. A Landau parametrization with an added exponential tail is fitted to the pion distribution.

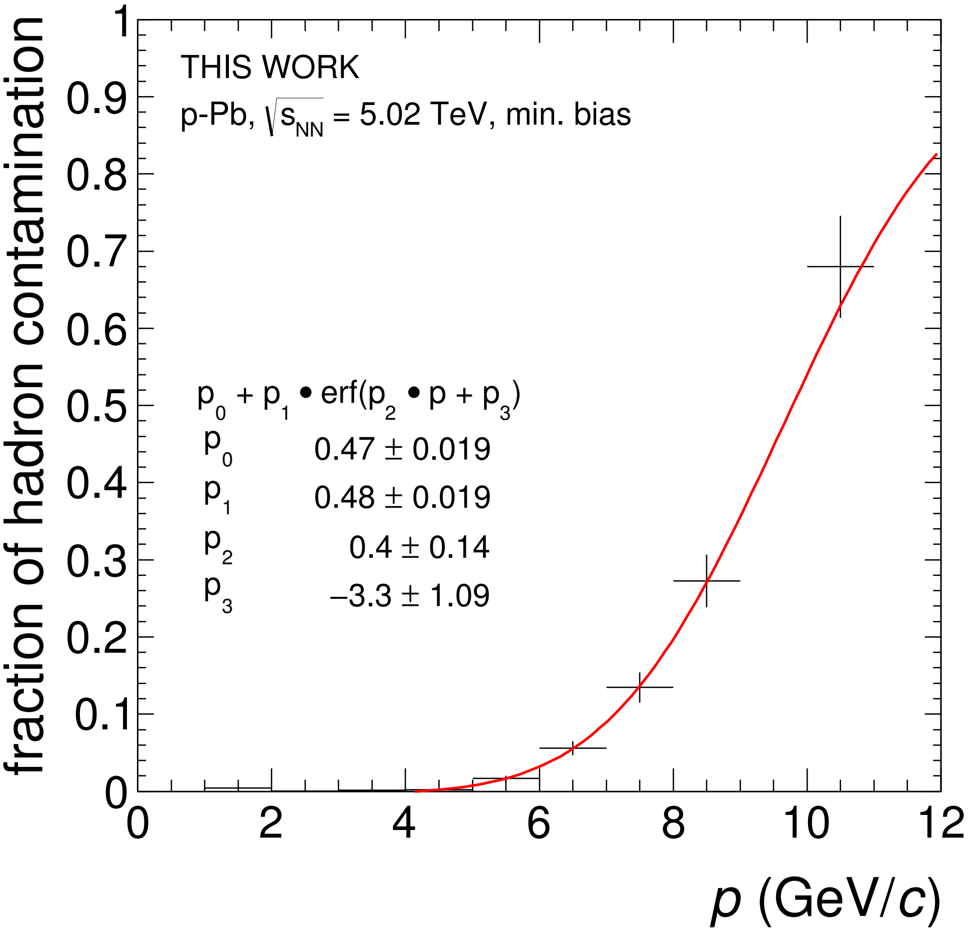

Figure 3.5: Fractional hadron contamination as function of momentum. The line indicates an error function parametrization which is fit to the contamination.

3.5 Background subtraction

Since the semi-leptonic decay of heavy-flavor hadrons always includes a neutrino, it is not possible to reconstruct the full decay topology. Thus, it is not possible to identify the electrons from heavy-flavor hadron decays directly but statistical methods need to be used. The majority of the electron background is coming from the Dalitz decay of light neutral mesons (e.g. $\pi^0 \rightarrow e^+e^-\gamma$) or photons (e.g. $\pi^0 \rightarrow \gamma\gamma$) which convert to e^+e^- in the detector material. In a previous analysis for pp collisions at $\sqrt{s} = 7\,\text{TeV}$ it was estimated that these Dalitz decays and γ-conversions constitute more than 90% of the background [96]. A much smaller contribution called "K_{e3}" is from weak kaon decays, which decays into a pion, an electron, and a neutrino. The K_{e3} contribution is only significant at $p_{\text{T}} < 2\,\text{GeV}/c$. The dielectron decay of quarkonia (J/ψ) becomes a significant contribution to the background at $p_{\text{T}} > 3\,\text{GeV}/c$. The last significant contribution is from primary real and virtual photons, which are created directly in hard scattering processes.

An essential part of the analysis is the determination and subtraction of the electron background. In the following two different methods of background subtraction are discussed.

The first method relies on the calculation of a so called "cocktail" of all background sources of electrons. It relies on measured cross sections of light hadrons and is therefore limited by their systematic uncertainties. This method was used previously in similar analysis in the PHENIX Collaboration [55, 97] and the ALICE Collaboration [96, 98]. The second method takes advantage of the fact that the main source of background electrons are light meson Dalitz decays and the conversion of photons in the detector. Both processes always produce a correlated electron-positron pair with a small invariant mass. This method was used for similar analysis in the STAR Collaboration [68]. While previous measurements of electrons from heavy-flavor hadron decays with ALICE used the cocktail based subtraction, this work describes the first measurement using the tagging of photonic electrons to determine the electron background in ALICE [69].

3.5.1 Cocktail method

In the cocktail based subtraction all significant contributions to the electron background are estimated separately and summed up. The p_{T}-differential cross section of the different hadrons contributing to the background are needed as an input to a Monte Carlo decayer, which forces the decay to electrons. The most important input is the neutral pion spectrum since it contributes the largest part to the background spectrum. At the time of the analysis a π^0 measurement was not available and thus the spectrum of the charged pions was used, approximating $\text{d}\sigma_{\pi^0}/\text{d}p_{\text{T}} = (\text{d}\sigma_{\pi^+}/\text{d}p_{\text{T}} + \text{d}\sigma_{\pi^-}/\text{d}p_{\text{T}})/2$. This approximation is valid using isospin symmetry, where the pion family forms a triplet. The charged pion spectra were measured at low p_{T} [75] and high p_{T} [99] by the ALICE Collaboration. The combined spectra were parametrized with a Tsallis function [100]:

$$E\frac{\text{d}^3\sigma}{\text{d}p^3} = C\frac{(n-1)(n-2)}{nT(nT+m(n-2))}(1+(m_{\text{t}}-m)/(nT))^{-n}, \tag{3.2}$$

with $m_{\text{T}} = \sqrt{m^2 + p_{\text{T}}^2}$ being the transverse mass and C, n and T being fit parameters. Other light meson spectra $(\eta, \eta', \rho, \omega$ and $\phi)$ were calculated using m_{T} scaling [101] of the Tsallis parametrization of the pion spectrum. m_{T}-scaling is an approach to calculate heavier meson

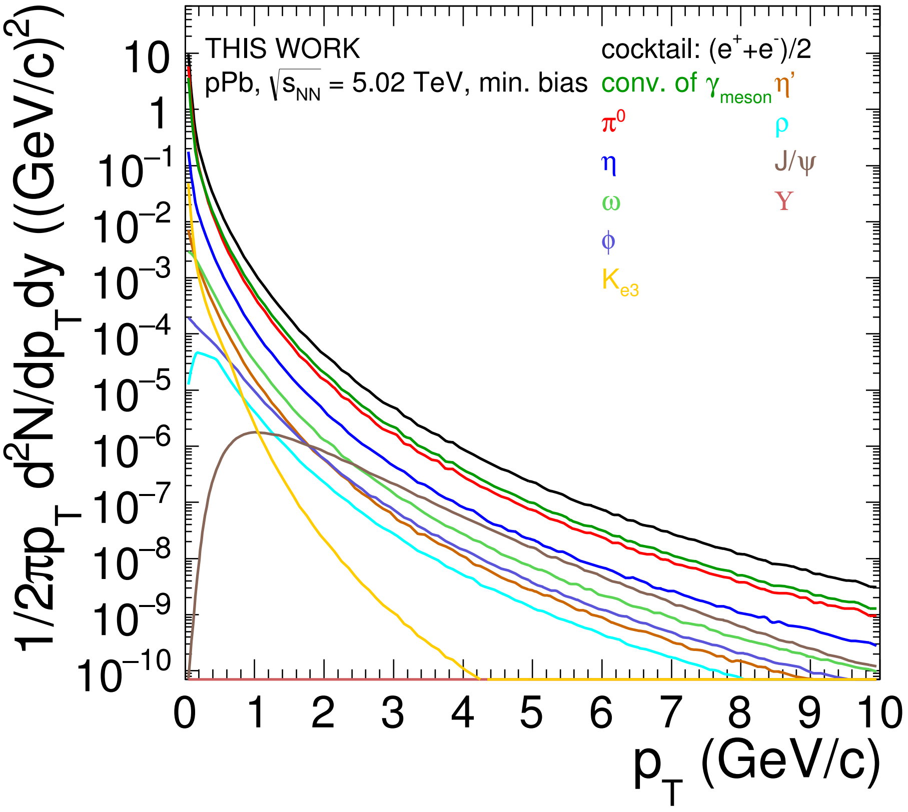

Figure 3.6: The different contributions to the background cocktail as function of p_{T}.

spectra assuming that the shapes of pion and heavier meson spectra are the same as function of $m_{\mathrm{T}} = \sqrt{p_{\mathrm{T}}^2 + m^2}$. The normalization factors between the different relative light meson m_{T} spectra were obtained from PHENIX [102] assuming negligible changes for the ratios at higher $\sqrt{s_{\mathrm{NN}}}$. The agreement between m_{T} scaled spectra and measurements was shown by PHENIX [102] and by ALICE [96] through a comparison of the measured η spectrum with an m_{T} scaled π^0 spectrum. The systematic uncertainties of the pion spectrum were propagated by moving the pion spectrum up/down by the systematic uncertainties and refitting with Tsallis parametrizations.

A source of electrons at low transverse momentum is the weak decay of kaons, known as $\mathrm{K_{e3}}$ ($K^{\pm} \rightarrow \pi^0 \nu_e \mathrm{e}^{\pm}, K^0_{\mathrm{L}} \rightarrow \pi^{\pm} \nu_e \mathrm{e}^{\mp}$). Kaons have a non negligible branching ratio (5%/40% [7]) into the decay to a pion, an electron/positron and the respective neutrino. Due to the neutrino, it is not possible to measure the cross section directly. The contribution to the background cocktail is estimated by extracting an electron spectrum from $\mathrm{K_{e3}}$ decays in a PYTHIA [93] simulation using GEANT3 [92] for the detector response and normalize this to the total cocktail. This relative yield as function of p_{T} is then multiplied with the actual cocktail distribution as described above. The $\mathrm{K_{e3}}$ contribution is small, i.e. 3% of the yield of electrons from heavy-flavor hadron decays for $p_{\mathrm{T}} \leq 1.5\,\mathrm{GeV}/c$. Due to the large uncertainty of this method, a 100% systematic uncertainty is assigned to the cross section of electrons from $\mathrm{K_{e3}}$ decays.

The decay of J/ψ to e^+e^- is a non negligible source of background at high p_{T}. The p_{T}-differential cross section of J/ψ in p-Pb collisions at $\sqrt{s_{\mathrm{NN}}} = 5.02\,\mathrm{TeV}$ was parametrized as described in [103]. Results from different beam energies were used to obtain an empirical parametrization of the p_T-differential J/ψ cross section as function of $\sqrt{s}$. The parametrized cross section was scaled with N_{coll} and used as input to the Monte Carlo cocktail used to evaluate the p_T-differential cross section of single electrons from J/ψ decays in the rapidity window $|y_{lab}| < 1$. The resulting cross section is approximately 3% of the cross section of electrons from heavy-flavor hadron decays for $p_T \geq 1.5\,\mathrm{GeV}/c$. A systematic uncertainty of 50% is assigned to the cross section due to the assumption of binary scaling and not including any possible cold nuclear matter effects. The parametrized cross section is in good agreement to a later publication with the J/ψ cross section measured in p-Pb collisions with ALICE [104].

3.5.2 Photonic tagging method

The main contribution to the background of electrons not coming from heavy-flavor hadron decays is from the Dalitz decay and $\gamma\gamma$ decay of π^0 and η mesons. The photons are actually much more abundant than the electrons from Dalitz decays but they only convert to electron-positron pairs in the beam pipe or detector material, which is optimized to a small thickness (about 10% conversion probability in the whole ITS and TPC [89]). These produce so-called photonic electrons, which means they originate from particle decays where real or virtual photons are emitted. Electrons from photon conversions and Dalitz decays always come as an electron and positron pair with a very small invariant mass value (photon conversion) or an invariant mass up to almost the meson mass (Dalitz). This can be exploited to select electrons from photonic sources, because heavy-flavor hadron decays do not produce low-mass e^+e^- pairs. In a first step the yield of correlated electron-positron pairs, i.e. those coming from the same decay, have to be separated from random, uncorrelated combinations of electrons and positrons. In a second step the photonic yield has to be corrected for the limited acceptance and finite detector efficiencies (e.g. one leg of the e^+e^--pair propagates in a direction outside of the geometrical acceptance of ALICE) based on MC simulations.

Raw photonic electron yield

The determination of the p_T-differential yield of electrons from photonic decays is done statistically with respect to the number of electron candidates in the following steps:

Find possible partners:
To find the partner for an electron candidate from a photonic decay, the electron and positron candidates are combined. Tracks fulfilling the so-called “associated partner” selection criteria are selected for further analysis. The latter selection criteria are less stringent compared to the standard electron candidate selection criteria to maximize the probability of finding the photonic partner. The criteria are summarized in Table 3.2.

Combine to invariant mass spectrum:
Each electron candidate is then combined with all associated partners of opposite charge (“unlike-sign”) in the same event and an invariant mass spectrum is filled ($N_{\mathrm{ULS}}[p_T]$). The invariant mass of the e^+e^- pair is required to be less than $150\,\mathrm{MeV}/c^2$ in order to include all electrons from γ conversions and π^0 Dalitz decays, while e^+e^- pairs from other light mesons (such

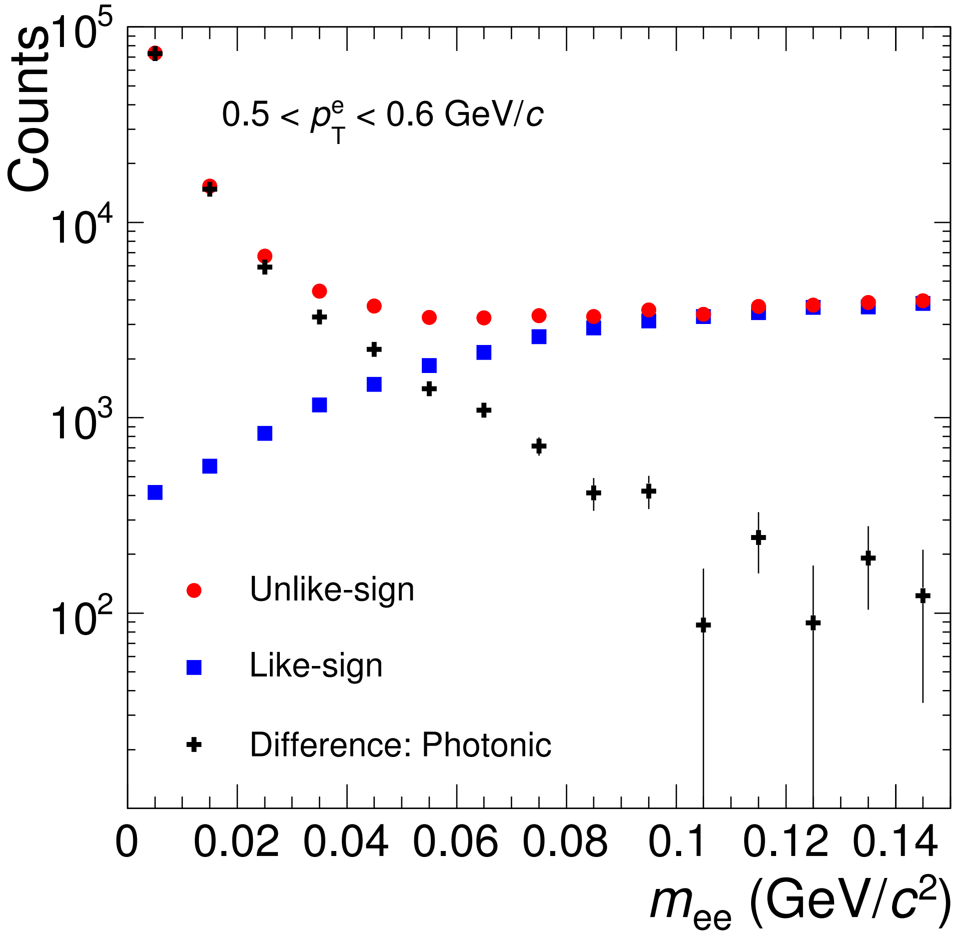

Figure 3.7: Invariant mass distributions of unlike-sign and like-sign electron pairs for the inclusive electron p_T interval $0.5 < p_T < 0.6\,\mathrm{GeV}/c$. The difference between the distributions is the photonic contribution. Published in [69].

as η, ω and η') are only included for e^+e^- pairs with invariant mass smaller than $150\,\mathrm{MeV}/c^2$. However, due to the small contribution of other light meson to the electron background [105], the difference is negligible. The yield of unlike-sign pairs fulfilling the selection criteria is filled in invariant mass spectra for each p_T interval of the electron candidate. In Figure 3.7 an example of the range $0.5 < p_T < 0.6\,\mathrm{GeV}/c$ is represented by the red circles.

Estimate uncorrelated pairs:

The combinations of electron candidates and associated partners include many uncorrelated, random pairs. To estimate the contribution of uncorrelated pairs in the invariant mass distribution, the so called “like-sign” subtraction method is used. Each electron candidate is combined with all “like-sign” associated partners of the same charge ($N_{LS}[p_T]$). The invariant mass spectrum of like-sign pairs is used to model the uncorrelated contribution in the invariant mass distribution of unlike-sign pairs. The acceptance of like-sign and unlike-sign e^+e^- pairs is assumed to be equal, in agreement with results of low-mass dielectron measurements in p-Pb collisions by ALICE [105]. The invariant mass spectrum of uncorrelated like-sign pairs is shown in Figure 3.7 as blue squares.

Table 3.2: Selection criteria for the associated tracks

track property	selection criterion
ITS and TPC refit	required
ITS clusters	≥ 2
TPC clusters	≥ 60
TPC dE/dx clusters	≥ 60
DCA radial	< 1cm
DCA z	< 2cm
$\lvert\sigma_{\mathrm{e-TPC}}\rvert$	< 3

Calculating the photonic yield:

The invariant mass distribution of like-sign pairs is subtracted from the distribution of unlike-sign pairs as shown in Equation 3.3. The remaining yield ($N_{\mathrm{photonic,raw}}\left[p_{\mathrm{T}}\right]$) for $m \leq 150\,\mathrm{MeV}/c^2$ is identified as the yield of electron candidates coming from photonic decays, shown as black crosses in Figure 3.7. The shape of the invariant mass spectrum is in agreement with Monte Carlo simulations showing a peak at zero invariant mass due to the photon conversions and a continuous spectrum (peaked at very low mass) to higher invariant mass from the Dalitz decays.

$$N_{\mathrm{photonic,raw}}\left[p_{\mathrm{T}}\right] = N_{\mathrm{ULS}}\left[p_{\mathrm{T}}\right] - N_{\mathrm{LS}}\left[p_{\mathrm{T}}\right] \tag{3.3}$$

Tagging efficiency

The raw spectrum of electron candidates from photonic decays needs to be corrected for cases where the photonic partner is not reconstructed. An efficiency needs to be evaluated which gives the conditional probability to find the partner among the associated candidates for an electron candidate which has decayed in a photonic decay. This efficiency is called “tagging efficiency” $\varepsilon_{\mathrm{tag}}$. The true Monte Carlo information is used for each pair to only select candidates for which the photonic partner was found. This is done by checking that the pair comes from the same mother particle in the MC simulation. $\varepsilon_{\mathrm{tag}}$ is calculated as the number of found pairs divided by the total number of electrons which originate from photonic sources as known from MC truth. The method was cross checked with an alternative approach. The number of photonic pairs is calculated in the same way as described in the previous section: the like-sign pair spectra are subtracted from the unlike-sign pair spectra for each p_{T} interval using spectra obtained from the MC simulation. In Figure 3.8 the tagging efficiency $\varepsilon_{\mathrm{tag}}$ is plotted as a function of the transverse momentum for both methods of estimating the number of photonic pairs. Results from both methods agree within the statistical uncertainties.

As mentioned before, due to the invariant mass selection criterion of $m \leq 150\,\mathrm{MeV}$, the Dalitz decays of light mesons heavier than the π^0 are not measured completely. This results also in a negligible change of the tagging efficiency (2%), which is reflected in the evaluation of the systematic uncertainties (see Table 3.5).

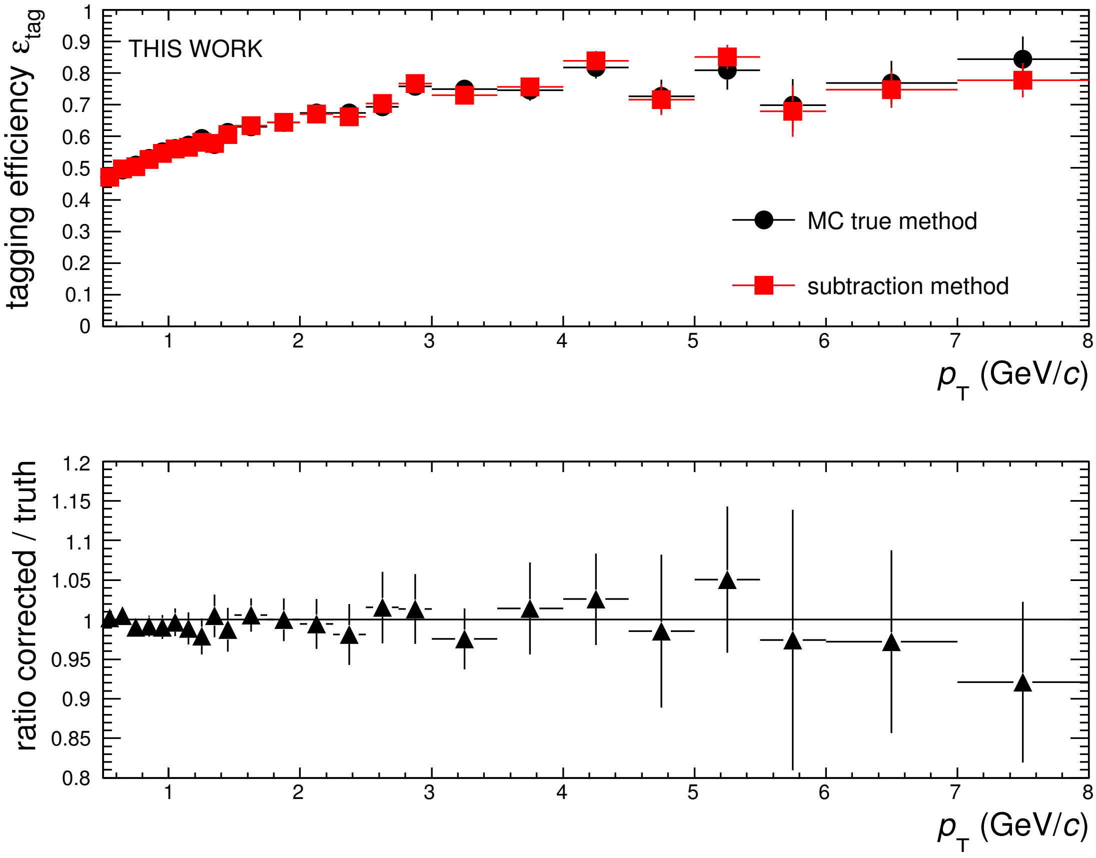

Figure 3.8: Comparison of the tagging efficiency obtained with two different methods of evaluating the number of tagged photonic pairs.

Correction for Monte Carlo

As described in the previous section, the p_T-dependent tagging efficiency gives the conditional probability to reconstruct the associated photonic partner. The decay kinematics for the Dalitz decay are dependent on the momentum of the meson, e.g. the opening angle between the e^+e^--pair is decreasing for increasing momentum. This means, for a higher relative abundance of mesons with high momentum, the opening angle of the e^+e^--pair in the Dalitz decay is on average smaller. This results in a higher probability to reconstruct the associated partners. Generally speaking the distribution of Dalitz decay electrons and thus ε_{tag} is dependent on the shape of the p_T-differential cross section of the photonic sources, namely light mesons such as π^0, η, ω, ϕ, η' and ρ.

The cross sections used in the Monte Carlo simulations do not reproduce the cross sections measured in the experiment, thus a correction is necessary. For this, p_T-dependent weights are applied to the meson spectra in the MC simulation. The weights are calculated as ratios of measured (or m_T-scaled) spectra and spectra from Monte Carlo. The measured π^0 spectrum and the m_T-scaled spectra for η, ω, ϕ, η' and ρ were used from the parametrizations for the cocktail method, as explained in the previous section (3.5.1).

The spectra in Monte Carlo were extracted from the reconstructed simulation data by scanning through the MC stack and selecting primary π^0, η, ω, ϕ, η' and ρ mesons.

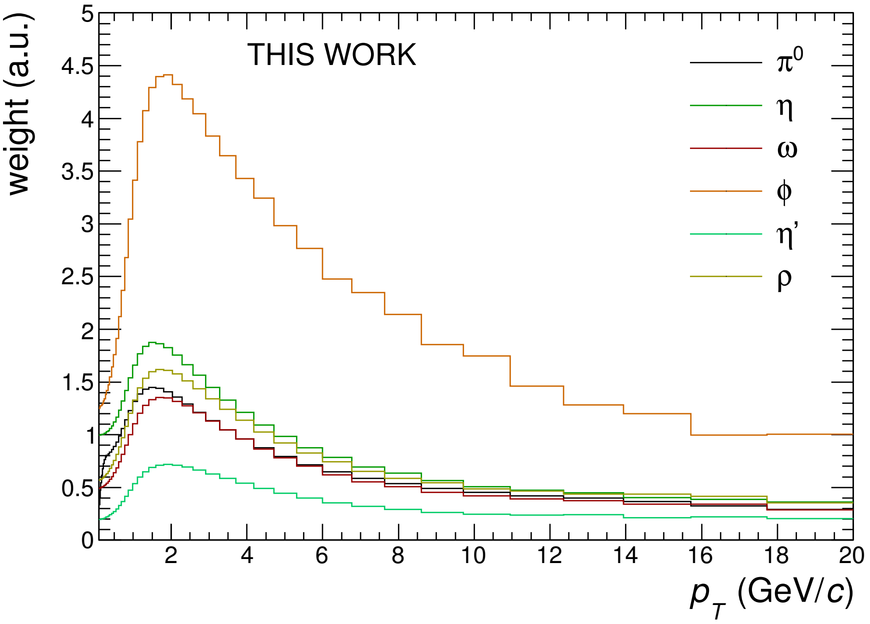

Figure 3.9: Weighting functions for light mesons with considerable contribution to the electron background.

The weights as shown in Figure 3.9 are applied to each identified electron of photonic origin. The p_T-dependent weight for the respective (mother) meson from Figure 3.9 is applied to the photonic electron. Thus the spectra of electrons from meson Dalitz decays and γ conversions of decay photons of these are weighted properly to resemble the spectral shapes observed in the experimental data. The corrected yield of photonic electrons N_photonic is determined as:

$$N_\mathrm{photonic}\left[p_\mathrm{T}\right] = \frac{N_\mathrm{ULS}\left[p_\mathrm{T}\right] - N_\mathrm{LS}\left[p_\mathrm{T}\right]}{\varepsilon_\mathrm{tag}\left[p_\mathrm{T}\right]} \tag{3.4}$$

with the meson cross section corrected p_T-dependent tagging efficiency ε_tag and the p_T-dependent invariant mass spectra of like-sign N_LS and unlike-sign pairs N_ULS.

3.6 Efficiency correction and normalization

The raw electron yield needs to be corrected for the finite geometrical acceptance ε_geo of the detector, the efficiency to reconstruct the tracks $\varepsilon_\mathrm{reco}$ and the efficiency of the electron identification ε_eID. The combined efficiency ε is estimated by a Monte Carlo simulation (see Section 3.1). A selection criterion is applied to remove particles produced far away from the production vertex ($< 1\%$), because these tracks were filtered in the calibration of the experimental data. The vertex of generated particles has to be within ± 15 cm in z-direction and within 3 cm in the xy-plane with respect to the geometric center of the detector. Then, all selection criteria described in 3.3 are applied except for the TPC eID selection. The p_T-differential efficiency of the track selection can be calculated by dividing the electron spectra obtained from the MC simulation before and after the track selection. The p_T-differential efficiency is shown in Figure 3.10. The

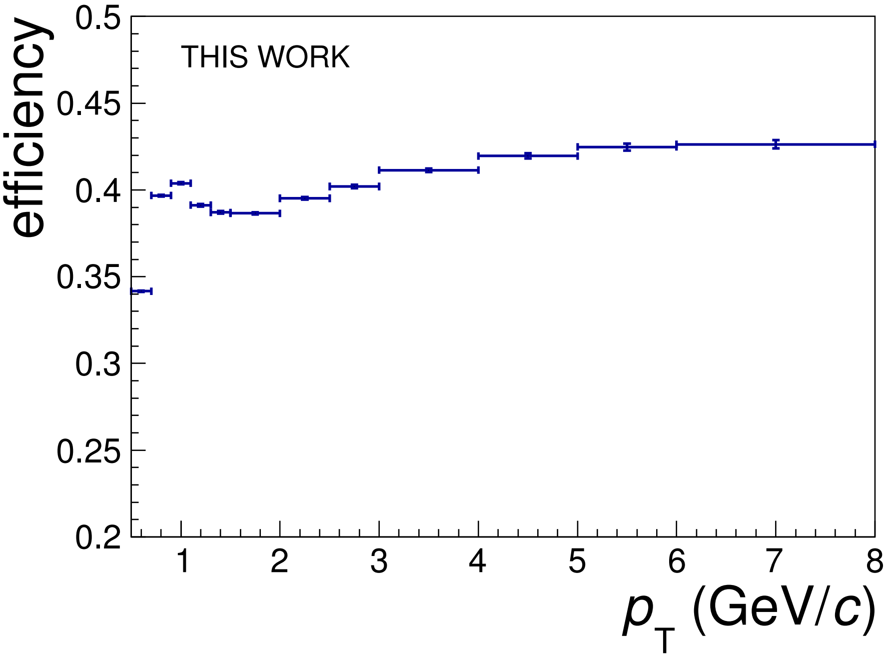

Figure 3.10: Transverse-momentum dependent acceptance and efficiency ($\epsilon^{\text{geo}} \times \epsilon^{\text{reco}} \times \epsilon^{\text{eID}}(\text{TOF})$) for electrons from heavy-flavor hadron decays calculated from a MC simulation applying all selection criteria of the measurement (except TPC PID).

PID efficiency of the TPC is independent of the track p_T. As explained in Section 3.4, the TPC $\mathrm{d}E/\mathrm{d}x$ normalized to the expected $\mathrm{d}E/\mathrm{d}x$ of electrons can be described by a Gauss distribution. The efficiency of the TPC PID selection can thus be calculated as the definite integral of a Gauss distribution in narrow momentum slices. For the analysis using TPC and TOF detector the selection criteria of ($-0.5 < \sigma_{\text{e-TPC}} < 3$) was used which results in a TPC efficiency of 0.69, while for the TPC only analysis the selection of ($0 < \sigma_{\text{e-TPC}} < 3$) results in an efficiency of 0.5.

To obtain the true spectrum of electrons from heavy-flavor hadron decays effects due to the limited detector resolution and bremsstrahlung need to be taken into account. Without a corresponding correction the measured electron p_T distribution is not equal to the true p_T distribution. Mathematically this relation can be expressed as a matrix multiplication: A true (by nature) p_T distribution/vector is folded with the detector response matrix **R** to the measured p_T distribution "M". To obtain the true spectrum T, the measured spectrum M needs to be "unfolded" by $\mathbf{R}^{-1}$ [106, 107]:

$$M = \mathbf{R} \cdot T \tag{3.5}$$

$$T = \mathbf{R}^{-1} \cdot M \tag{3.6}$$

While it is intrinsically not possible to obtain the true response matrix **R**, the detector response and bremsstrahlung can be modeled with GEANT3 with (run)time dependent input. Thus an approximate response matrix can be obtained from Monte Carlo simulations. **R** is the correlation matrix between the measured and reconstructed p_T. However, the inversion is usually not trivial because the matrix can be singular. Thus a so called "smearing matrix" is calculated, which approximates the inverse matrix: $\widetilde{\mathbf{R}} \approx \mathbf{R}^{-1}$. Bayes' Theorem is used to calculate the matrix elements $\widetilde{\mathbf{R}}_{ji}$ based on the response matrix $\mathbf{R}$:

$$P(A|B) = \frac{P(B|A)\,P(A)}{P(B)} \tag{3.7}$$

$$\widetilde{R}_{ji} = \frac{R_{ij}U_j}{\sum_k R_{ik}U_k} \tag{3.8}$$

With A representing the physical truth and B the measurement in the detector. $P(B|A)$ is the conditional probability to observe measurement B under the condition of a true distribution A, and it is equal to the matrix elements R_{ij} of the detector response matrix $\mathbf{R}$. Respectively, $P(A|B)$ is the conditional probability of a true distribution A under the condition of a measured distribution B, which is the inverse matrix which is needed to calculate the physical truth from a measurement. It corresponds to the matrix elements $\widetilde{R}_{ji}$ of the smearing matrix $\widetilde{R}$. $P(B)$ is analogous to the vector elements of the measured spectrum M and calculated with the response matrix: $M_i = \sum_k R_{ik}U_k$. U_j are the vector elements of the unfolded true distribution $P(A)$. The equations have two remaining unknowns: $P(A)$ respectively U_j and $P(A|B)$ respectively the smearing matrix elements $\widetilde{R}_{ji}$. To overcome this problem, an iterative process is used:

$$U' = \widetilde{\mathbf{R}}[U] \cdot M \tag{3.9}$$

If the spectrum U is the true distribution "T" the unfolded spectrum U' is also T. Otherwise the solution for U' is in between U and T. As an iterative process U is replaced with U' to calculate the next solution U''. After 10 iteration steps a convergence is reached to obtain the true unfolded distribution.

3.7 Systematic uncertainties

The precision of a measured observable is not only determined by statistics but is also subject to systematic uncertainties which arise from the detector system, the analysis techniques and the proper description of those in the Monte Carlo simulation. The systematic uncertainties are studied for the selection of electron candidates, the hadron contamination removal, the detector alignment and the analysis method. The uncertainties on the selection of electron candidates are studied by variation of the track selection criteria and electron identification criteria. The complete analysis to calculate the yield of electrons from heavy-flavor hadron decays was repeated for each selection criterion variation. To identify deviations of the yield which are not the result of statistical fluctuations due to changed selection criteria, a method proposed by R. Barlow [108] was adopted. The difference Δ between the fully corrected yields obtained with the reference selection criteria and the modified selection criteria, respectively, is calculated for each p_{T} bin as shown in Equation 3.10. It is evaluated relative to the combined statistical uncertainty σ_{Δ} as shown in Equation 3.11. Here, a full correlation between both yields is assumed, which is justified because in each variation only one selection criterion is changed, and, thus, one of the two electron samples is always a true subset of the other one.

$$\Delta(p_{\mathrm{T}}) = \frac{1}{2\pi p_{\mathrm{T}}} \frac{d^2 N_{ref}(p_{\mathrm{T}})}{dp_{\mathrm{T}}\, dy} - \frac{1}{2\pi p_{\mathrm{T}}} \frac{d^2 N_{\mathrm{var}}(p_{\mathrm{T}})}{dp_{\mathrm{T}}\, dy} \tag{3.10}$$

$$\sigma_{\Delta}(p_{\mathrm{T}}) = \sqrt{\left|\sigma^2_{\mathrm{ref}}(p_{\mathrm{T}}) - \sigma^2_{\mathrm{var}}(p_{\mathrm{T}})\right|} \tag{3.11}$$

Variation of selection criteria

For each selection criterion only deviations from the reference are considered in which the normalized difference $\frac{\Delta}{\sigma_{\Delta}}(p_{\mathrm{T}})$ is bigger than 2σ over a broad p_{T} range to exclude single-bin fluctuations. The assigned uncertainties are then calculated as a relative uncertainty by dividing the yields from the varied selection criteria by the yield of the reference criterion. A summary of the variations of the selection criteria is shown in Table 3.3 for the electron candidates and in Table 3.4 for the associated candidates. The assigned uncertainties are summarized in Table 3.5.

Table 3.3: Table of the variations of the selection criteria of electron candidates.

Observable	Reference cut	TPC-TOF	TPC-only
DCA xy and z (cm)	(10,20)	(5,10),(20,50)	(5,10),(20,50)
ITS layer	4	3, 5, 6	3, 5, 6
SPD	kBoth ITS layer 4	kAny ITS layer 3, 4, 5, 6	kAny ITS layer 3, 4, 5, 6
	kBoth ITS layer 4	kFirst ITS layer 4, 5	kFirst ITS layer 4, 5
TPC cluster	110	90, 95, 105, 110, 115, 120	90, 95, 105, 110, 115, 120
TPC PID cluster	80	60, 70, 90, 100	60, 70, 90, 100
TOF PID	$3\sigma_{\mathrm{e-TOF}}$	no, 1.5, 2, 2.5, $4\sigma_{\mathrm{e-TOF}}$	n/a
TPC PID lower cut	$-0.5\sigma_{\mathrm{e-TPC}}$ (69%) (TPC-TOF) $0\sigma_{\mathrm{e-TPC}}$ (50%) (TPC-only)	$0.09\sigma_{\mathrm{e-TPC}}$ (50%) $-0.17\sigma_{\mathrm{e-TPC}}$ (60%) $-0.94\sigma_{\mathrm{e-TPC}}$ (84%)	$-0.17\sigma_{\mathrm{e-TPC}}$ (60%) $-0.425\sigma_{\mathrm{e-TPC}}$ (69%) $-0.94\sigma_{\mathrm{e-TPC}}$ (84%)
TPC PID upper cut	$3\sigma_{\mathrm{e-TPC}}$ (69%)	$2.15\sigma_{\mathrm{e-TPC}}$ (66.9%) $2.67\sigma_{\mathrm{e-TPC}}$ (68.5%) $4.21\sigma_{\mathrm{e-TPC}}$ (69.1%)	not checked (no difference to TPC-TOF)
η	-0.6 to 0.6	-0.6 to 0, 0 to 0.6, -0.4 to 0, 0 to 0.4, -0.5 to -0.1, 0.1 to 0.5	-0.6 to 0, 0 to 0.6, -0.4 to 0, 0 to 0.4, -0.5 to -0.1, 0.1 to 0.5

Table 3.4: Table of the variations of the selection criteria for the associated track candidates for the photonic background evaluation.

Observable	Reference cut	TPC-TOF	TPC-only
DCA xy and z	(10,20)	(5,10),(20,50)	(5,10),(20,50)
ITS layer	2	3, 4, 5	3, 4, 5
TPC (cls, PID cls)	(80,60)	(80,70), (100,60), (100,80)	(80,70), (100,60), (100,80)
TOF PID	not TOF PID	$3\sigma_{\mathrm{e-TOF}}$	$3\sigma_{\mathrm{e-TOF}}$
TPC PID	$\pm 3\sigma_{\mathrm{e-TPC}}$	2, $4\sigma_{\mathrm{e-TPC}}$	2, $4\sigma_{\mathrm{e-TPC}}$
Mass cut	0.14	0.01, 0.05, 0.1, 0.13, 0.15, 0.18, 0.2	0.01, 0.05, 0.1, 0.13, 0.15, 0.18, 0.2
Minimum p_{T}	0	0.1, 0.2, 0.3, 0.5, 0.7, 0.9	0.1, 0.2, 0.3, 0.5, 0.7, 0.9
Re-weighting	yes	no, reweighting of η Dalitz component * 0.8 and 1.2	no, reweighting of η Dalitz component * 0.8 and 1.2

Example for the variation procedure

An example for the procedure can be found in Figure 3.11. In the left panel the results for the yields of electrons from heavy-flavor hadron decays are shown for different selection criteria of the number of ITS clusters for the associated electron candidate, according to Table 3.4. In the middle panel the $\frac{\Delta}{\sigma_\Delta}(p_\mathrm{T})$ is calculated according to Equation 3.10 and 3.11. Deviations larger than 3σ are visible, which means that the deviations for the yields with different selection criteria are not of statistical nature. In the right panel the ratios of the yields with the changed selection criteria are divided by the yield with the default selection criterion. Due to the large asymmetry of the deviation, a systematic uncertainty of 4% is assigned to the transverse-momentum range $0.5 < p_\mathrm{T} < 1\,\mathrm{GeV}/c$, while for $1 < p_\mathrm{T} < 2.5\,\mathrm{GeV}/c$ a systematic uncertainty of 1% is assigned.

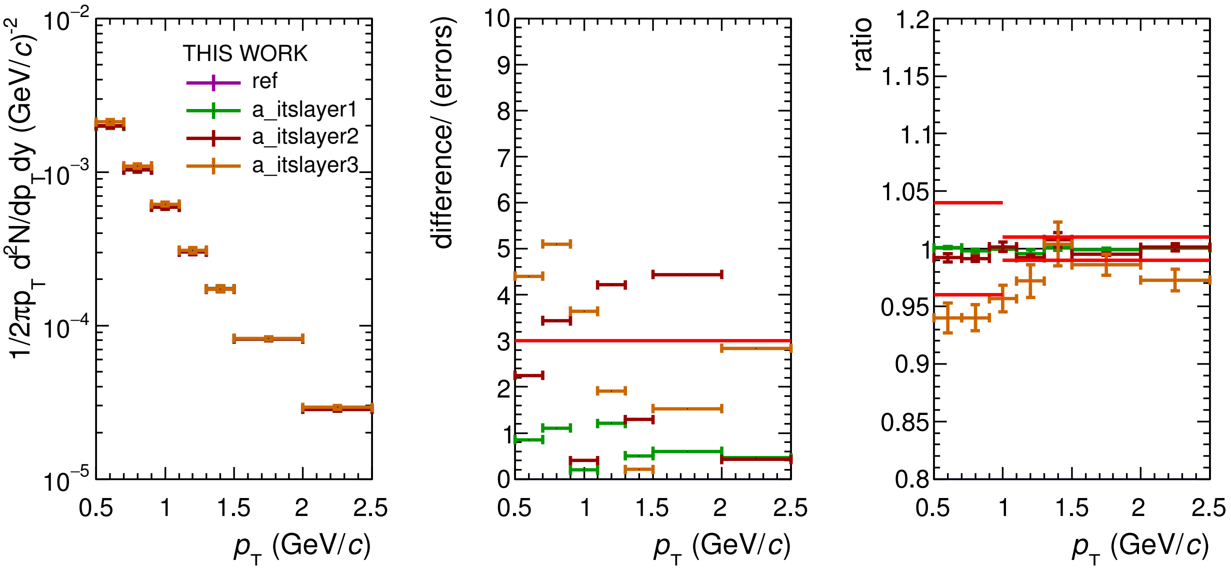

Figure 3.11: Left panel: corrected yields of electrons from heavy-flavor hadron decays for different selection criteria for the number of ITS cluster for the associated electron candidate. Middle panel: Difference between yields with changed selection criterion and default selection criterion divided by the reduced uncertainty according to Equation 3.10 and 3.11. Right panel: Ratio of the yields with changed selection criteria to the yield with default selection criterion. Red lines indicate the assigned systematic uncertainties.

Hadron contamination function

The systematic uncertainty due to the subtraction of the hadron contamination was studied by variation of the parametrization which describes the hadron contamination as function of momentum p. As shown in Figure 3.12 the hadron contamination function was varied in two ways: The obtained values for the contamination as described in Section 3.4.1 were shifted to the lower or upper extreme of their statistical uncertainty and a new fit was used as a parametrization. In addition, instead of an error function a polynomial function of third degree was used to fit the hadron contamination as function of momentum for $p < 10\,\mathrm{GeV}/c$ and a constant value $c = 0.95$ was used above. The parametrizations used for the estimation of the systematic uncertainties are shown in Figure 3.12. A total uncertainty of 2% on the yield of

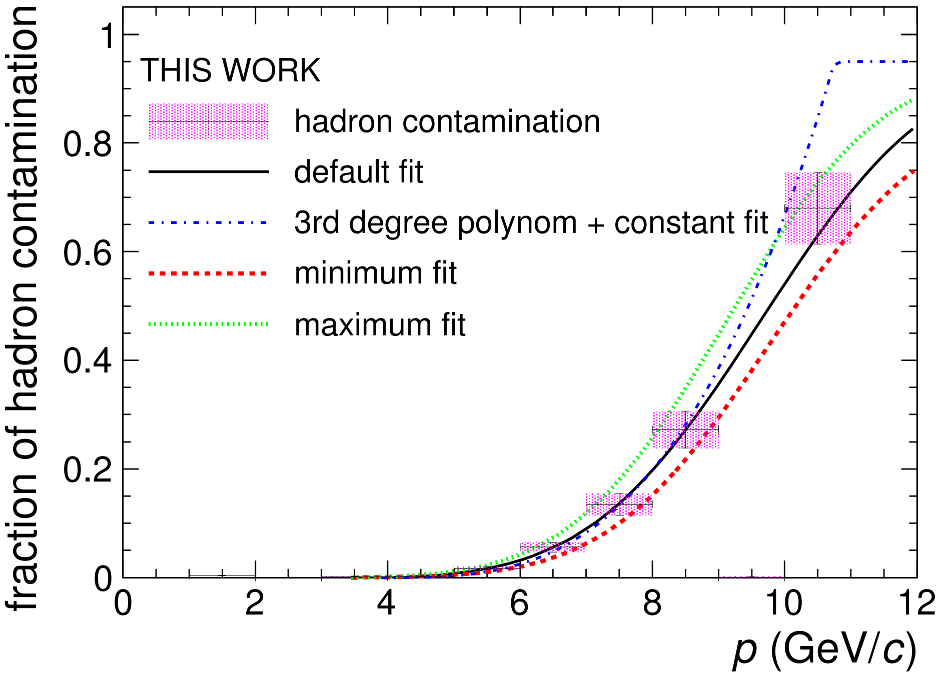

Figure 3.12: Different parametrizations for the hadron contamination function to evaluate a systematic uncertainty on the hadron contamination removal. The dashed (red) and dotted (green) lines represent new parametrizations fitted to the values for the hadron contamination (magenta area) shifted up and down by the statistical uncertainties respectively. The dotted-dashed (blue) line represents a third degree polynomial plus a constant $c = 0.95$ as parametrizations for the hadron contamination.

electrons from heavy-flavor hadron decays for the momentum range $2.5 < p_{\mathrm{T}} < 8\,\mathrm{GeV}/c$ has been estimated.

Subdetector matching

The matching of track between different parts of the detector is subject to systematic deviations due to uncertainties of the alignment of the different detectors. The uncertainty for the matching of tracks between ITS and TPC was analyzed in detail in [33] and quantified to a constant 3% over the whole p_{T} range. The systematic uncertainty on the matching between TPC and TOF was obtained from the analysis of the multiplicity dependence of identified charged particles [75] and amounts to 3%. The uncertainties on the TOF PID of 2% were also obtained from the same publication.

MC closure test

Besides variations of the selection criteria for the associated track in the invariant mass approach, the analysis algorithm/method of extracting the yield of electrons from heavy-flavor hadron decays was checked by using a MC simulation as input to the analysis. The MC sample describe in Section 3.1 was split up in two sub-samples to avoid auto-correlation. One half was treated in the software as real data, while the other half was used for the MC corrections.

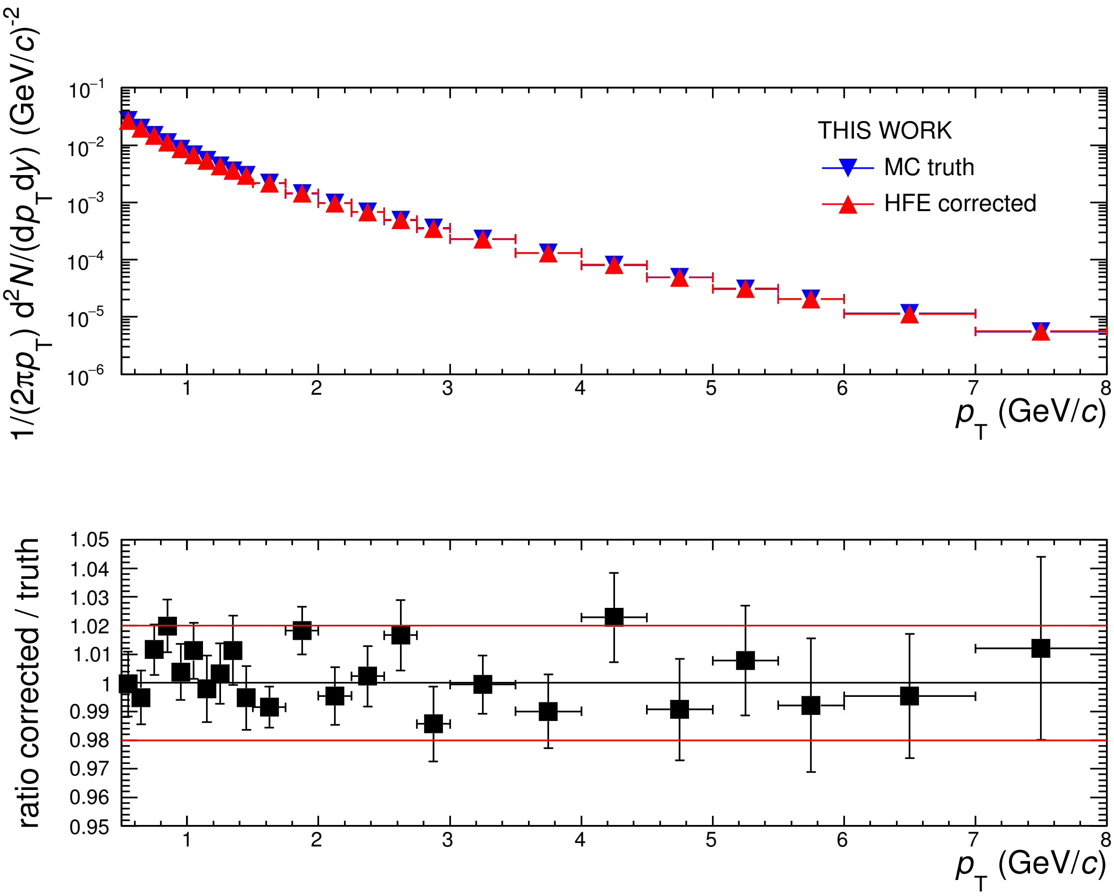

Figure 3.13: The upper panel compares the yield of electrons from heavy-flavor hadron decays from MC (MC truth) with the yield obtained by the analysis software using the same MC as "data" sample. The ratio in the lower panel shows a good agreement between the resulting yields. The red lines indicate the assigned systematic uncertainty of 2%.

The resulting yield was compared to the true yield of electrons from heavy-flavor hadron decays contained in the half MC sample treated as data. Figure 3.13 shows the very good agreement between the reconstructed and the true yield. The maximum variation of 2% of the ratio between both yields is taken as a systematic uncertainty of the method.

Summary of systematic uncertainties

The systematic uncertainties are summarized in Table 3.5. The correlation between the uncertainties is assumed to be small and, thus, they are treated as uncorrelated and added quadratically. The contributions to the total uncertainty do not have one dominant source but are due to many medium sized (2%–3%) uncertainties. The total systematic uncertainty on the p_T-differential yield of electrons from heavy-flavor hadron decays is 9.9% in $0.5 < p_T < 1$ GeV/c, 8% in $1 < p_T < 2.5$ GeV/c and 6% in $2.5 < p_T < 8$ GeV/c. The decrease of the systematic uncertainties with increasing p_T can be explained by the increase of the signal over background ratio, yielding to less influence of the uncertainties on the determination of the electron background.

Table 3.5: Summary of systematic uncertainties for the two different PID strategies.

	TPC-TOF	TPC-only
Variable / inclusive e	$0.5 < p_T < 2.5\,\mathrm{GeV}/c$	$2.5 < p_T < 8\,\mathrm{GeV}/c$
DCA xy and z	negligible	negligible
TPC cluster	2%	negligible
TPC cluster PID	2.5%	negligible
ITS layer	2%	1%
SPD requirement	2%	2%
ITS-TPC matching [33]	3%	3%
TPC PID	3%	3%
TPC-TOF matching[75]	3%	n/a
TOF PID[75]	2%	n/a
η range	negligible	negligible
Hadron contamination	negligible	2%
Variable / associated e		
DCA xy and z	1% (0.5–1 GeV/c) 0% (1–2.5 GeV/c)	negligible
TPC clusters tracking	negligible	negligible
TPC clusters PID	negligible	negligible
ITS number of hits	4% (0.5–1 GeV/c) 1% (1–2.5 GeV/c)	1%
TPC PID	3% (0.5–1 GeV/c) 1% (1–2.5 GeV/c)	negligible
ITS PID	negligible	negligible
Mass cut	2% (0.5–1 GeV/c) 0% (1–2.5 GeV/c)	negligible
Minimum p_T	negligible	1%
Re-weighting	2%	negligible
MC closure test	2%	2%
Unfolding	1%	1%
SUM	9.9% (0.5–1 GeV/c) 8.0% (1–2.5 GeV/c)	6%

3.8 Proton-proton reference

To calculate the nuclear modification factor R_{pPb} (see Section 1.4) a reference from pp collisions at the same beam energy $\sqrt{s_{\mathrm{NN}}} = 5.02\,\mathrm{TeV}$ is needed. No measurement of electrons from heavy-flavor hadron decays from pp collisions at $\sqrt{s} = 5.02\,\mathrm{TeV}$ is available. ALICE has measured electrons from heavy-flavor hadron decays in pp collisions at $\sqrt{s} = 2.76\,\mathrm{TeV}$ [98] and $\sqrt{s} = 7\,\mathrm{TeV}$ [96] and the ATLAS experiment has measured electron cross sections in pp collision at $\sqrt{s} = 7\,\mathrm{TeV}$ [109]. The results of the present work were published together with another measurement extending the p_{T} coverage to $6 < p_{\mathrm{T}} < 12\,\mathrm{GeV}/c$, exploiting the electron identification capabilities of the ALICE EMCal [69]. Therefore a reference up to $p_{\mathrm{T}} = 12\,\mathrm{GeV}/c$ is needed, which requires to combine the cross sections at $\sqrt{s} = 7\,\mathrm{TeV}$ from ALICE and ATLAS. The cross section in the one common momentum bin $7 < p_{\mathrm{T}} < 8\,\mathrm{GeV}/c$ was calculated as a weighted average of both results. The inverse squared uncertainties were used as weights according to [7].

The measurement of the cross section of electrons from heavy-flavor hadron decays in pp collisions with ALICE at $\sqrt{s} = 7\,\mathrm{TeV}$ was done in the rapidity range $|y| < 0.5$, the cross section measurement with ALICE at $\sqrt{s} = 2.76\,\mathrm{TeV}$ was done in the rapidity range $|y| < 0.8$. The measurement of electron cross sections with ATLAS was done in the pseudo-rapidity range $|\eta| < 2.0$, excluding $1.37 < |\eta| < 1.52$. Recent results by ALICE for D-meson cross section in pp and p-Pb collisions [62] observe no variations as function of the rapidity (in $|\eta| < 0.8$), in agreement with theory predictions by FONLL [48]. Thus, no effect on the interpolation due to the different pseudo-rapidity ranges of the measurements is expected. The interpolated cross section will be compared to the measurement in p-Pb collisions at $\sqrt{s_{\mathrm{NN}}} = 5.02\,\mathrm{TeV}$ in the asymmetric rapidity range $-1.065 < y_{\mathrm{cms}} < 0.135$ assuming no effect due to the shift of the average rapidity by $\Delta y = -0.465$ in the p-Pb system.

The combined cross section from ALICE and ATLAS at $\sqrt{s} = 7\,\mathrm{TeV}$ and the cross section from ALICE at $\sqrt{s} = 2.76\,\mathrm{TeV}$ were interpolated to $\sqrt{s} = 5.02\,\mathrm{TeV}$ using a power law function to describe the cross section as function of $\sqrt{s}$:

$$\sigma_{\mathrm{e}}[p_{\mathrm{T}}] = p_1[p_{\mathrm{T}}]\left(\sqrt{s}\right)^{p_2[p_{\mathrm{T}}]}, \tag{3.12}$$

where σ_{e} is the cross section at a given p_{T} and p_1, p_2 free parameters. Equation 3.12 is solved analytically for each p_{T} interval, since two cross sections are available for two parameters of the equation. The power-law assumption is in general agreement with different theoretical models based on pQCD for the $\sqrt{s}$ dependence of the cross section [110]. To study the dependence of the interpolation on the choice of the parametrization, alternatively the interpolation was calculated using a linear or an exponential function. From this an uncertainty of $+5\%/-10\%$ without a significant p_{T} dependence was evaluated. The uncertainties from the measurements at $\sqrt{s} = 2.76\,\mathrm{TeV}$ and $\sqrt{s} = 7\,\mathrm{TeV}$ were split into the uncertainties which are correlated and uncorrelated in $\sqrt{s}$. Most uncertainties were assumed correlated due to similar experiment conditions. The uncertainty on the ITS was treated as uncorrelated between both measurements due to a known change in the detector condition. The uncertainties from the unfolding procedure and from the background cocktail are independent between both measurements and also treated as uncorrelated uncertainties. Correlated uncertainties were added linearly, while uncorrelated uncertainties were added quadratically in the interpolation procedure. The resulting correlated and uncorrelated contributions to the interpolated cross section were added in quadrature. The resulting total uncertainty was also combined quadratically with the $+5\%/-10\%$ uncertainty due to the interpolation procedure. Each of the measurements in pp collision has a p_{T} independent systematic uncertainty related to the minimum-bias collision cross section. The uncertainties of the cross section for the ALICE measurement in pp collisions at $\sqrt{s} = 2.76\,\mathrm{TeV}$ (1.9%) and for ALICE and ATLAS in pp collisions at $\sqrt{s} = 7\,\mathrm{TeV}$ (3.5% resp. 3.4%) were interpolated to the energy of $\sqrt{s} = 5.02\,\mathrm{TeV}$ resulting in 2.3%.

Figure 3.14 shows the reference spectra at $\sqrt{s} = 2.76\,\mathrm{TeV}$ and $\sqrt{s} = 7\,\mathrm{TeV}$ and the interpolated spectrum at $\sqrt{s} = 5.02\,\mathrm{TeV}$.

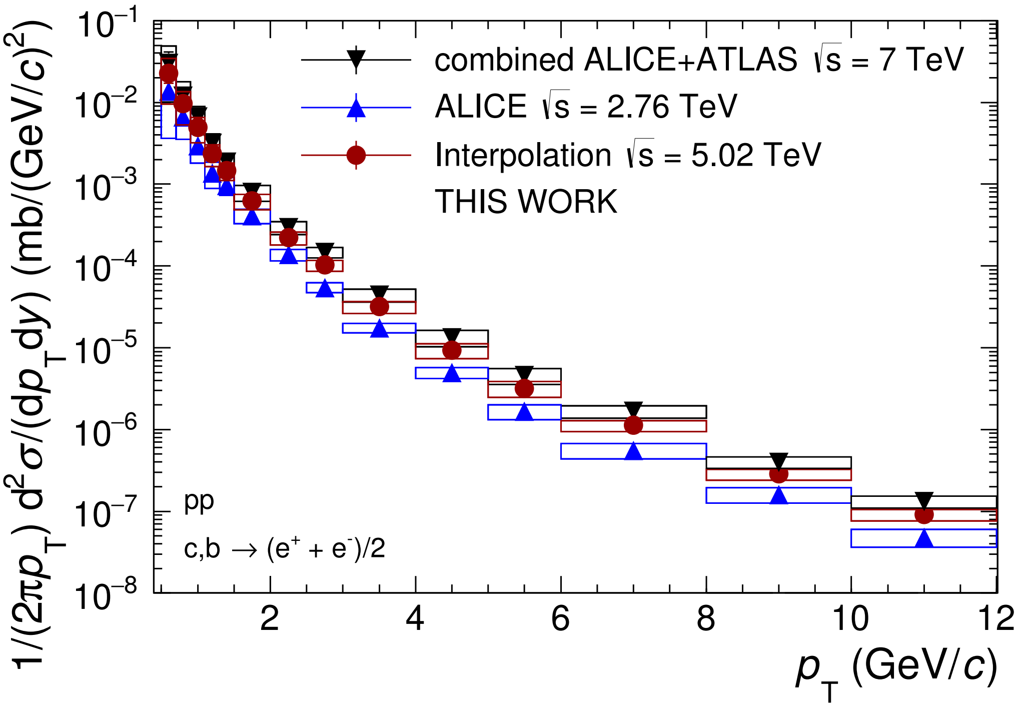

Figure 3.14: Interpolation of the cross sections of electrons from heavy-flavor hadron decays in pp collisions at $\sqrt{s} = 2.76\,\mathrm{TeV}$ [98] and $\sqrt{s} = 7\,\mathrm{TeV}$ [96, 109] to the collision energy $\sqrt{s} = 5.02\,\mathrm{TeV}$.

3.9 Results

The transverse-momentum differential cross section of electrons $\left(\frac{e^{+}+e^{-}}{2}\right)$ from heavy-flavor hadron decays is calculated as:

$$\frac{1}{2\pi p_{\mathrm{T}}}\frac{\mathrm{d}^{2}\sigma}{\mathrm{d}p_{\mathrm{T}}\mathrm{d}y}=\frac{1}{2}\frac{1}{2\pi p_{\mathrm{T}}^{\mathrm{centre}}}\frac{1}{\Delta y\Delta p_{\mathrm{T}}}\frac{N\cdot\sigma_{\mathrm{MB}}^{\mathrm{V0}}}{N_{\mathrm{MB}}},\tag{3.13}$$

where $p_{\mathrm{T}}^{\mathrm{centre}}$ are the centers of the p_{T} bins with width Δp_{T} and Δy denotes the rapidity to which the analysis is restricted. $N_{\mathrm{hfe}}/N_{\mathrm{MB}}$ is the electron yield normalized by the number of events (N_{MB}) obtained by the unfolding procedure with the approximation for the inverse detector response matrix $\widetilde{\mathbf{R}}$, which includes ϵ^{geo}, ϵ^{reco} and ϵ^{eID} (see Section 3.6). The minimum bias cross section $\sigma_{\mathrm{MB}}^{\mathrm{V0}} = 2.09 \pm 0.07\,\mathrm{b}$ in p-Pb collisions was obtained through a van der Meer scan [111].

3.9.1 Cross sections

The p_{T}-differential cross section of electrons from heavy-flavor hadron decays in p-Pb collisions at $\sqrt{s_{\mathrm{NN}}} = 5.02\,\mathrm{TeV}$ is measured in the transverse momentum range $0.5 < p_{\mathrm{T}} < 8\,\mathrm{GeV}/c$ and in the rapidity range $-1.065 < y_{\mathrm{cms}} < 0.135$. Two different electron identification strategies are used according to the electron transverse momentum: TPC and TOF ($0.5 < p_{\mathrm{T}} < 2.5\,\mathrm{GeV}/c$) and TPC only ($2.5 < p_{\mathrm{T}} < 8\,\mathrm{GeV}/c$). As a cross check for the electron identification, the cross section measurement from the TPC-TOF strategy was extended to $p_{\mathrm{T}} = 4\,\mathrm{GeV}/c$ as shown in Figure 3.15. The cross sections from both eID strategies in the range $2.5 < p_{\mathrm{T}} < 4\,\mathrm{GeV}/c$ agree well within their uncertainties. As explained in Section 3.7, the usage of the TOF detector adds additional uncertainty from electron identification (3%) and track matching (2%) to the measurement. Therefore, the final cross section for $p_{\mathrm{T}} > 2.5\,\mathrm{GeV}/c$ was measured only with the TPC electron identification. The normalization uncertainty related to the minimum bias cross section $\sigma_{\mathrm{MB}}^{\mathrm{V0}}$ of 3.7% is not shown in Figure 3.15.

The p_{T}-differential cross section is shown in Figure 3.16 together with the interpolated cross section for pp collisions at $\sqrt{s} = 5.02\,\mathrm{TeV}$. The results are published in [69]. The statistical uncertainties are indicated by vertical error bars, the systematic uncertainties are shown as boxes. The obvious difference of the relative size of the systematic uncertainties from both measurements, in particular at low p_{T}, is the result of different methods used for estimation of the electron background. The interpolation is based on pp measurements [96, 98, 109] which use a cocktail based subtraction (Section 3.5.1). For the measurement of the cross section in p-Pb collisions a reduction of the relative uncertainties by 70–80% in $0.5 < p_{\mathrm{T}} < 2.5\,\mathrm{GeV}/c$ is achieved with respect to the same measurement in pp collisions at $\sqrt{s} = 7\,\mathrm{TeV}$. The substantial reduction of the uncertainties is due to the method of tagging the photonic background (Section 3.5.2). Here, the uncertainties of the measured light hadron spectra are not relevant unlike for the cocktail based subtraction of the background.

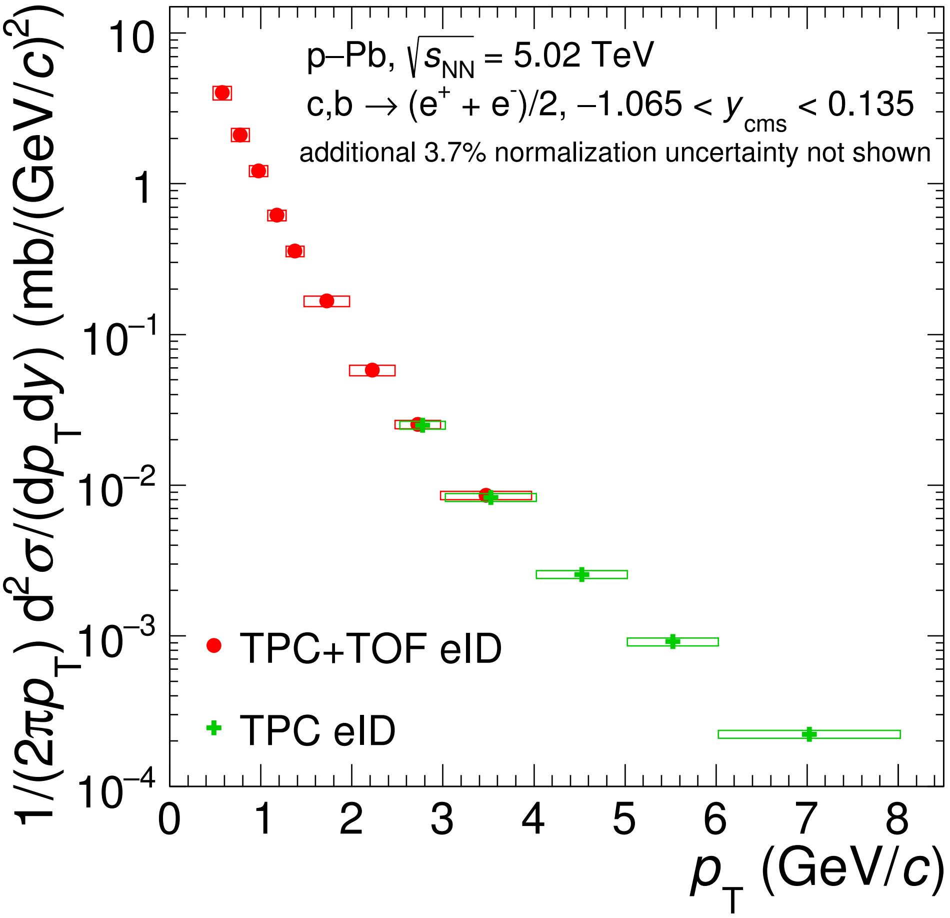

Figure 3.15: Comparison of the p_T-differential cross section for the two electron ID strategies. For low to intermediate p_T the TPC and TOF detectors were used (red), while for the intermediate to high p_T region only the TPC detector was used. Both measurements agree well with each other within their uncertainties in the overlapping p_T range. Published in [69].

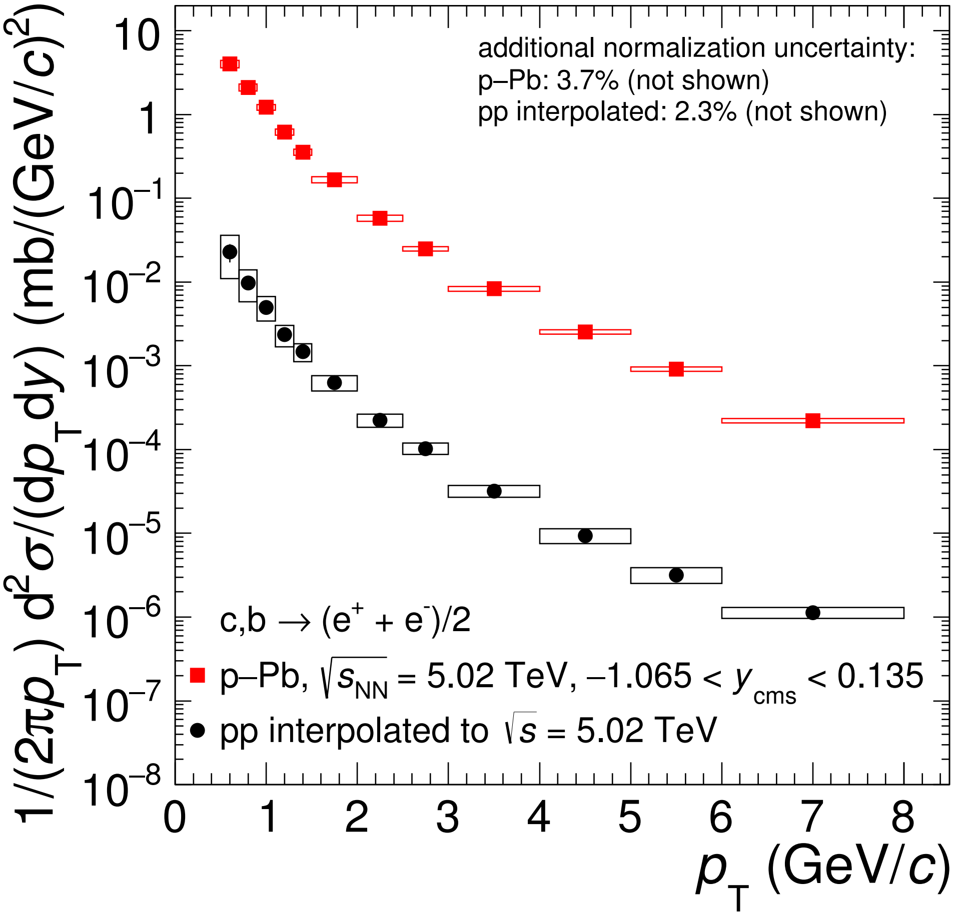

Figure 3.16: p_{T}-differential cross section of electrons from heavy-flavor hadron decays in p-Pb collisions at $\sqrt{s_{\mathrm{NN}}} = 5.02\,\mathrm{TeV}$ (red) together with the interpolated cross section for pp collisions at $\sqrt{s} = 5.02\,\mathrm{TeV}$ (black). The statistical uncertainties are indicated by vertical error bars, the systematic uncertainties are shown as boxes. Published in [69].

3.9.2 Nuclear modification factor

To study initial state effects the nuclear modification factor R_{pPb} is calculated as the ratio of the p-Pb cross section and the pp cross section scaled by the nucleon number $A = 208$ of the Pb nucleus:

$$R_{\mathrm{pPb}} = \frac{\mathrm{d}\sigma_{\mathrm{pPb}}}{\mathrm{d}p_{\mathrm{T}}} \bigg/ A\frac{\mathrm{d}\sigma_{\mathrm{pp}}}{\mathrm{d}p_{\mathrm{T}}} \tag{3.14}$$

This nuclear modification factor R_{pPb} is shown in Figure 3.17. The normalization uncertainty of 4.4% is shown as black bar, resulting from the normalization uncertainty from the measurement in p-Pb collisions at $\sqrt{s_{\mathrm{NN}}} = 5.02\,\mathrm{TeV}$ (3.7%) and the interpolated normalization uncertainty (2.3%) by adding in quadrature. The major contribution to the systematic uncertainties on the R_{pPb} is due to the large uncertainties of the interpolated pp reference which is mainly driven by the cocktail background subtraction technique. The result is compatible with unity in the measured transverse momentum range $0.5 < p_{\mathrm{T}} < 8\,\mathrm{GeV}/c$ within statistical and systematical uncertainties. It can be concluded that cold nuclear matter effects do not play a role in the suppression of the yield of electrons from heavy-flavor hadron decays observed at high p_{T} in Pb–Pb collisions at $\sqrt{s_{\mathrm{NN}}} = 2.76\,\mathrm{TeV}$ [112]. An enhancement of the p_{T}-differential cross section of electrons in p-Pb collisions cannot be excluded as also seen in d–Au collisions at $\sqrt{s_{\mathrm{NN}}} = 200$ GeV [97], which can be explained by the so-called Cronin effect due to broadening of the parton transverse momentum. In Figure 3.18 the measurement of R_{pPb} is compared to different theoretical model calculations. Theoretical predictions using perturbative QCD, which include cold nuclear matter effects, agree with the measurement and show negligible deviations from unity. The model prediction shown in gray ("FONLL+EPS09NLO") is calculated by combining predictions for heavy-flavor cross sections from FONLL [46, 48] with parametrizations for shadowing of the nuclear parton distribution function "EPS09NLO" [34]. Calculations by Sharma *et. al.* [38] use nuclear shadowing effects as well as k_{T}-broadening and nuclear energy loss. The model predicts a small suppression for low transverse momentum. The calculations were initially done for forward rapidity measurements and extrapolated to mid-rapidity [115]. A different approach is used by Kang *et. al.* [39] which predicts an enhancement at low transverse momentum through broadening of the parton p_{T} by incoherent multiple parton scattering processes before the hard scattering process. The fluctuations lead to a larger $\langle p_{\mathrm{T}}\rangle^2$. The model was calculated for backward rapidity and extrapolated to the rapidity region of this work [115]. Blast-wave model calculations predict a transverse momentum redistribution of the p_{T}-differential electron production cross section by assuming hydrodynamical expansion of a produced medium in p-Pb collisions. This would lead to a modification of the p_{T}-differential charm and beauty spectra by radial and elliptic flow (see Sections 1.5 and 1.4). The parameters for the blast-wave model [113] were obtained from the measurement of identified charged particles in p-Pb collisions at $\sqrt{s_{\mathrm{NN}}} = 5.02\,\mathrm{TeV}$ [75]. From the model p_{T}-differential spectra for D and B mesons were calculated. The spectra were used as input to a Monte Carlo decayer forcing the semi-leptonic decay to electrons. The resulting spectra of electron from D and B meson decays were compared to FONLL predictions [48] for electrons from D and B meson hadron decays at $\sqrt{s_{\mathrm{NN}}} = 5.02\,\mathrm{TeV}$ [114]. The blast-wave calculations agree with the measured data and predict only a small enhancement at low p_{T}.

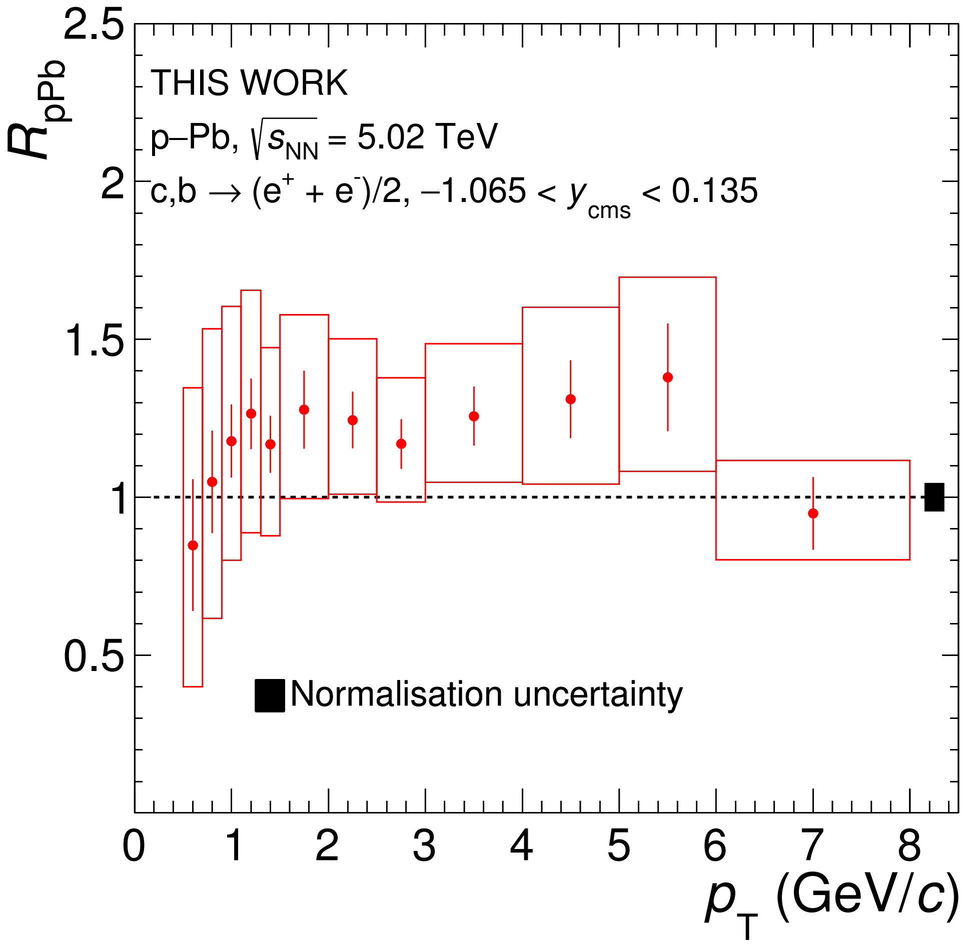

Figure 3.17: Nuclear modification factor R_{pPb} for electrons from heavy-flavor hadron decays. The black box indicates the normalization uncertainty of 4.4%.

All theoretical models predict small effects for a deviation of the cross section with respect to binary-collision scaling of electrons from heavy-flavor hadron decays in p-Pb collisions at $\sqrt{s_{\mathrm{NN}}} = 5.02\,\mathrm{TeV}$. They are in agreement with the measured data within uncertainties.

3.9.3 Discussion

The measurement of R_{pPb} has substantial systematic uncertainties which can be improved in future analyses. However, the systematic uncertainties on the measured cross section in p-Pb collisions at $\sqrt{s_{\mathrm{NN}}} = 5.02\,\mathrm{TeV}$ are already very small (6%–10%) and cannot be reduced much further (using the same analysis methods). The statistical uncertainties are also small (3% for $0.5 < p_{\mathrm{T}} < 4\,\mathrm{GeV}/c$ and 4%–7% for higher p_{T}), thus an increase of the statistics would not lead to improvements in the measurement. The main contribution to the large uncertainties of R_{pPb} is from the pp reference measurement. A first step could be to reanalyze the measurements in pp collisions at $\sqrt{s} = 2.76\,\mathrm{TeV}$ [98] and $\sqrt{s} = 7\,\mathrm{TeV}$ [96] using the tagging method to estimate the photonic electron background. The possible improvements are indicated by the gray error boxes in Figure 3.19. For this estimate, the uncertainties of the interpolated pp reference for R_{pPb} are scaled to the relative uncertainties of the p-Pb cross section for each p_{T} interval. This assumes that the cross section measurement in p-Pb collisions is of high quality and the uncertainties are

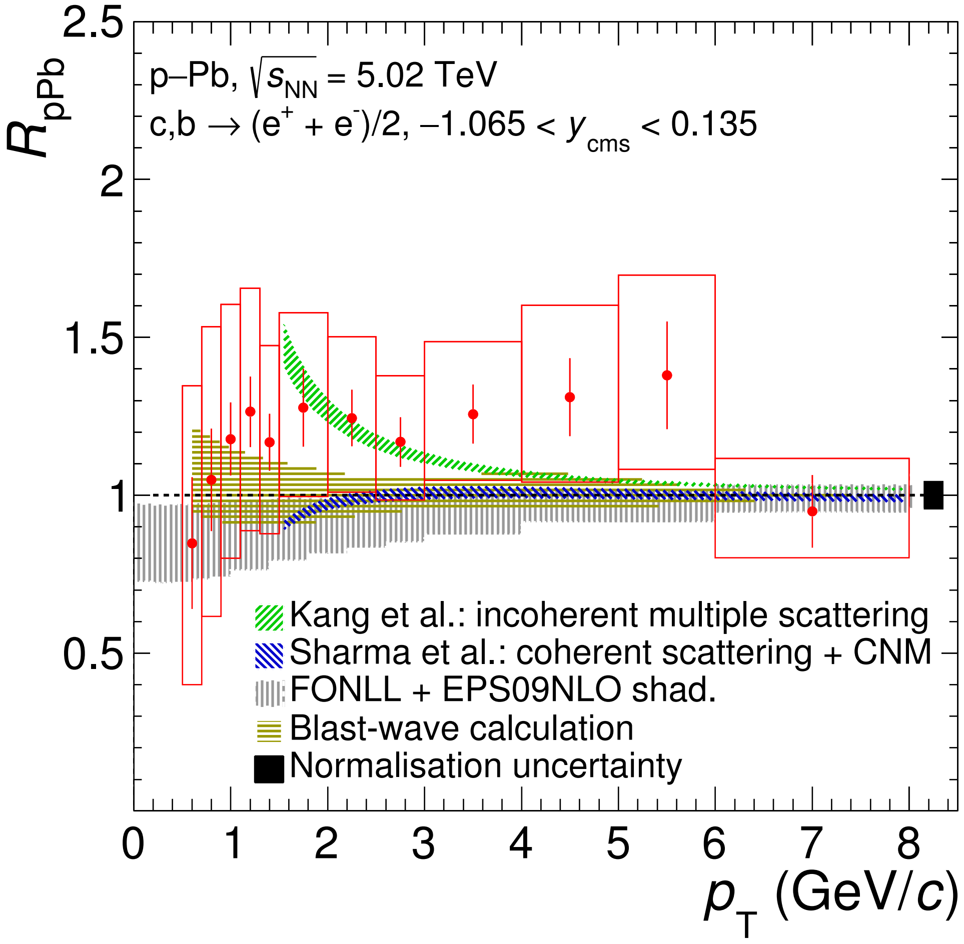

Figure 3.18: Comparison of the measured R_{pPb} with predictions from different theoretical models (FONLL+EPS09NLO[34, 46], Kang *et al.* [39], Sharma *et al.* [38], blast-wave [113, 114]). The black box indicates the normalization uncertainty of 4.4%. Published in [69].

at the lower limit for this kind of measurement. The interpolation uncertainty of $+5\%/-10\%$ is added to reflect the possible improvement with the currently available experimental data. A visible reduction of the systematic uncertainties at low p_{T} can be achieved by using the tagging method. While for intermediate transverse momentum $2.5 < p_{\mathrm{T}} < 8\,\mathrm{GeV}/c$ the improvement is only marginal because the electron background in this region is already small and thus the uncertainties are less dependent on the determination of the electron background. A measurement of electrons from heavy-flavor hadron decays in pp collisions at $\sqrt{s} = 5.02\,\mathrm{TeV}$ could be used in the future as a new reference. It would reduce the predicted systematic uncertainty by the interpolation uncertainty $(+5\%/-10\%)$. However, the current theoretical model predictions have already very small uncertainties. As stated above, a new measurement with improved statistical and systematical uncertainties, using the current analysis methods and detector setup, will not increase the precision to allow for a discrimination between most of the model calculations which are not deviating very much from each other. A discrimination to the model calculations by Kang *et. al.* [39] below $p_{\mathrm{T}} = 2.5\mathrm{GeV}/c$ could be achieved with smaller uncertainties. It can be concluded that the current theoretical models agree with the results of the measurement: The influence of cold nuclear matter effects on the heavy-flavor production in the measured

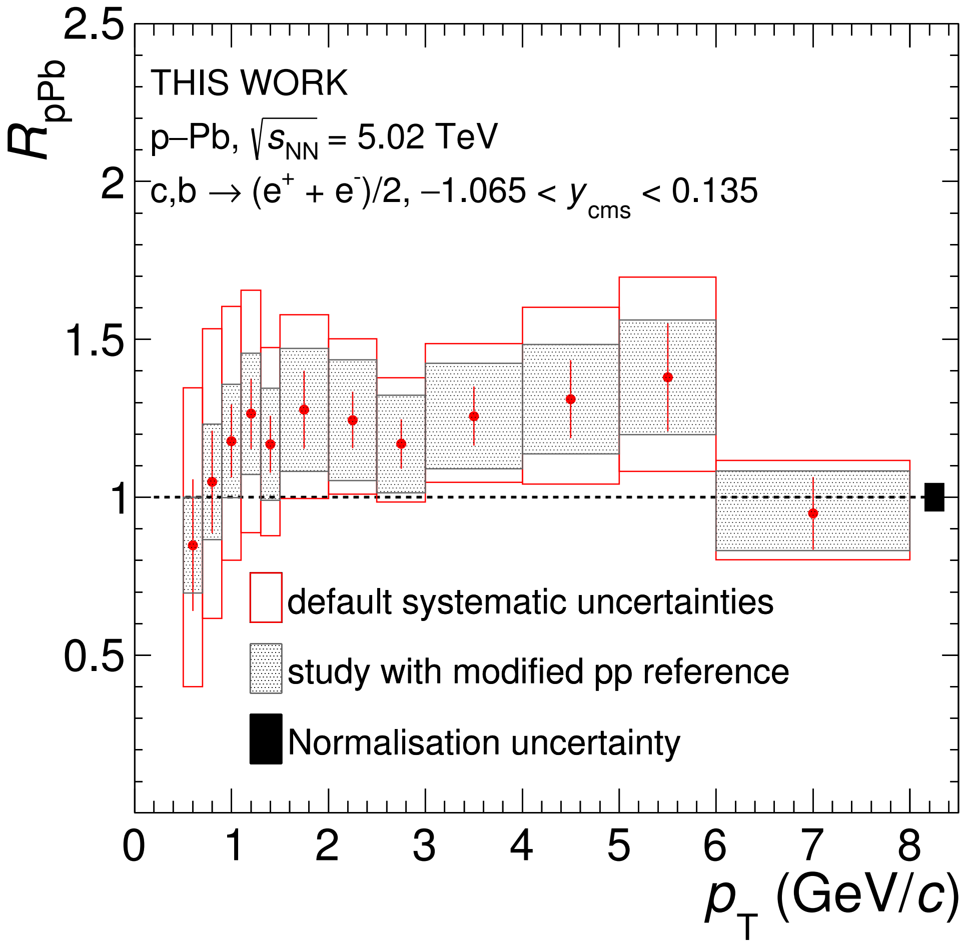

Figure 3.19: $R_{\rm pPb}$ with the current systematic uncertainties in red and with reduced uncertainties of the pp reference in gray. The black box indicates the normalization uncertainty of 4.4%.

transverse momentum range is rather small and major improvements in the measurement of electrons from heavy-flavor hadron decays in the future are questionable.

4 Dependence of the electron yield on the charged-particle multiplicity

The influence of CNM effects on the production of heavy-flavor hadrons in p-Pb was discussed in the last chapter. The minimum-bias cross section of electrons from semi-leptonic heavy-flavor hadron decays in p-Pb collisions at $\sqrt{s_{\mathrm{NN}}} = 5.02\,\mathrm{TeV}$ was compared to a reference cross section in pp collisions interpolated to $\sqrt{s} = 5.02\,\mathrm{TeV}$ and scaled by the mass number of the Pb nucleus (A= 208). The result is compatible with unity which implies that the heavy-flavor yield in p-Pb collisions is compatible with the yield in pp collisions at the same cms energy scaled by the average number of binary collision $\langle N_{\mathrm{coll}}\rangle$ in a p-Pb collision ($\langle N_{\mathrm{coll}}\rangle_{\mathrm{MB}} \approx 7$ [116]). The conclusions obtained from the p_{T}-dependent nuclear modification factor R_{pPb} are limited in their interpretation to average minimum bias collisions. A better general understanding of heavy-flavor production mechanisms can be achieved by looking into extreme cases where the respective number of binary collisions is much larger than $\langle N_{\mathrm{coll}}\rangle$.

In pp collisions heavy-flavor production was studied as function of the charged-particle multiplicity. The charged-particle multiplicity gives information about the soft (non-perturbative) regime while heavy-flavor production is related to hard processes described by pQCD. Early models including the first tunes of Pythia 6 [93] predicted a decrease of heavy-flavor production as function of the multiplicity which can be estimated by the charged particle density. The general understanding was that for an increase in soft processes the probability for hard processes becomes smaller and thus heavy-flavor production is suppressed for high multiplicity events. However, ALICE observed the opposite trend: The relative heavy-flavor production increases linearly or even faster than linearly with respect to the charged-particle multiplicity which is calculated by the relative charged particle density [117, 118]. Model calculations including Multiple-Parton Interactions (MPIs) [119] have been able to describe the linear increase for heavy-flavor production [120, 121]. They explain the enhancement of heavy-flavor yields by including multiple hard parton-parton scatterings in a proton-proton collision. The situation in p-Pb collisions is more complicated since on average seven nucleon-nucleon collisions occur. Only ALICE has measured the multiplicity dependence of heavy-flavor production in p-Pb collisions. Also only theoretical model calculations from EPOS [122] are available to describe heavy-flavor production in p-Pb collisions for events with large multiplicity where a large number of binary collisions and MPIs may both play a role. ALICE has measured D-meson production as function of charged-particle multiplicity in p-Pb collisions [76]. Results show a faster-than-linear increase for D-meson relative yields for a charged-particle multiplicity estimated at mid-rapidity. However, when the charged-particle multiplicity is estimated in the backward rapidity region, only a linear dependence is observed for the relative D-meson yields. This analysis focuses on the multiplicity dependence of heavy-flavor production in p-Pb collisions by measuring the relative yields of electrons from heavy-flavor hadron decays as a function of the multiplicity. The charged-particle multiplicity is estimated using two different approaches: At mid-rapidity using SPD tracklets and at backward rapidity using the analogue signal of the V0A detector. Since for low transverse momentum ($p_{\mathrm{T}} < 4\,\mathrm{GeV}/c$) mainly electrons from D-meson decays are measured, the relative results are checked for compatibility with the published results [76]. Due to the large fraction of electrons from beauty hadron decays at high

p_{T}[1], a different trend of the multiplicity dependence might be observed for high-p_{T} electrons from heavy-flavor decays compared to high-p_{T} D mesons.

The yields of electrons from heavy-flavor hadron decays have to be evaluated for different classes of the charged-particle multiplicity. The multiplicity classes were defined using estimators at mid-rapidity and backward rapidity, respectively. Also the charged-particle multiplicity needs to be calibrated and corrected for detector inefficiencies. This is described in Section 4.1. Afterwards, the multiplicity dependent yields of electrons from heavy-flavor hadron decays is calculated using the same analysis strategy as described in the last chapter. The subtraction of the hadron contamination, the correction of the photonic yield using the tagging efficiency $\varepsilon_{\mathrm{tag}}$ and the correction for the tracking efficiency and geometric acceptance need to be evaluated in order to check a possible multiplicity dependence. In case a multiplicity dependence is observed, corrections have to be taken into account accordingly, which is described in Section 4.2. Systematic uncertainties of the measurement of the relative yields are evaluated in Section 4.3. The results of the measurements are discussed in Section 4.4 and compared to the results on the multiplicity dependence of D-mesons in p-Pb collisions.

4.1 Multiplicity selection

In this analysis the charged-particle multiplicity is estimated in two ways for different rapidity regions. At mid-rapidity the charged-particle multiplicity is measured using SPD tracklets (see Section 2.3) restricted to a pseudo-rapidity range of $|\eta| < 1$. The number of tracklets is proportional to the number of charged particles on an event average. A Monte Carlo simulation is used to determine the proportionality factor between the measured number of tracklets and the charged particle density $\mathrm{d}N_{\mathrm{ch}}/\mathrm{d}\eta$. At backward rapidity ($2.8 < \eta < 5.1$) the charged-particle multiplicity is estimated with the signal in the V0A detector.

The multiplicity estimators have a known bias. The average number of SPD tracklets and the average V0A signal depend on the z position of the event vertex due the change in the geometric acceptance. In addition, temporary and permanent failures in parts of the detector lead to an inhomogeneous acceptance. Before the estimators can be used to calculate the charged-particle multiplicity these biases need to be corrected. In the following the correction procedures for both multiplicity estimators are described.

4.1.1 SPD tracklet multiplicity

The distribution of the raw number of SPD tracklets (N_{tr}) is shown in Figure 4.1 for the two data samples `LHC13b` and `LHC13c` which are described in Section 3.1.

The acceptance of the SPD is inhomogeneous and depends on the z position of the reconstructed primary vertex ($\mathrm{z}_{\mathrm{vtx}}$). The asymmetry of the distribution of N_{tr} as function of $\mathrm{z}_{\mathrm{vtx}}$ is shown in Figure 4.2a for the data samples `LHC13b` in panel (i) and `LHC13c` in panel (ii) respectively. The performance of the SPD is not constant over time which is shown in the profile of both data sample distributions in panel (iii) of Figure 4.2a. The ratio of both profiles is shown in Figure 4.2a (iv) which demonstrates a considerable difference between the data samples. Thus, the data samples `LHC13b` and `LHC13c` need to be corrected separately. The profiles in Figure 4.2a

---

[1] More than 50% of electrons with $p_{\mathrm{T}} > 4\,\mathrm{GeV}/c$ come from beauty-hadron decays in pp collisions at $\sqrt{s} = 7\,\mathrm{TeV}$ [64]

(iii) are used as an input to renormalize N_{tr} for `LHC13b` and `LHC13c` separately on an event-by-event base from $\langle N_{\mathrm{tr}}\rangle_{\mathtt{LHC13b}} = 28.55$ and $\langle N_{\mathrm{tr}}\rangle_{\mathtt{LHC13c}} = 28.13$ to a fixed global scale $N_{\mathrm{tr}}^{\mathrm{glob}}$. The best choice for the global renormalization scale was studied in [76], where it was concluded that fluctuations could be minimized by renormalizing to the minimum of the profile. Thus, for this analysis $N_{\mathrm{tr}}^{\mathrm{glob}} = 19.44$ was used, which is the minimum of the profile of LHC13c.

The $\mathrm{z_{vtx}}$ dependent number of tracklets $N_{\mathrm{tr}}(\mathrm{z_{vtx}})$ is corrected by an offset $\Delta N(\mathrm{z_{vtx}})$ which is smeared by a Poissonian distribution with the mean $\lambda = \Delta N$:

$$N_{\mathrm{tr}}^{\mathrm{corr}}(\mathrm{z_{vtx}}) = N_{\mathrm{tr}}(\mathrm{z_{vtx}}) - \mathrm{P}[\lambda = \Delta N(\mathrm{z_{vtx}})] \tag{4.1}$$

with $\Delta N(\mathrm{z_{vtx}})$ being a $\mathrm{z_{vtx}}$ dependent correction factor calculated with the average $\langle N_{\mathrm{tr}}\rangle(\mathrm{z_{vtx}})$ and the global scale $N_{\mathrm{tr}}^{\mathrm{glob}}$:

$$\Delta N = N_{\mathrm{tr}}(\mathrm{z_{vtx}}) \cdot \left(\frac{N_{\mathrm{tr}}^{\mathrm{glob}}}{\langle N_{\mathrm{tr}}\rangle(\mathrm{z_{vtx}})} - 1\right) \tag{4.2}$$

The corrected distributions are shown in Figure 4.2b panel (i) and (ii). The average for the corrected distributions $\langle N_{\mathrm{tr}}^{\mathrm{corr}}\rangle$ is essentially flat at the fixed global scale $N_{\mathrm{tr}}^{\mathrm{glob}}$ as shown in panel (iii) of Figure 4.2b. A residual shape is still seen, resulting in fluctuations $< 2\%$ from the smearing procedure, which will be added as a systematic uncertainty on the relative charged-particle multiplicity. However, the difference between both running periods was removed by the correction which is demonstrated in the ratio between both profiles in panel (iv) of Figure 4.2b.

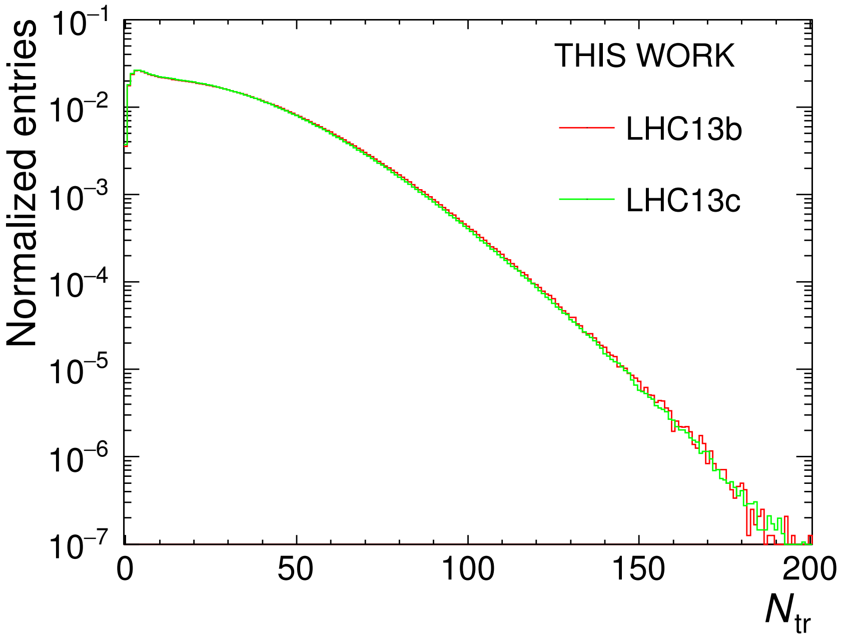

Figure 4.1: Frequency distribution of raw tracklet multiplicity N_{tr} for the periods `LHC13b` and `LHC13c`.

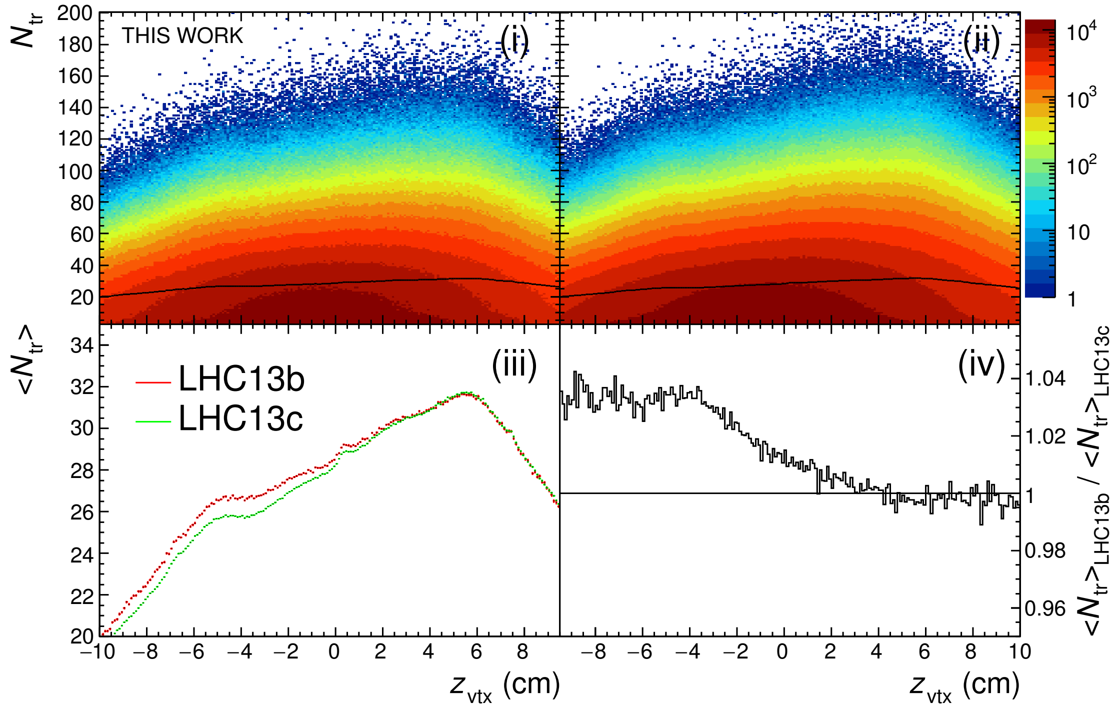

(a) Uncorrected N_{tr}

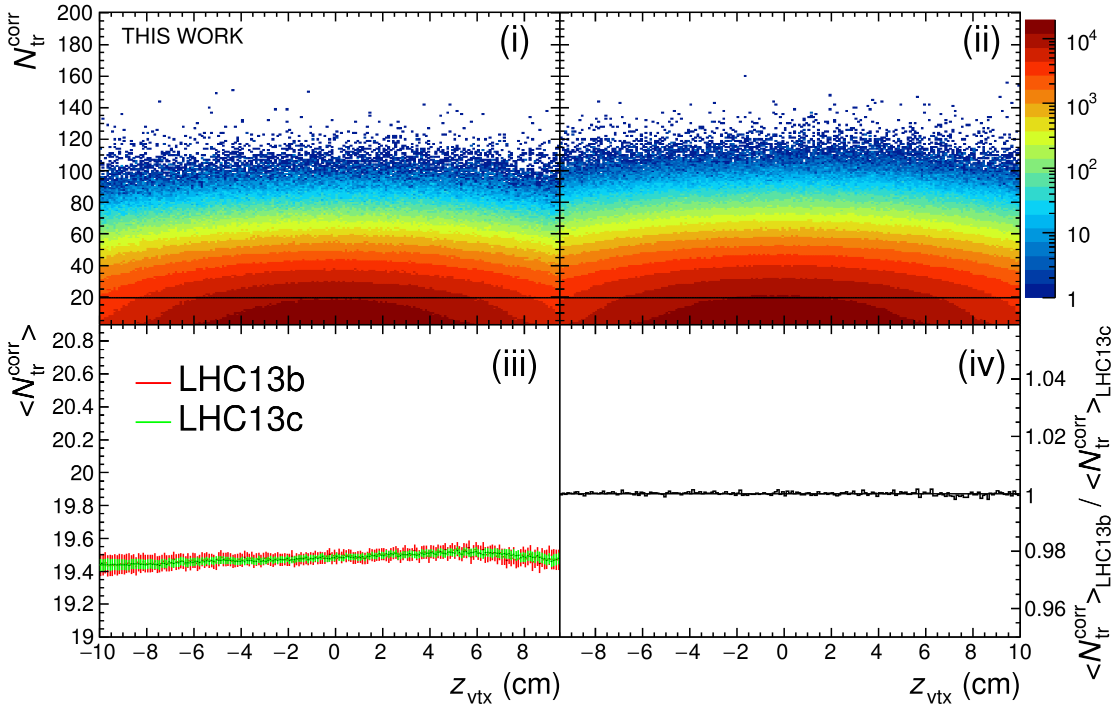

(b) Corrected $N_{\mathrm{tr}}^{\mathrm{corr}}$

Figure 4.2: Frequency distribution of N_{tr} ($N_{\mathrm{tr}}^{\mathrm{corr}}$) as function of z_{vtx} for the periods `LHC13b` in (i) and `LHC13c` in (ii). The black lines in (i) and (ii) represent the profiles $\langle N_{\mathrm{tr}} \rangle$ ($\langle N_{\mathrm{tr}}^{\mathrm{corr}} \rangle$) for each z_{vtx}. The profiles for both running periods are shown in panel (iii). The ratio between both profiles is shown in panel (iv).

4.1.2 V0A multiplicity

Alternatively, the signal in the backward rapidity V0A detector can be used to estimate the charged-particle multiplicity. The V0A detector is located in the direction of the Pb beam and measures a signal proportional to the number of charged particles hitting the scintillator material. The raw N_{V0A} frequency distribution is shown in Figure 4.3.

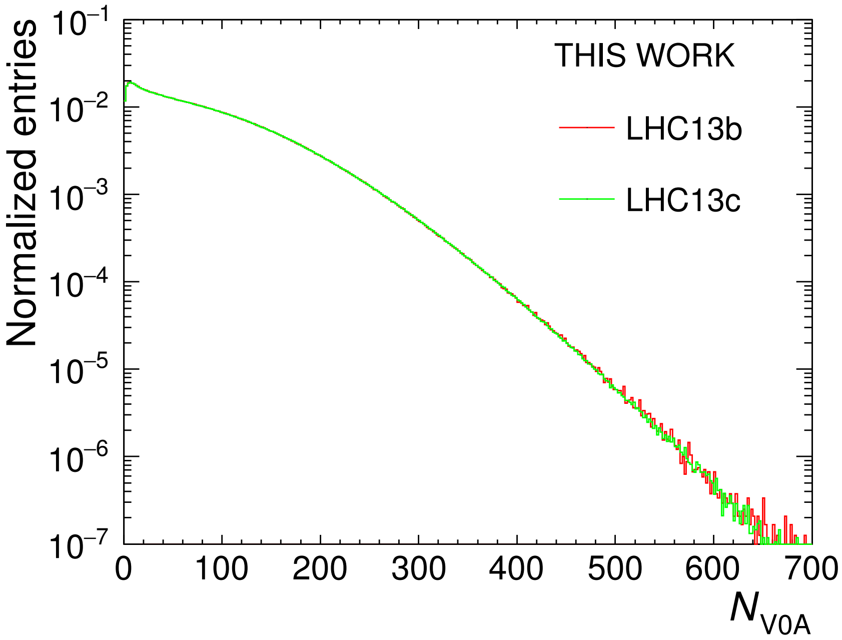

Figure 4.3: Frequency distribution of the raw signal N_{V0A} for the periods `LHC13b` and `LHC13c`.

The same procedure as for the N_{tr} correction is applied. The averages $\langle N_{\mathrm{V0A}}\rangle(z_{\mathrm{vtx}})$ shown in panel (iii) of Figure 4.4a are calculated from the asymmetric distribution of N_{V0A} as function of z_{vtx} shown in Figure 4.4a panel (i) and (ii). The monotonous dependence on z_{vtx} can be explained with the decreasing acceptance for increasing distance of the vertex from the V0A detector (located at 340 cm in z). Compared to the deviations for the SPD tracklet multiplicity distributions between `LHC13b` and `LHC13c` as function of z_{vtx}, the detector performance of the V0A detector is nearly constant over both periods.

The same Poissonian smearing is used to renormalize N_{V0A} on an event-by-event base from $\langle N_{\mathrm{V0A}}\rangle_{\mathtt{LHC13b}} = 87.28$ and $\langle N_{\mathrm{V0A}}\rangle_{\mathtt{LHC13c}} = 87.40$ to the global minimum of the profile of LHC13c which is $N^{\mathrm{glob}}_{\mathrm{V0A}} = 82.7$. Also in this case, the corrections yield to a homogeneous $N^{\mathrm{corr}}_{\mathrm{V0A}}(z_{\mathrm{vtx}})$ as shown in Figure 4.4b.

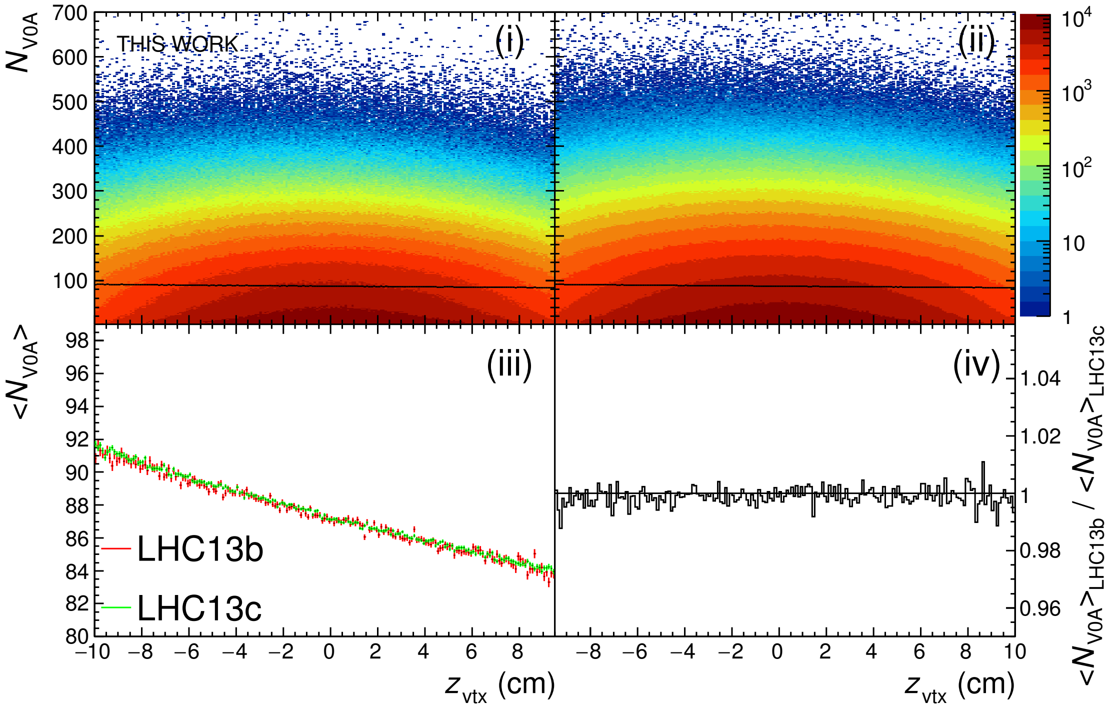

(a) Uncorrected N_{V0A}

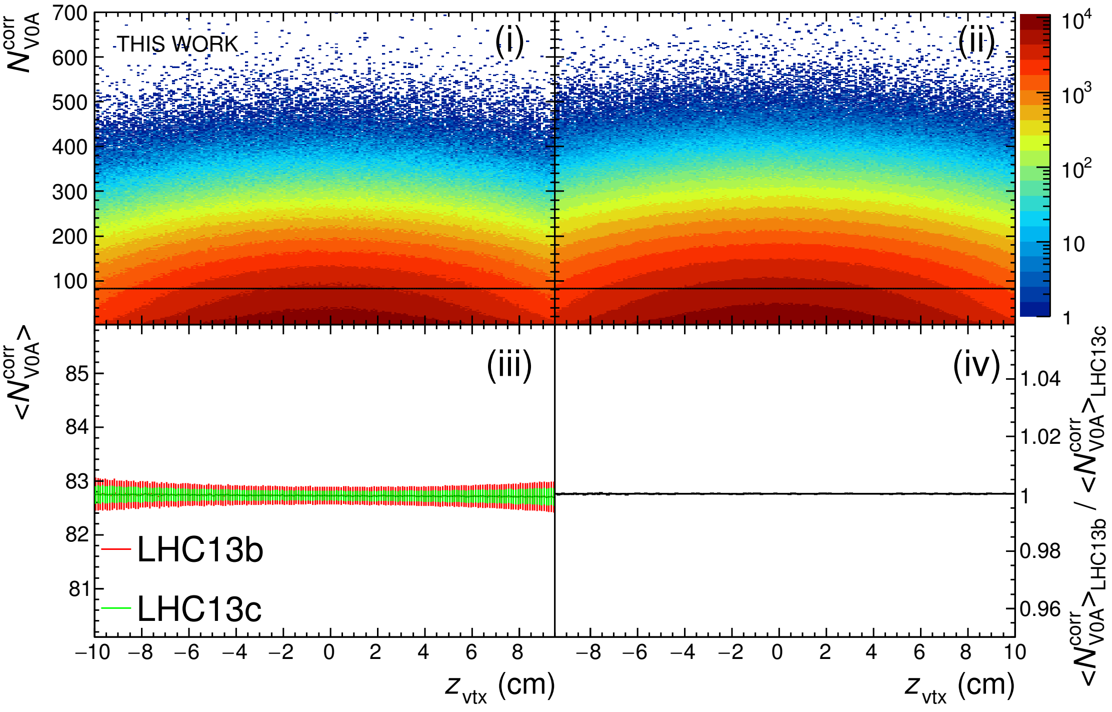

(b) Corrected $N^{\mathrm{corr}}_{\mathrm{V0A}}$

Figure 4.4: Frequency distribution of N_{V0A} ($N^{\mathrm{corr}}_{\mathrm{V0A}}$) as function of $\mathrm{z_{vtx}}$ for the periods `LHC13b` in (i) and `LHC13c` in (ii). The black lines in (i) and (ii) represent the profiles $\langle N_{\mathrm{V0A}}\rangle$ ($\langle N^{\mathrm{corr}}_{\mathrm{V0A}}\rangle$) for each $\mathrm{z_{vtx}}$. The profiles for both running periods are shown in panel (iii). The ratio between both profiles is shown in panel (iv).

4.1.3 Event multiplicity normalization

The relative yield of electrons from heavy-flavor hadron decays is measured as function of the relative charged-particle multiplicity. The corrected number of tracklets $N_{\mathrm{tr}}^{\mathrm{corr}}$ and corrected V0A signal $N_{\mathrm{V0A}}^{\mathrm{corr}}$ are split into multiplicity classes, abbreviated with the index i in the following, in which the yields of electrons from heavy-flavor hadron decays are measured. The $N_{\mathrm{tr}}^{\mathrm{corr}}$ distribution is subdivided into six multiplicity classes at these borders: {1, 22, 29, 35, 44, 70, 200}. The $N_{\mathrm{V0A}}^{\mathrm{corr}}$ distribution is subdivided into five classes at these borders: {0, 91, 133, 173, 227, 800}. The classes were optimized to cover a wide range of relative multiplicity and distributed evenly between the centers of each class. Within each class the means $\langle N_{\mathrm{tr}}^{\mathrm{corr}}\rangle_{\mathrm{i}}$ and $\langle N_{\mathrm{V0A}}^{\mathrm{corr}}\rangle_{\mathrm{i}}$ are used as central value for the respective class i. From $\langle N_{\mathrm{tr}}^{\mathrm{corr}}\rangle_{\mathrm{i}}$ a charged-particle density is calculated using Monte Carlo information. Afterwards the class values $\langle N_{\mathrm{tr}}^{\mathrm{corr}}\rangle_{\mathrm{i}}$ are normalized to a relative charged-particle density $\langle \mathrm{d}N_{\mathrm{ch}}/\mathrm{d}\eta\rangle_{\mathrm{i}}/\langle \mathrm{d}N_{\mathrm{ch}}/\mathrm{d}\eta\rangle$ using the charged-particle density measured by ALICE in the same pseudo-rapidity range [123]. The V0A signals $\langle N_{\mathrm{V0A}}^{\mathrm{corr}}\rangle_{\mathrm{i}}$ are directly related to a charged-particle multiplicity and are normalized to the total average $\langle N_{\mathrm{V0A}}^{\mathrm{corr}}\rangle$ to obtain relative charged-particle multiplicities.

Conversion from $N_{\mathrm{tr}}^{\mathrm{corr}}$ to $\mathrm{d}N_{\mathrm{ch}}/\mathrm{d}\eta$

To convert the corrected number of tracklets $N_{\mathrm{tr}}^{\mathrm{corr}}$ to a charged particle density $\mathrm{d}N_{\mathrm{ch}}/\mathrm{d}\eta$ Monte Carlo information is exploited. For each Monte Carlo event the number of charged particles is counted and correlated to the number of tracklets N_{tr} in Monte Carlo. ALICE has measured a linear dependence between $N_{\mathrm{tr}}^{\mathrm{corr}}$ and the number of charged particles in the same pseudo-rapidity range [123].

A Monte Carlo simulation with the same minimum-bias event selection as for the present measurement was generated. The simulation is based on the DPMJET [124] event generator and GEANT3 [92] for the propagation of the particles through the detector and for the simulation of the detector response. In Figure 4.5 the frequency distribution of N_{ch} as function of $N_{\mathrm{tr}}^{\mathrm{corr}}$ is shown. The distribution is fit with a linear function $N_{\mathrm{ch}}\left(N_{\mathrm{tr}}^{\mathrm{corr}}\right) = \alpha \cdot N_{\mathrm{tr}}^{\mathrm{corr}}$. The result of the fit yields $\alpha = 1.89$ which represents the proportionality factor between the number of tracklets and the number of charged particles. The calculated $\langle N_{\mathrm{tr}}^{\mathrm{corr}}\rangle_{\mathrm{i}}$ for each multiplicity class i is translated to a charged particle density by multiplication with α and dividing by the pseudo-rapidity range $\Delta\eta = 2$:

$$\langle \mathrm{d}N_{\mathrm{ch}}/\mathrm{d}\eta\rangle_{\mathrm{i}} = \frac{\langle N_{\mathrm{tr}}^{\mathrm{corr}}\rangle_{\mathrm{i}}}{\Delta\eta} \cdot \alpha \tag{4.3}$$

The relative charged-particle multiplicity is calculated by normalizing the calculated charged particle densities $\langle \mathrm{d}N_{\mathrm{ch}}/\mathrm{d}\eta\rangle_{\mathrm{i}}$ for each multiplicity class i with the measured charged particle density $\mathrm{d}N_{\mathrm{ch}}/\mathrm{d}\eta_{|\eta|<1} = 17.64 \pm 0.01\,(\mathrm{stat.}) \pm 0.68\,(\mathrm{syst.})$ [123]. The resulting values for the multiplicity classes are shown in column 4 of Table 4.1.

V0A multiplicity normalization

The average normalized charged-particle multiplicity estimated with the V0A detector is obtained by a data-driven approach due to the lack of a charged particle measurement at backward rapidity. The average V0A signal per multiplicity class is divided by the global average

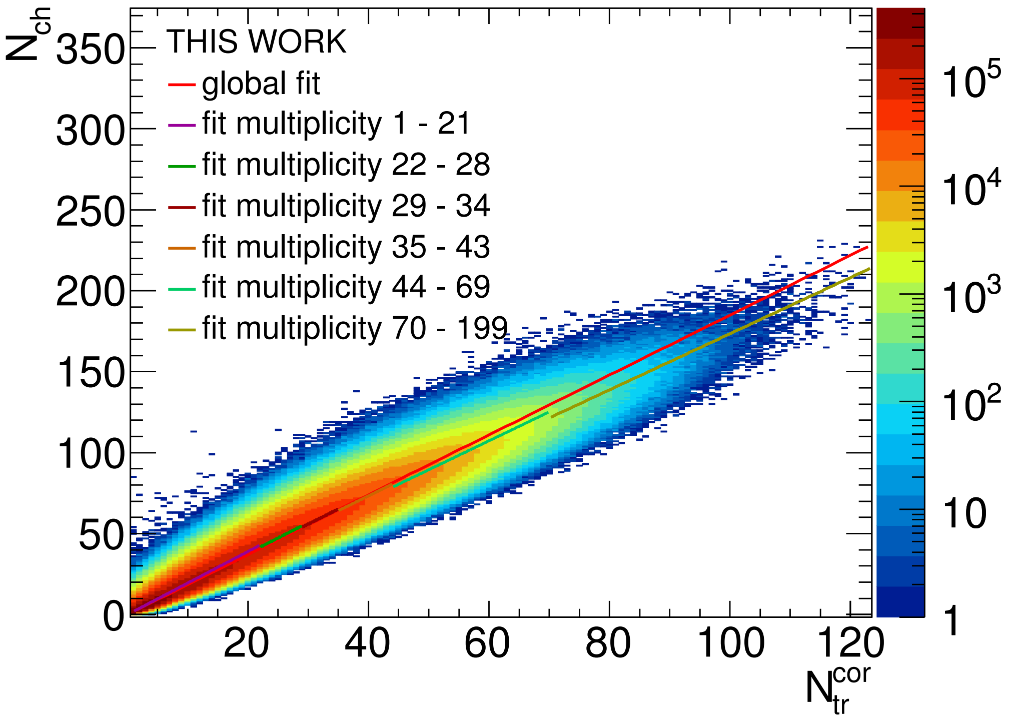

Figure 4.5: N_{ch} as function of N_{tr}^{corr} as obtained from the MC simulation with linear fits to the total distribution and to the single multiplicity intervals.

Table 4.1: Multiplicity classes using N_{tr} as estimator and corresponding values for $dN_{ch}/d\eta$.

N_{tr}	$< N_{tr} >$	α_i	$\frac{\langle dN_{ch}/d\eta\rangle_i}{\langle dN_{ch}/d\eta\rangle}$	$\frac{\langle dN_{ch}/d\eta\rangle_i}{\langle dN_{ch}/d\eta\rangle}$ (with α_i)	difference(%)	$N_{events}/10^6$
all	19.48	1.89				99.51
1-21	10.22	1.95	0.55	0.56	-3.04	60.68
22-28	24.83	1.88	1.33	1.32	0.47	13.45
29-34	31.35	1.88	1.68	1.67	0.33	8.47
35-43	38.56	1.88	2.07	2.06	0.36	8.15
44-69	51.92	1.85	2.78	2.73	2.00	6.99
70-200	77.78	1.83	4.17	4.04	3.20	0.54

V0A signal $N_{V0A}^{glob} = 82.7$. The different multiplicity classes and respective number of events per class are listed in Table 4.2.

Systematic uncertainties

Local deviations from the linear dependence between N_{tr}^{corr} and N_{ch} are studied by repeating the linear fit in each multiplicity class i with class dependent proportionality factors α_i. The average $\langle N_{tr}^{corr}\rangle_i$ are multiplied with the respective α_i. The results for the relative average charged particle densities $\langle dN_{ch}/d\eta\rangle_i/\langle dN_{ch}/d\eta\rangle$ are shown in column 5 of Table 4.1 and the deviation to the values obtained with the global α is shown in percent in column 6. These deviations are of the order of 3% and the residual width of the renormalization amounts to 2%. The systematic uncertainties of the calculated charged-particle densities is conservatively estimated to

Table 4.2: Multiplicity classes using N_{V0A} as estimator and corresponding values for $\mathrm{d}N_{\mathrm{ch}}/\mathrm{d}\eta$.

N_{V0A}	$< N_{\mathrm{V0A}} >$	$N_{\mathrm{V0A}}/ < N_{\mathrm{V0A}} >$	$\mathrm{N}_{events}/10^6$
all	82.73		99.72
0-90	39.80	0.48	62.23
91-132	109.56	1.32	16.54
133-172	150.31	1.82	9.93
173-226	195.21	2.36	6.93
227-798	273.15	3.30	4.08

5%, assuming full correlation between both uncertainty contributions. The uncertainties are in agreement with the measurement of D mesons as function of multiplicity with ALICE [76].

The evaluated uncertainty is assigned to both multiplicity estimators. At mid-rapidity also the systematic uncertainty on the measured charged particle density $\delta(\mathrm{d}N_{\mathrm{ch}}/\mathrm{d}\eta_{|\eta|<1}) = 3.85\%$ [123] has to be taken into account. The uncertainties are added in quadrature and the resulting systematic uncertainties are 6.3% for $\langle \mathrm{d}N_{\mathrm{ch}}/\mathrm{d}\eta \rangle_{\mathrm{i}}/\langle \mathrm{d}N_{\mathrm{ch}}/\mathrm{d}\eta \rangle$ and 5% for $\langle N^{\mathrm{corr}}_{\mathrm{V0A}} \rangle_{\mathrm{i}}/\langle N^{\mathrm{corr}}_{\mathrm{V0A}} \rangle$.

4.2 Event multiplicity dependent measurement

The multiplicity dependence of the yield of electrons from heavy-flavor hadron decays is studied by measuring the yield in different multiplicity classes and normalizing it to the multiplicity integrated result. The subdivision into multiplicity classes makes it necessary to reduce the number of p_{T} intervals due to the finite statistics of the measurement. Only a small fraction of the events have very high multiplicity and the heavy-flavor yield decreases substantially with increasing p_{T}. Therefore, the number of p_{T} bins for the analysis was reduced to three: $0.5 < p_{\mathrm{T}} < 2\,\mathrm{GeV}/c$, $2 < p_{\mathrm{T}} < 4\,\mathrm{GeV}/c$, $4 < p_{\mathrm{T}} < 8\,\mathrm{GeV}/c$. Because of the increasing fraction of electrons from beauty-hadron decays at high p_{T}, the result for the highest p_{T} interval is interesting as it might reflect a the multiplicity dependence of the beauty production. It is not possible to have finer p_{T} intervals in the region $4 < p_{\mathrm{T}} < 8\,\mathrm{GeV}/c$ with the currently available statistics.

In this analysis, the same steps as in the multiplicity independent one are applied (see Sections 3.4.1, 3.5 and 3.6). The study of the yield as function of multiplicity and p_{T} makes the analysis more complex, since all corrections, in principle, have to be evaluated as function of p_{T} and multiplicity. However, for corrections without multiplicity dependence the results of the inclusive analysis can be used.

In this sections a possible multiplicity dependence of the corrections is investigated.

4.2.1 Track selection and electron identification

The electron selection is done in the same way as described in Section 3.4 for the case of combined TPC and TOF electron identification. A possible dependence of the hadron contamination is evaluated by estimating the hadron contamination as function of momentum in the different multiplicity classes. The estimated p_{T}-dependent hadron contamination for the different multiplicity classes is in agreement with the multiplicity independent hadron contamination within the statistical uncertainties as shown in Figure 4.6. Therefore, the hadron contamination parametrization evaluated in the inclusive analysis (Section 3.4.1) can be used to statistically re-

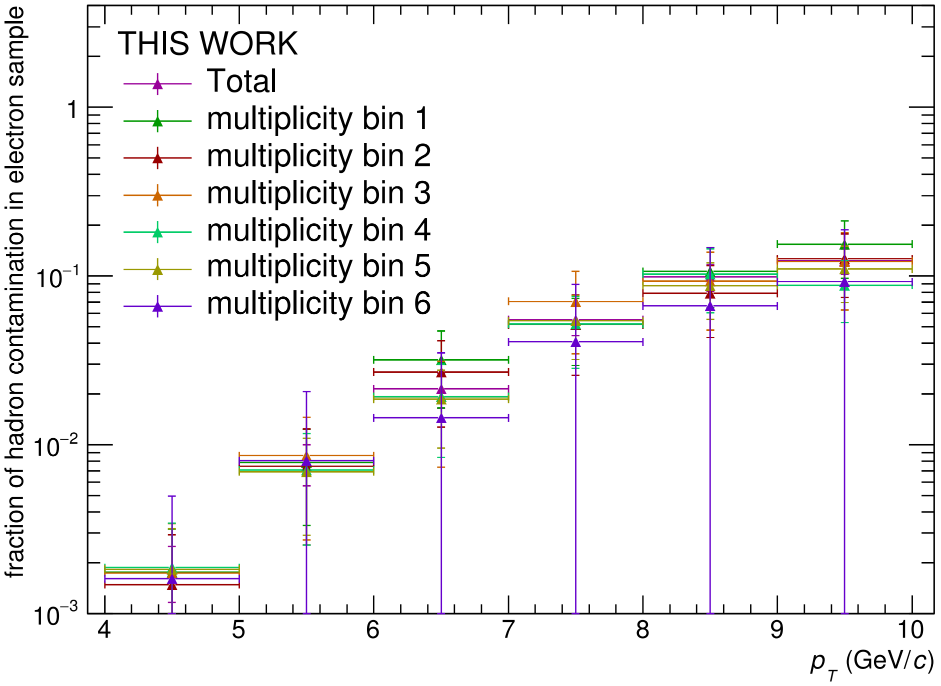

Figure 4.6: Comparison of the hadron contamination for different multiplicity classes with the multiplicity integrated reference.

move the remaining hadron contamination for the raw electron yield of each multiplicity class. A possible multiplicity dependence of the track selection criteria is checked by calculating the efficiency (see Section 3.6) in the different multiplicity classes. In Figure 4.7 the efficiencies are shown as function of the multiplicity for all three p_T intervals. The efficiencies agree with each other for all multiplicity classes within the individual transverse-momentum bin. Thus, the correction for tracking efficiency and geometric acceptance is independent of the multiplicity. The raw non-photonic yield can be corrected with the efficiency evaluated in the inclusive analysis (Section 3.6). However, since in this analysis self-normalized yields are calculated, the corrections cancel each other in the numerator and denominator (described in detail in Section 4.4).

4.2.2 Multiplicity dependence of the background

The electron background of electrons not coming from heavy flavor hadron decays needs to be determined for each multiplicity class. The cocktail based method would require to calculate an individual cocktail for each multiplicity class using measured pion spectra for exactly the same multiplicity classes, which are not available at this point. However, the method of tagging the photonic yield (see Section 3.5.2) is not dependent on external measurements and thus makes the multiplicity dependent analysis of electrons from heavy-flavor hadron decays possible. The photonic yield is measured as function of p_T and multiplicity, corrected with the tagging efficiency and subtracted from the inclusive yield of electrons. Using the same strategy as discussed in the previous section, the tagging efficiency is evaluated concerning its multiplicity dependence and treated accordingly. The multiplicity dependence on the removal of the

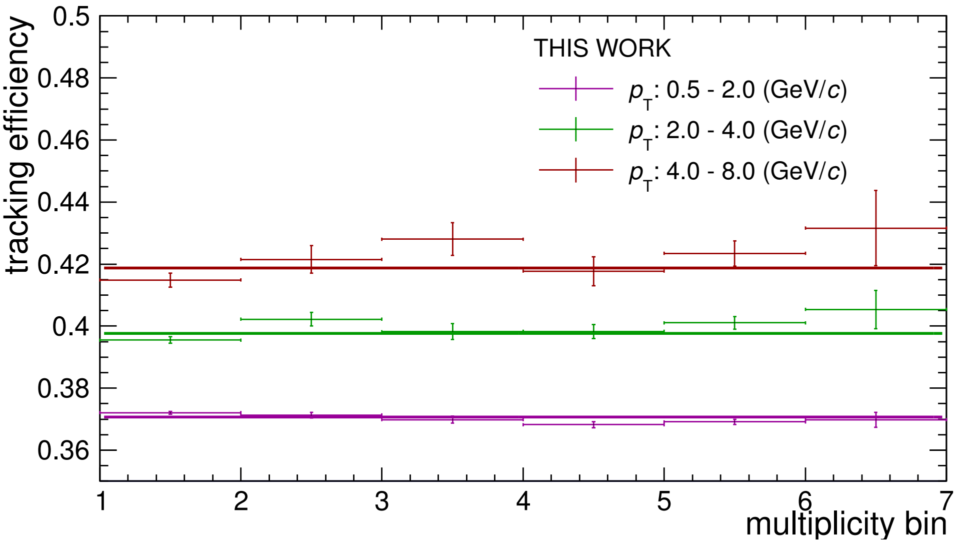

Figure 4.7: Tracking efficiency for the different p_T intervals as function of the multiplicity class.

non-photonic background contributions from J/ψ and K_{e3} decays (see Section 3.5.1) is also studied.

Photonic background

The raw photonic yield is determined in the same way as described in Section 3.5.2 for each multiplicity class. However, the tagging efficiency, which is used to correct the raw photonic yield might have a dependence on the multiplicity. In Figure 4.8 the tagging efficiency is calculated as function of the multiplicity for all three transverse-momentum intervals. The tagging efficiency in different multiplicity classes agree with each other within the statistical uncertainties for all p_T intervals. The multiplicity independent tagging efficiency evaluated in the inclusive analysis, which is described in Section 3.5.2, is used to correct the raw photonic yields for each multiplicity class.

Non-photonic background

In the inclusive analysis the yield of electrons from weak kaon decay (K_{e3}) and J/ψ decays are subtracted from the non-photonic electron yield using the information extracted from the cocktail approach (see Section 3.5.1). In the multiplicity dependent analysis this component has to be subtracted as well before the self-normalized yields can be computed. The multiplicity dependence of the K_{e3} and J/ψ background have to be estimated. As described in Section 3.5.1, the combined background yield of electrons from J/ψ and K_{e3} decays is not significant (3% of the yield of electrons from heavy-flavor hadron decays). Thus, the estimate of the multiplicity dependence will have little influence on the result. As a first order approximation, the same multiplicity dependence for electrons from J/ψ and K_{e3} decays as for the electrons from heavy-flavor hadron decays is assumed. This assumption is supported by a compatible multiplicity dependence between D mesons and J/ψ in pp collisions at $\sqrt{s} = 7\,\text{TeV}$ measured by ALICE [118]. A conservative estimate of 50% for the systematic uncertainty on the multiplicity

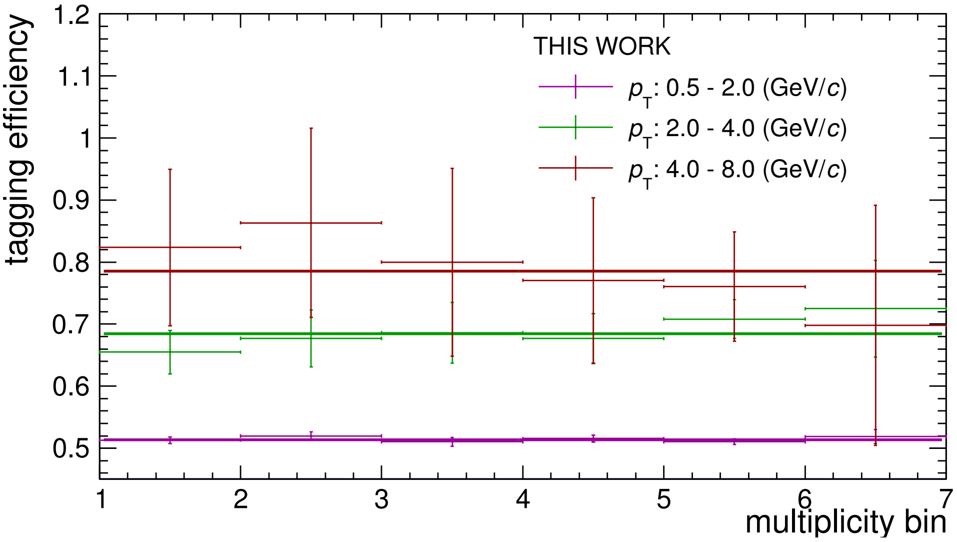

Figure 4.8: Tagging efficiency for the different p_T intervals as function of the multiplicity class.

dependence is used. The self-normalized yield of electrons from heavy-flavor hadron decays (r_i) for the multiplicity class i can be written as:

$$r_i = \frac{Y_i}{Y} = \frac{C'_i - (J' + K') \cdot m_i}{C' - (J' + K')} \tag{4.4}$$

where C'_i and C' the event normalized non-photonic yields, J' and K' the event normalized yields of electrons from J/ψ and K_{e3}. The factor m_i scales the multiplicity independent yields J' and K' to the respective yields as function of the average charged-particle multiplicity. As mentioned above, the dependence of the J/ψ and K_{e3} yields as function of charged particle multiplicity is not measured and has to be estimated. By assuming a similar multiplicity dependence of the J/ψ and K_{e3} yields compared to the measurement of electrons from heavy-flavor hadron decays ($m_i \approx r_i$), the equation 4.4 simplifies to:

$$r_i = \frac{Y_i}{Y} = \frac{C'_i}{C'} \tag{4.5}$$

4.3 Systematic uncertainties

The analysis of the systematic uncertainties for the self-normalized yield of electrons from heavy-flavor hadron decays differs from the evaluation of the systematic uncertainties in the inclusive analysis. Since the yields for the multiplicity classes are normalized to the multiplicity integrated yield, the correlated systematic uncertainties between the multiplicity dependent yields in the numerator and the multiplicity independent yields in the denominator cancel in the ratio. Most of the uncertainties evaluated in Section 3.7 are correlated in multiplicity and p_T. Variation of the selection criteria are done to estimate residual systematic uncertainties which do not cancel in the ratio. In this section systematic uncertainties are studied as a function of the charged-particle multiplicity and the transverse momentum.

4.3.1 Variation of the selection criteria

To determine the residual systematic uncertainty on the track and eID selection criteria which does not cancel in the normalization, the optimized selection criteria are varied to lower and higher values in the same way as described in Section 3.7. The values used for the estimation of the systematic uncertainty are listed in Table 4.3. For each variation of the selection criteria a new self-normalized yield of electrons from heavy-flavor hadron decays as function of p_{T} and multiplicity class is calculated. Then, the ratio between the relative yield with the varied selection criterion and the relative yield with the default selection criterion is computed. The statistical uncertainties of the default self-normalized yields and those with varied selection criteria were treated as uncorrelated and added in quadrature. All ratios are compatible with unity within their statistical uncertainties. However, this method of obtaining systematic uncertainties, which is used in the inclusive analysis (see Section 3.7), gives inconclusive results due to the large statistical uncertainties of the self-normalized yields.

Table 4.3: Variations of the selection criteria for the inclusive and associated electron.

Observable	Reference	Variation inclusive track
DCA xy and z	(10,20)	(5,10),(20,50)
kink mothers	accepted	rejected
ITS layer	4	3, 5, 6
SPD	kBoth	kFirst 4,5
TPC cluster	100	90, 95, 105, 110, 115, 120
TPC PID cluster	80	60, 70, 90, 100
TOF PID	$3\sigma_{\mathrm{e-TOF}}$	1.5, 2, 2.5, $4\sigma_{\mathrm{e-TOF}}$
TPC PID lower cut	$-0.5\sigma_{\mathrm{e-TPC}}$ (69%)	$0.09\sigma_{\mathrm{e-TPC}}$ (50%) $-0.17\sigma_{\mathrm{e-TPC}}$ (60%) $-0.94\sigma_{\mathrm{e-TPC}}$ (84%)

Observable	Reference	Variation associated track
DCA xy and z	(10,20)	(5,10),(20,50)
ITS layer	2	3, 4, 5
TPC (cls, PID cls)	(80,60)	(80,70), (100,60), (100,80)
TOF PID	$0\sigma_{\mathrm{e-TOF}}$	$3\sigma_{\mathrm{e-TOF}}$
TPC PID	$\pm 3\sigma_{\mathrm{e-TPC}}$	2, $4\sigma_{\mathrm{e-TPC}}$

A different approach of estimating the systematic uncertainties for the self-normalized yields as function of p_{T} and multiplicity is used: The values of the ratios between the self-normalized yields with default and altered selection criteria are filled into a frequency distribution for each multiplicity class and p_{T} bin as shown in Figure 4.9 and 4.10, respectively for the multiplicity dependence at mid-rapidity and at backward rapidity. The distributions were fitted with a Gaussian parametrization. The deviation of the mean from one and the width of the fitted Gauss distribution are added to estimate the systematic uncertainty.

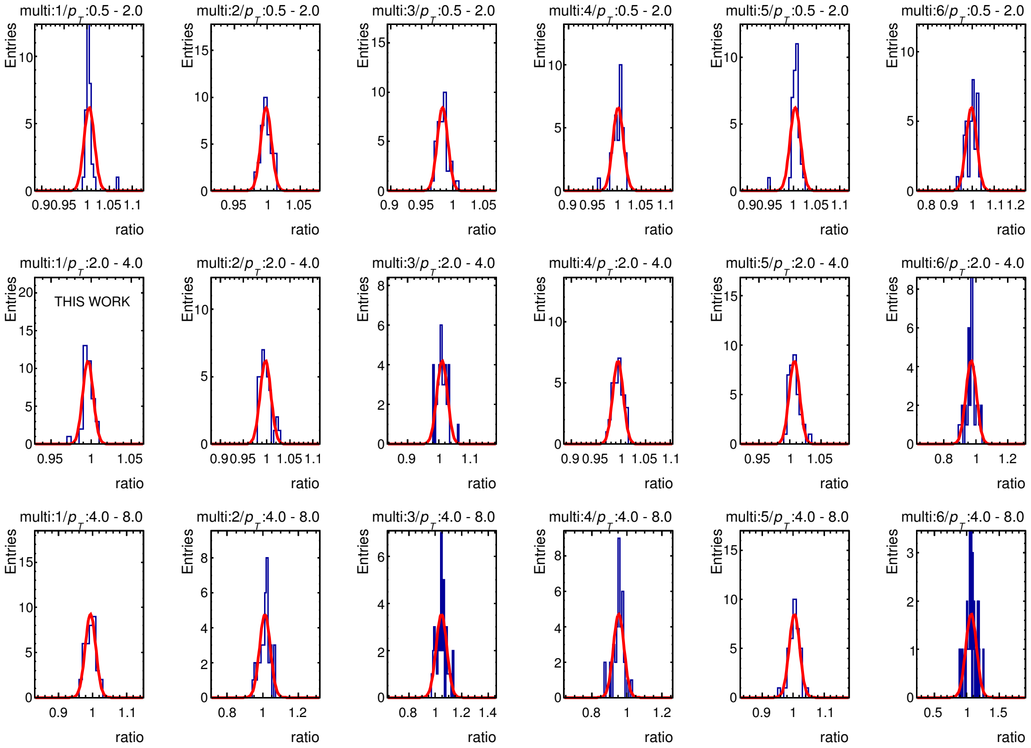

Figure 4.9: Frequency distribution of all selection criteria variations for all p_{T} intervals and multiplicity classes using N_{tr} as multiplicity estimator at mid-rapidity.

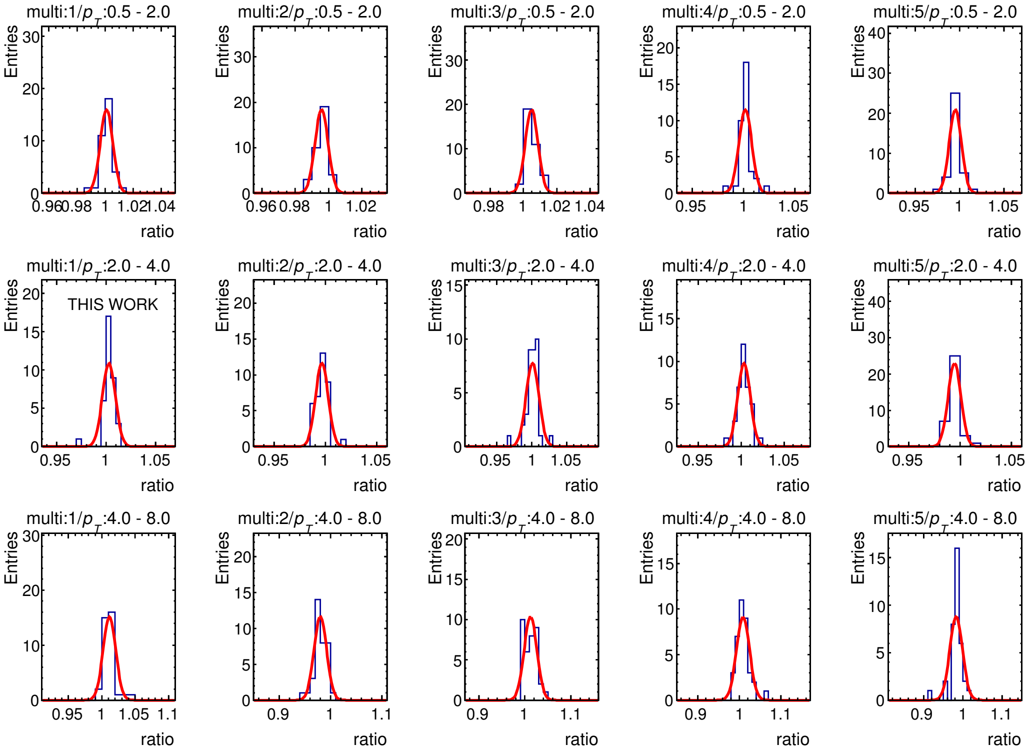

Figure 4.10: Frequency distribution of all selection criteria variations for all p_{T} intervals and multiplicity classes using N_{V0A} as multiplicity estimator at backward rapidity.

To cross check the dependence of the evaluated uncertainties on the choice of the fit function for the distribution, also a uniform distribution was tested. The standard deviation for a uniform distribution U is calculated as $\sqrt{V_{\mathrm{U}}(H)} = \frac{max(H)-min(H)}{\sqrt{12}}$, with H being the frequency distribution. The calculated uncertainties for both methods agree reasonably with each other as shown in Figure 4.11 and 4.12.

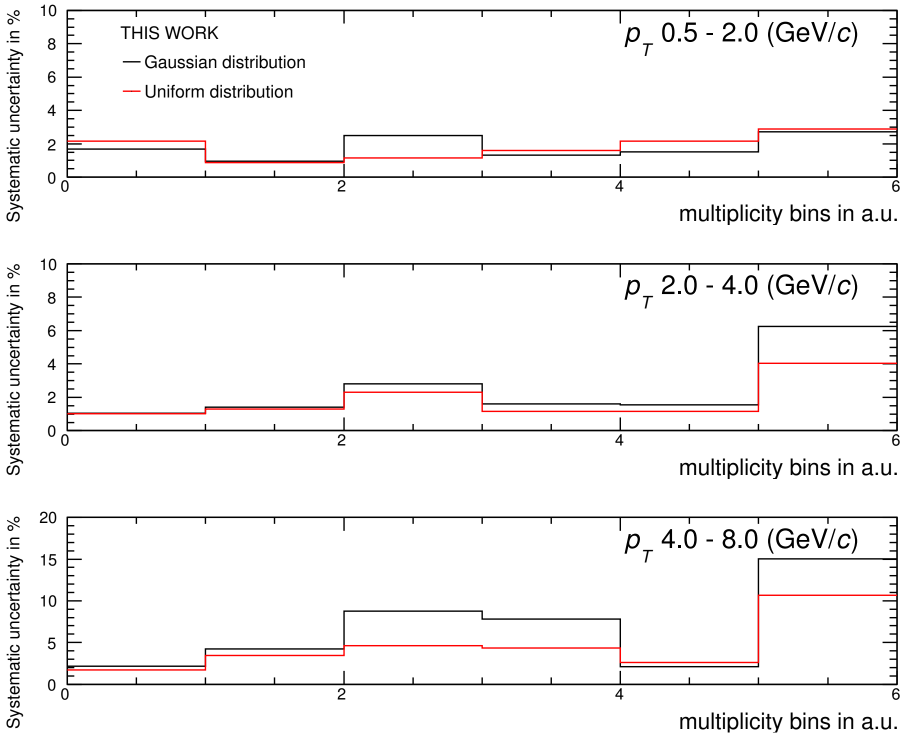

Figure 4.11: Comparison of the obtained uncertainties with the Gaussian fit (black) and a uniform distribution (red) for all p_{T} intervals and multiplicity classes using N_{tr} as multiplicity estimator at mid-rapidity.

Fluctuations are observed due to the remaining problem of limited statistics in the single p_{T} intervals and multiplicity classes. The study of the systematic uncertainties is repeated by merging multiplicity classes: For the case of $N_{\mathrm{tr}}^{\mathrm{corr}}$ the six multiplicity classes were merged to three classes while for the $N_{\mathrm{V0A}}^{\mathrm{corr}}$ case the last four classes were merged to two classes. The frequency distribution for each merged multiplicity class and p_{T} bin is shown in Figure 4.13 and 4.14. The relative uncertainties as function of the merged multiplicity classes are shown in the Figures 4.15 and 4.16. The Figures show comparable systematic uncertainties for both multiplicity estimators and also for both methods of describing the distribution of the ratios (Gaussian and uniform). The uncertainties are independent of the multiplicity classes for both multiplicity estimators and are 1% for $0.5 < p_{\mathrm{T}} < 4\,\mathrm{GeV}/c$ and 2% for $4 < p_{\mathrm{T}} < 8\,\mathrm{GeV}/c$.

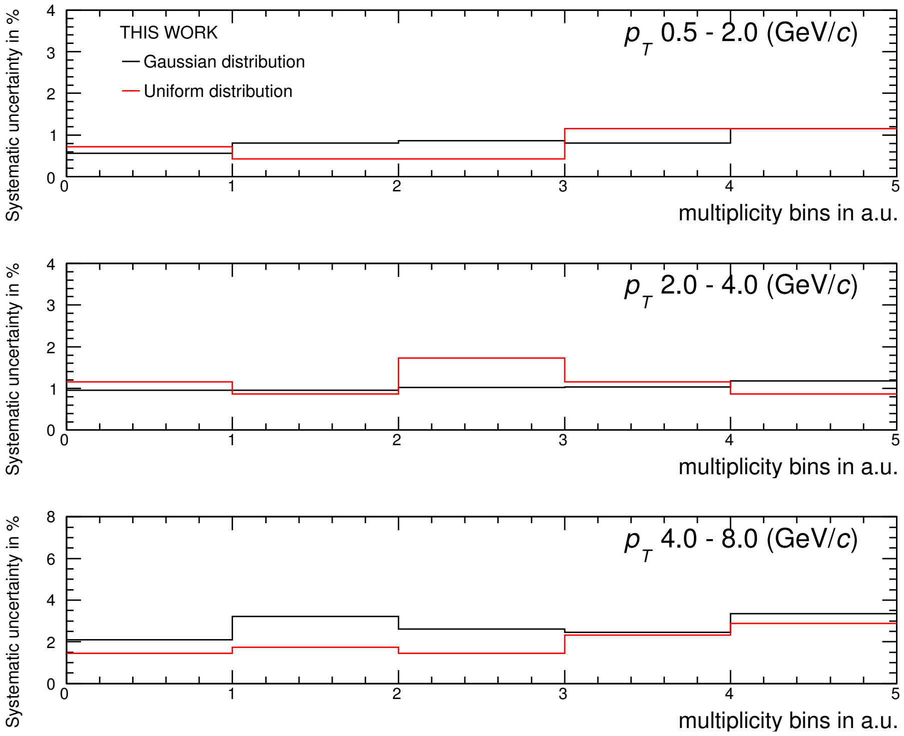

Figure 4.12: Comparison of the obtained uncertainties with the Gaussian fit (black) and a uniform distribution (red) for all p_{T} intervals and multiplicity classes using N_{V0A} as multiplicity estimator at backward rapidity.

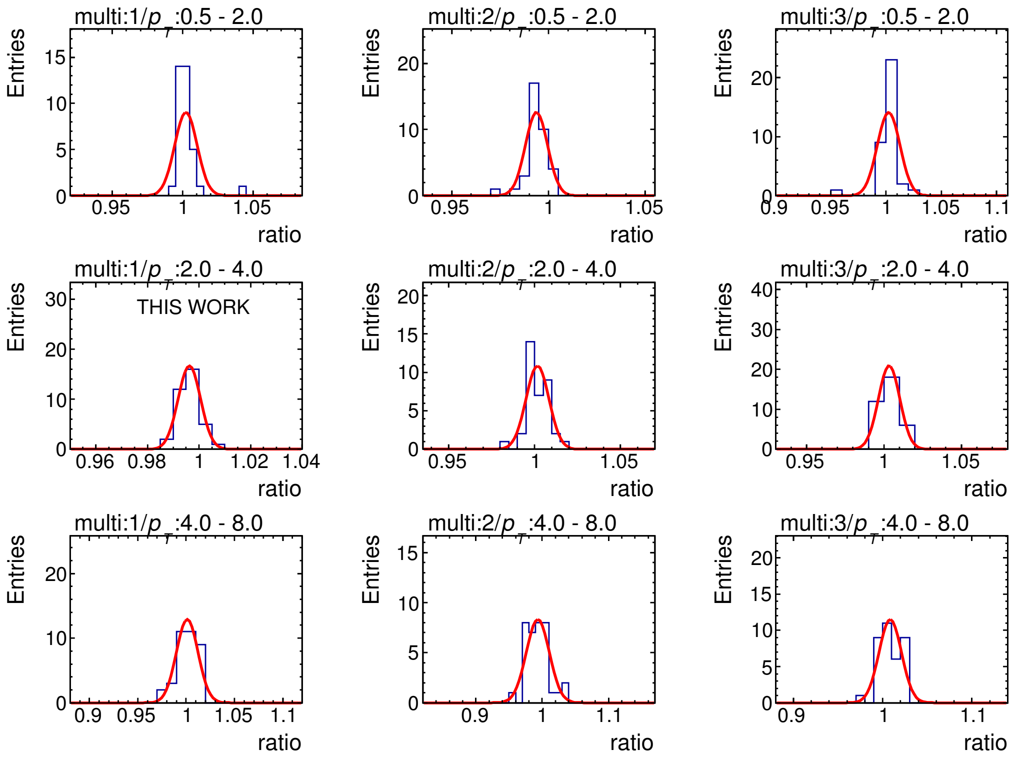

Figure 4.13: Frequency distribution of all selection criteria variations for all p_{T} intervals and merged multiplicity classes using N_{tr} as multiplicity estimator at mid-rapidity.

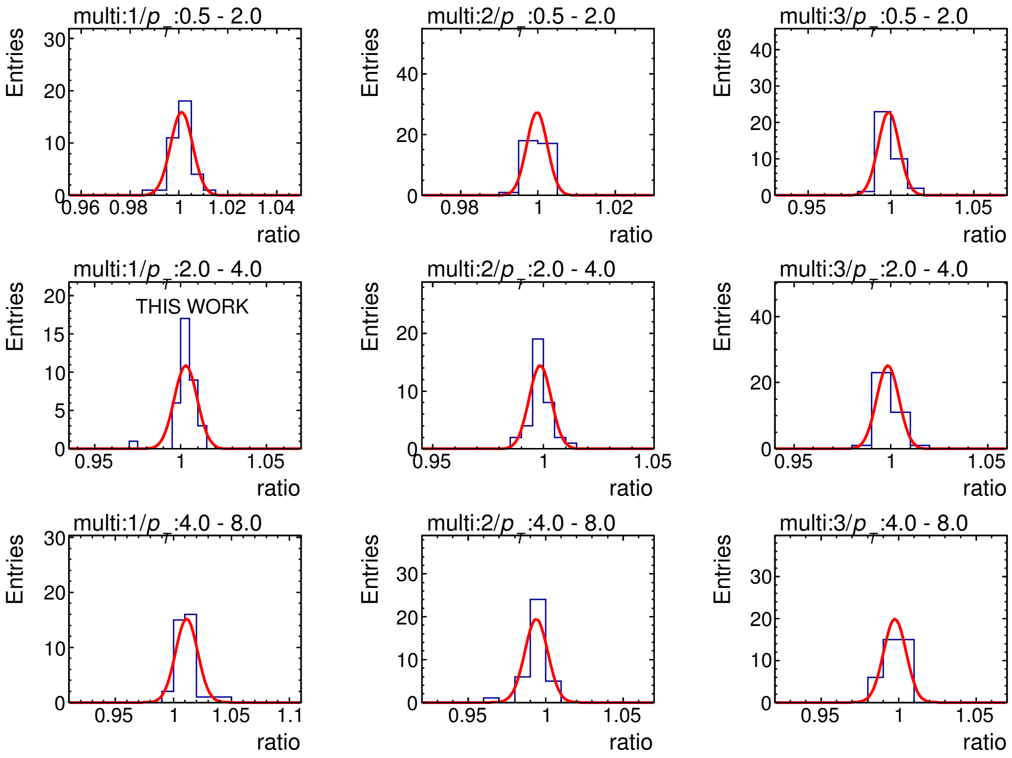

Figure 4.14: Frequency distribution of all selection criteria variations for all p_{T} intervals and merged multiplicity classes using N_{V0A} as multiplicity estimator at backward rapidity.

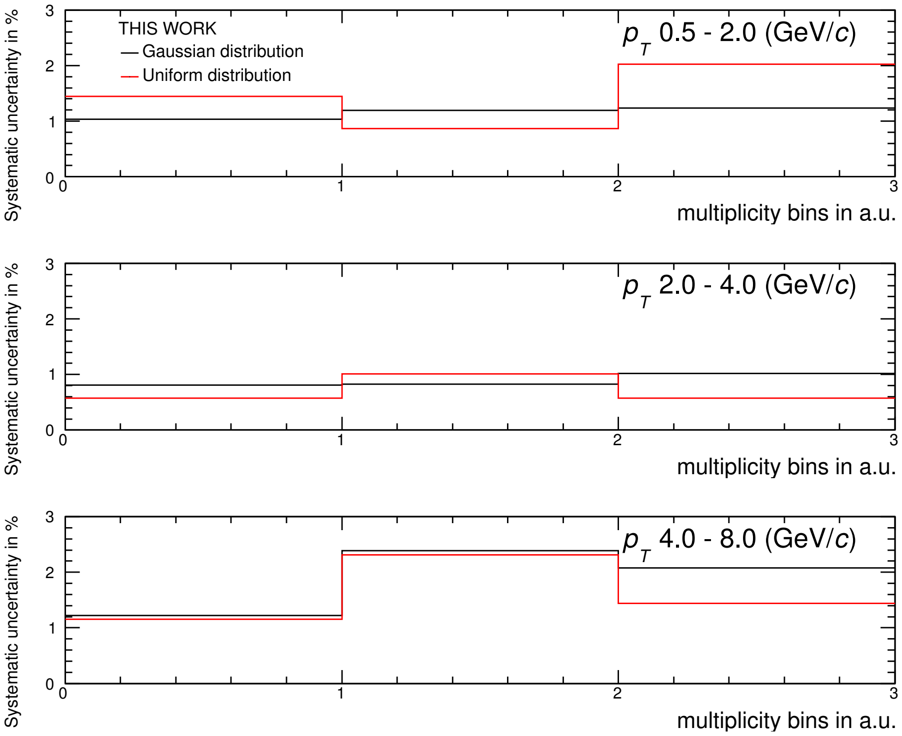

Figure 4.15: Comparison of the uncertainties obtained with the Gaussian fit (black) and a uniform distribution (red) for all p_{T} intervals and merged multiplicity classes using N_{tr} as multiplicity estimator at mid-rapidity.

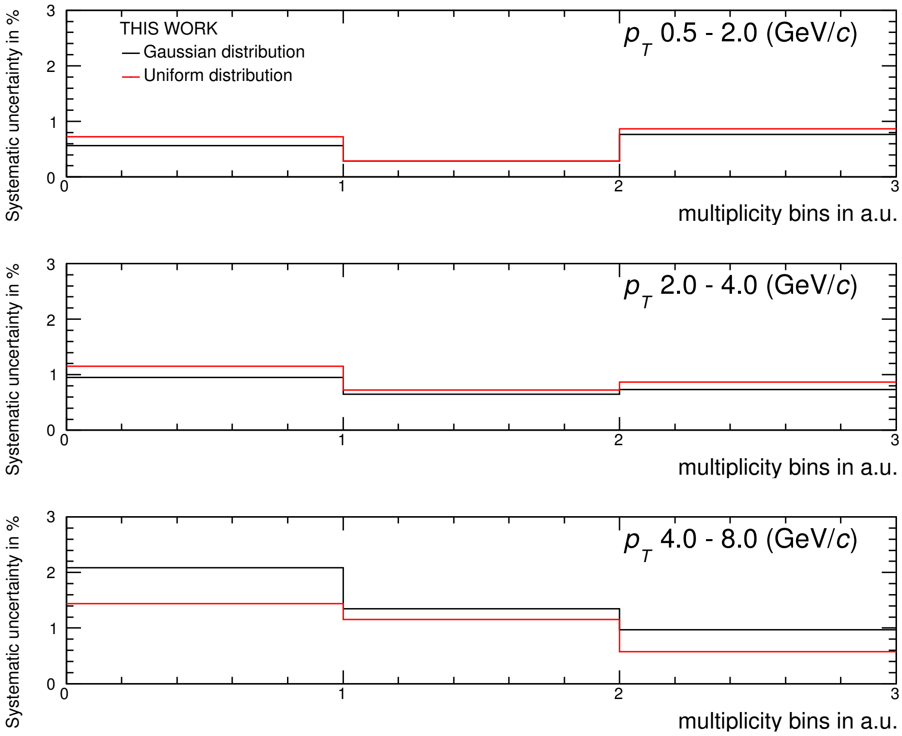

Figure 4.16: Comparison of the uncertainties obtained with the Gaussian fit (black) and a uniform distribution (red) for all p_{T} intervals and merged multiplicity classes using N_{V0A} as multiplicity estimator at backward rapidity.

4.3.2 Non-photonic background

In Section 4.2.2 the multiplicity dependence of the background of electrons from J/ψ and K_{e3} decays is assumed to be similar to the multiplicity dependence of electrons from heavy-flavor hadron decays (see Equation 4.4). The non-photonic background cancels in the normalization due to this assumption as shown in Equation 4.5. However, the uncertainty on this assumption needs to be propagated to the calculation of the uncertainty of the normalized yields. In general the uncertainty of the normalized yield r_{i} for multiplicity class i can be expressed as:

$$\Delta r_{\mathrm{i}} = \sqrt{(\left(\frac{\partial r}{\partial m_{\mathrm{i}}}\Delta m_{\mathrm{i}}\right)^2 + \left(\frac{\partial r}{\partial J'}\Delta J'\right)^2 + \left(\frac{\partial r}{\partial K'}\Delta K'\right)^2} \tag{4.6}$$

$$\frac{\partial r}{\partial m_{\mathrm{i}}}\Delta m_{\mathrm{i}} = -\frac{J'+K'}{C'-J'-K'}\delta m_{\mathrm{i}} \cdot m_{\mathrm{i}} \tag{4.7}$$

$$\frac{\partial r}{\partial J'} = \frac{\partial r}{\partial K'} = \frac{C'_{\mathrm{i}} - C' \cdot m_{\mathrm{i}}}{(C'-J'-K')^2} \overset{m_{\mathrm{i}}C'=C'_{\mathrm{i}}}{=} 0 \tag{4.8}$$

$$\delta r_{\mathrm{i}} = \frac{1}{r_{\mathrm{i}}}\sqrt{\left(\frac{\partial r}{\partial m_{\mathrm{i}}}\Delta m_{\mathrm{i}}\right)^2} \approx \frac{J'+K'}{C'-J'-K'}\delta m_{\mathrm{i}} \tag{4.9}$$

The uncertainties are propagated by Gaussian error propagation. The derivatives with respect to the yields of electrons from J/ψ (J') and K_{e3} (K') decays become zero and the only contributions to the systematic uncertainty of the self-normalized yields r_{i} come from the uncertainty on the multiplicity dependence of electrons from J/ψ and K_{e3} decays. As mentioned before, multiplicity studies in pp collisions [117] of J/ψ and D mesons agree reasonable with each other. The deviations between the multiplicity dependence of J/ψ and D mesons are not larger than 50%. Therefore, the uncertainty on the multiplicity dependence of the non-photonic background is estimated to be also in the range of 50%. With Equation 4.9 the uncertainties are computed to be less or comparable with 2% for all p_{T} bins. As a conservative estimate 2% is used as a multiplicity and p_{T} independent systematic uncertainty resulting from the assumptions on the multiplicity dependence of the non-photonic background.

4.3.3 Weighting functions

As described in Section 3.5.2, the light meson spectra in the Monte Carlo simulation need to be reweighted for the calculation of the tagging efficiency to correct the raw photonic yield.

However, no multiplicity dependence is applied to the reweighting functions. The reweighting functions are recalculated with modified light meson spectra to obtain a sensitivity for the influence on the reweighting functions. The p_{T}-differential cross sections for pions for different centrality classes are provided in [125] and plotted in Figure 4.17 (top panel). The centrality dependent cross sections were normalized to the minimum bias cross section as shown in the lower plot of Figure 4.17.

The centrality classes are related to the multiplicity classes used in this analysis as shown in Table 4.4. The relation between centrality class and charged particle density $\langle \mathrm{d}N_{\mathrm{ch}}/\mathrm{d}\eta \rangle$ is obtained from [75] and divided by the measured charged particle density $\langle \mathrm{d}N_{\mathrm{ch}}/\mathrm{d}\eta \rangle_{|\eta|<1} = 17.64$.

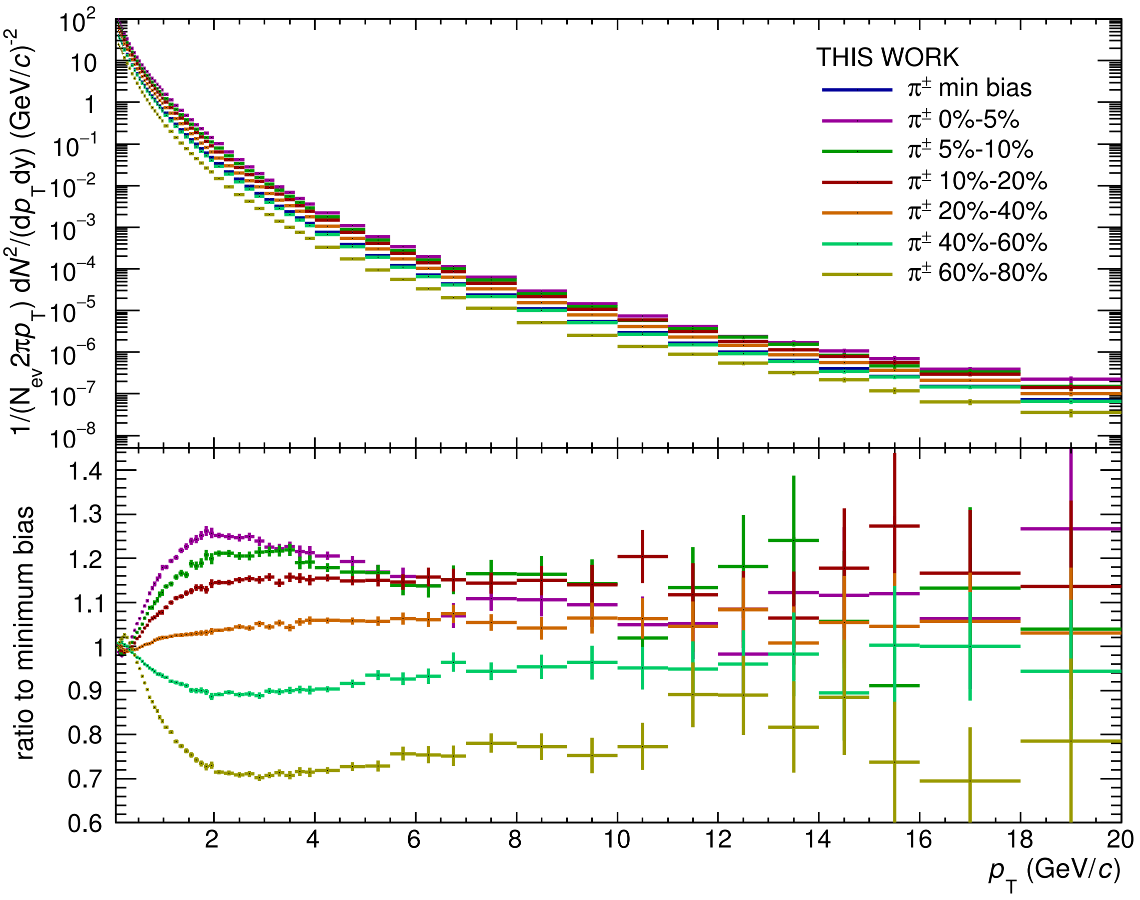

Figure 4.17: Spectra of charged pions for different centrality classes (top) [125] measured in p-Pb collisions at $\sqrt{s_{\mathrm{NN}}} = 5.02\,\mathrm{TeV}$ with ALICE. Spectra divided by the minimum bias spectrum of charged pions (bottom).

The most peripheral centrality class (80%–100%) is omitted in the study because it is outside the multiplicity range of this analysis. The reweighting functions are recalculated using each of the provided pion spectra. The parametrization of the measured pion spectra is multiplied with each of the ratios shown in the lower panel of Figure 4.17. As described in 3.5.2, the other light meson spectra are calculated by m_{T} scaling of the modified pion spectra. Thus, a set of reweighting functions for each centrality class is calculated for each of the light meson spectra (π^0, η, ω, ϕ, η' and ρ). The modified reweighting functions calculated with the different centrality dependent pion spectra are shown in Figure 4.18. In the calculation of the self-normalized yields the modified reweighting functions are used only for the numerator (multiplicity dependent yields), while for the denominator (multiplicity independent yields) the default reweighting functions are used. The ratios between the self-normalized yields with modified reweighting functions and the self-normalized yields with the default reweighting functions are shown in the three bottom panels of Figure 4.19 for the three p_{T} intervals, respectively. The figure shows that at $p_{\mathrm{T}} > 2\,\mathrm{GeV}/c$ the electron background from photonic decays is much smaller and changes of the reweighting functions have negligible influence. For $0.5 < p_{\mathrm{T}} < 2\,\mathrm{GeV}/c$ the self-normalized yields vary up to 5% with respect to the self-normalized yields using the default reweighting functions. A systematic uncertainty of 5% is assigned independent on multiplicity

Table 4.4: Relation between centrality classes and charged-particle multiplicity. Adapted from [75].

centrality class	$\langle \mathrm{d}N_{\mathrm{ch}}/\mathrm{d}\eta \rangle_i$ / $\langle \mathrm{d}N_{\mathrm{ch}}/\mathrm{d}\eta \rangle_{\lvert\eta\rvert<1}$
0–5%	2.56
5–10%	2.06
10–20%	1.73
20–40%	1.32
40–60%	0.91
60–80%	0.56

in $0.5 < p_{\mathrm{T}} < 2\,\mathrm{GeV}/c$ to quantify the influence of a multiplicity dependence of the reweighting functions.

4.3.4 Summary of the systematic uncertainties

Table 4.5: Systematic uncertainties on the self-normalized yields from various sources

type	$0.5 < p_{\mathrm{T}} < 2\,\mathrm{GeV}/c$	$2 < p_{\mathrm{T}} < 4\,\mathrm{GeV}/c$	$4 < p_{\mathrm{T}} < 8\,\mathrm{GeV}/c$
track cut variations	1%	1%	2%
non-photonic background	2%	2%	2%
reweighting	5%	0%	0%
total	5.5%	2.2%	2.8%

The uncertainties on the self-normalized yields are summarized in Table 4.5. The uncertainties are treated as uncorrelated and thus are added in quadrature. In total the combined uncertainties are (5.5%, 2.2%, 2.8%) independent of the multiplicity classes for the three p_{T} intervals.

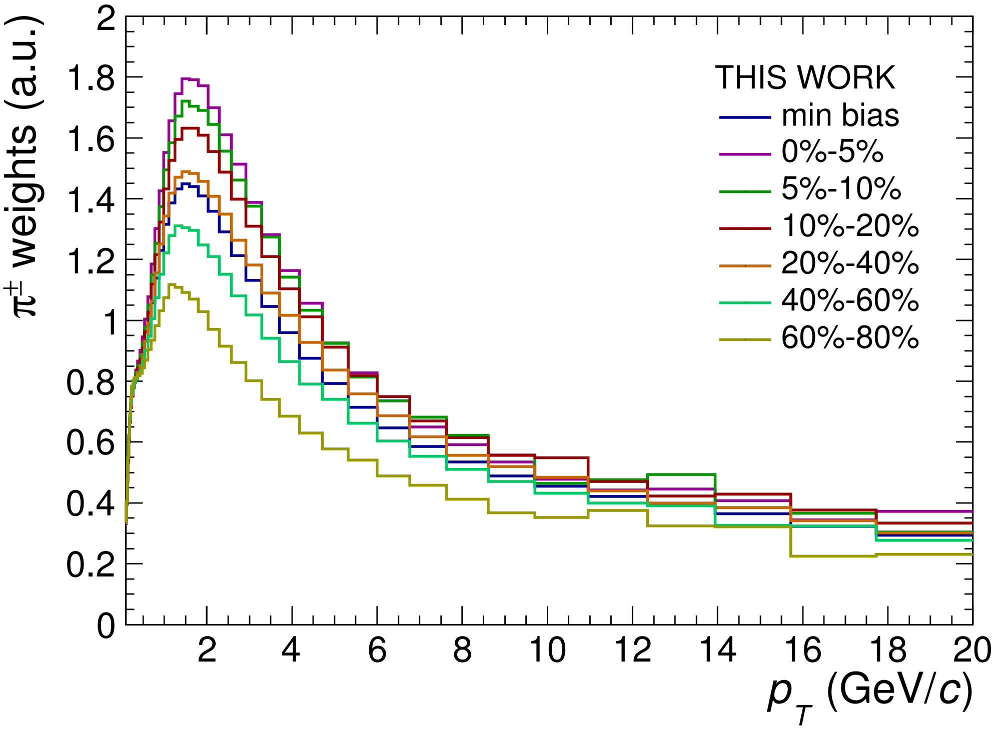

Figure 4.18: Monte Carlo tagging efficiency weights for pions for different centrality classes obtained by folding the default weight function with the functions shown in the bottom panel of Figure 4.17.

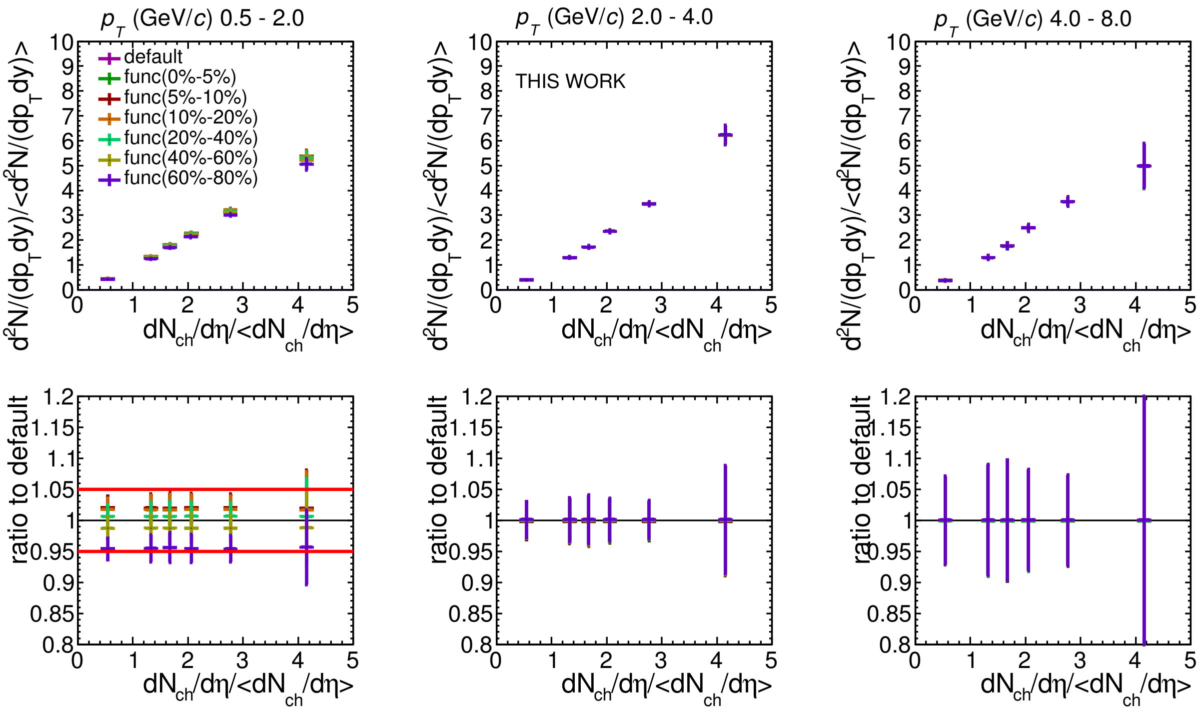

Figure 4.19: Self-normalized yields of electrons for different reweighting functions in three p_{T} intervals (top). Ratio between self-normalized yields with changed reweighting function and the self-normalized yield with the default reweighting function (bottom). The assigned systematic uncertainty of 5% is indicated with the red lines.

4.4 Results of the self-normalized yields as function of multiplicity

The self-normalized yields of electrons from heavy-flavor hadron decays as function of the charged-particle multiplicity are calculated as following:

$$\frac{\mathrm{d}^2N_\mathrm{i}^\mathrm{e}/\mathrm{d}p_\mathrm{T}\mathrm{d}y}{\langle \mathrm{d}^2N^\mathrm{e}/\mathrm{d}p_\mathrm{T}\mathrm{d}y\rangle} = \frac{N_\mathrm{raw,i}/N_\mathrm{events,i}}{N_\mathrm{raw}/N_\mathrm{events}} \tag{4.10}$$

with $N_\mathrm{raw,i}$ being the raw yield of electrons after subtraction of the photonic background in the multiplicity class "i" which is normalized to the number of events $N_\mathrm{events,i}$ in the same multiplicity class. These event normalized raw yields are divided by the multiplicity independent event normalized raw yields. In the previous section it was shown that the correction for the detector acceptance and tracking efficiency is independent of the multiplicity. Thus, the correction cancels in the ratio of 4.10. All other factors (p_T, Δy, Δp_T) in equation 3.13 of the inclusive analysis are also constant as function of multiplicity and cancel in the ratio.

4.4.1 Self normalized yields

The self-normalized yields of electrons from heavy-flavor hadron decays as function of the charged-particle multiplicity estimated at mid-rapidity is shown in Figure 4.20. The statistical uncertainties are shown as error bars and the systematic uncertainties as boxes. The values for the three different p_T intervals are compatible with each other within their uncertainties. They are also compatible with (at least) a linear increase as function of the multiplicity which is indicated as a dashed line in Figure 4.20. However, in the transverse momentum range $2 < p_\mathrm{T} < 4\,\mathrm{GeV}/c$ the uncertainties are small and a faster-than-linear increase for the self-normalized yield as a function of the charged-particle multiplicity is observed. The relative yield has a magnitude of approximately 5.5 for a relative average charged-particle multiplicity of 4.

In Figure 4.21 the self-normalized electron yields are shown as function of the relative multiplicity estimated at backward rapidity. The relative yields agree very well with a linear dependence as function of the multiplicity, which is indicated with a dashed line. The yields are compatible for all three p_T ranges.

The relative yields are increasing linearly with the multiplicity, independent on the rapidity in which the multiplicity was estimated. However, a trend for faster-than-linear increase is found for the self-normalized yields as function of the charged-particle multiplicity estimated at mid-rapidity. The results are in agreement with observations of faster-than-linear increase for the self-normalized yields of D mesons and J/ψ in pp collisions at $\sqrt{s} = 7\,\mathrm{TeV}$ by ALICE [118].

The study of the pseudo-rapidity dependence of the charged-particle multiplicity provides a possible explanation for the observed results. ALICE has measured the dependence of the charged-particle spectra on the multiplicity [116]. The multiplicity dependent spectra are scaling with the number of collisions N_coll in the multiplicity class when the multiplicity is estimated at backward rapidity (using the V0A signal). However, the multiplicity dependent spectra scale with the number of participants N_part when the multiplicity is estimated at mid-rapidity. This difference could influence the self-normalized yields from electrons of heavy-flavor hadron decays as function of the charged-particle multiplicity since the production of heavy-flavor is dependent on a hard scale and, thus, is scaling with N_coll. The faster-than-linear increase of the relative

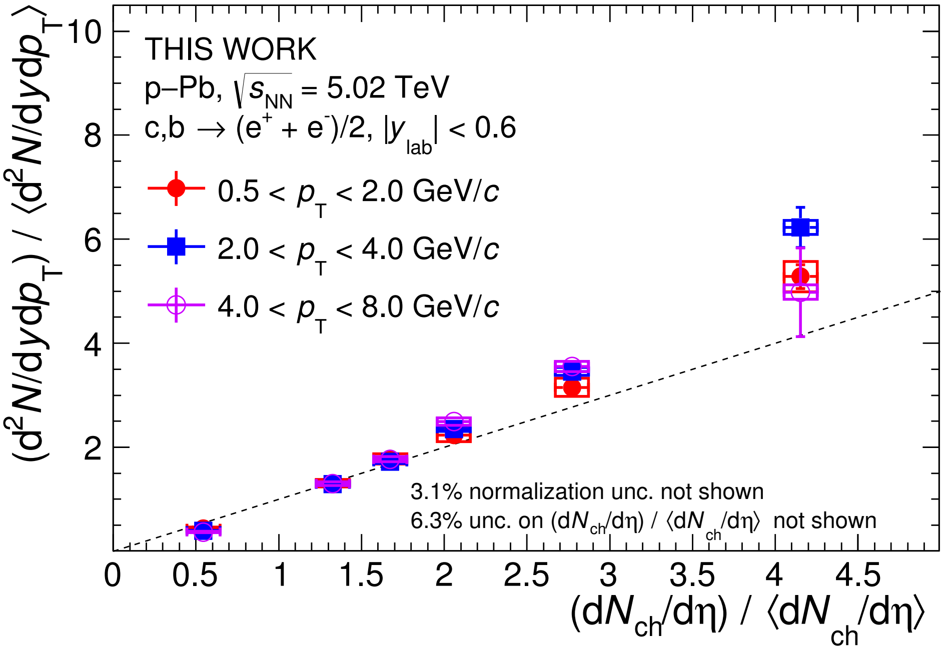

Figure 4.20: Self normalized yields of electrons from heavy-flavor hadron decays versus normalized charged-particle multiplicity using N_{tr} as mid-rapidity multiplicity estimator. The dashed line is shown to guide the eye (indicating a linear dependence)

heavy-flavor yields with respect to the charged-particle multiplicity estimated at mid-rapidity could be explained by the difference in scaling between the heavy-flavor part (N_{coll}) and the charged-particle part (N_{part}).

4.4.2 Comparison to D-meson results and EPOS calculations

The self-normalized yields of electrons from heavy-flavor hadron decays are compared to the results published by ALICE for the average self-normalized yields of D^+, D^0 and D^{*+} [76]. Since the electrons are coming from the decay of D mesons (and B mesons) and carrying only a small fraction of the momentum of the mother particle, their p_T-differential distribution is shifted on average to lower transverse momentum. To counter the bias of different kinematic ranges in the comparison of the self-normalized yields, the relative yields from the decay electrons are compared to relative yields from D mesons with approximately twice the average p_T. Figure 4.22 shows good agreement for all p_T intervals between the relative yields of decay electrons and D mesons. The measurement of relative yields of electrons from heavy-flavor hadron decays is thus a confirmation of the measurement of the relative yields of D mesons. The two measurement use independent methods of measuring heavy-flavor yields and their agreement give confidence in the respective measurement procedures.

The self-normalized yields for decay electrons and D mesons as function of the multiplicity estimated at backward rapidity show good agreement with each other as demonstrated in Figure 4.23. Both measurement show a linear increase as function of the relative charged-particle multiplicity.

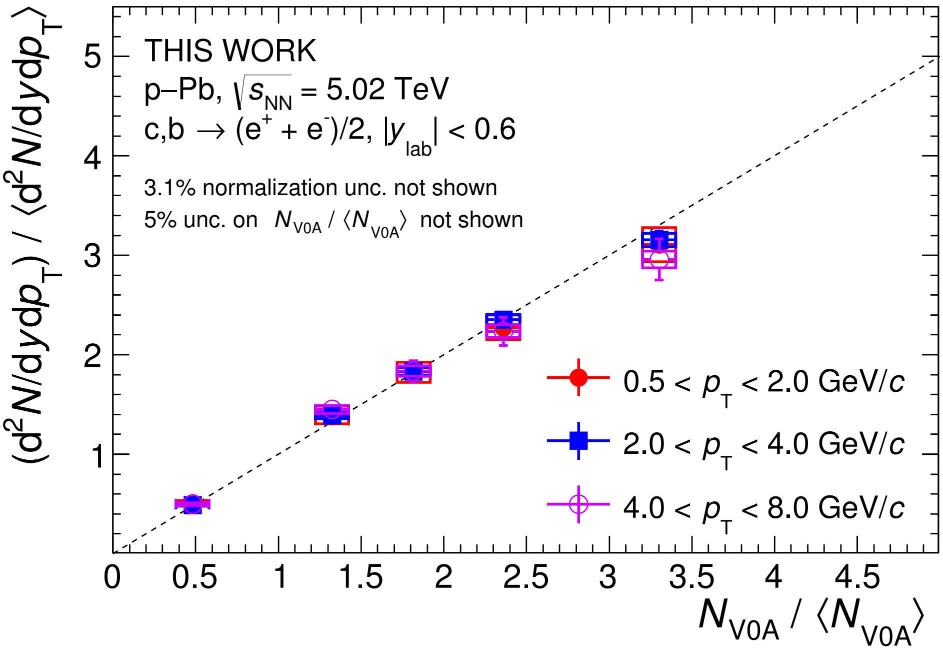

Figure 4.21: Self normalized yields of electrons from heavy-flavor hadron decays versus normalized charged-particle multiplicity using N_{V0A} as backward rapidity multiplicity estimator. The dashed line is shown to guide the eye (indicating a linear dependence)

The self-normalized yields in the Figures 4.22 and 4.23 are compared to calculations from the theoretical model EPOS 3 (version 3.116) [122, 126] for D mesons. The EPOS 3 model is designed to use the same theoretical framework for pp, p-A, and A-A collision systems. For the initial conditions a “Parton-based Gribov-Regge” formalism of multiple scatterings is used [126]. A hydrodynamical evolution is applied to the initial conditions of the simulated collisions [122].

For all p_T intervals the EPOS 3 model and the relative yields of D mesons agree within their uncertainties. The EPOS 3 model with hydrodynamical evolution predicts a faster-than-linear increase for the relative yields as function of multiplicity estimated at mid-rapidity (see Figure 4.22). The EPOS 3 model with hydrodynamical evolution agrees better with the measurements at high multiplicity than the model without hydrodynamical evolution. The EPOS 3 calculations with and without hydro agree with the relative yields as function of the multiplicity estimated at backward rapidity (Figure 4.23).

The better agreement observed for EPOS 3 with hydrodynamical expansion fits in the picture of a potential collective behavior in p-Pb collisions. In these measurements of long-range correlations of charged particles in azimuth, observed in the two-particle correlations, a “double-ridge” structure is observed [127]. The structure can be explained by hydrodynamic models which assume the formation of a collectively expanding system in the final state. An azimuthal anisotropy for heavy-flavor yields in A-A collisions has been measured by multiple experiments, consistent with the participation of charm quarks in the collective expansion of the QGP in A-A collisions (see Section 1.5 and references therein). Thus, the enhancement of the self-normalized yields of D mesons and electrons from heavy-flavor hadron decays as function of the charged-particle multiplicity estimated at mid-rapidity could be explained with the participation of heavy-flavor quarks in a collective expansion in p-Pb collisions. However, this interpretation

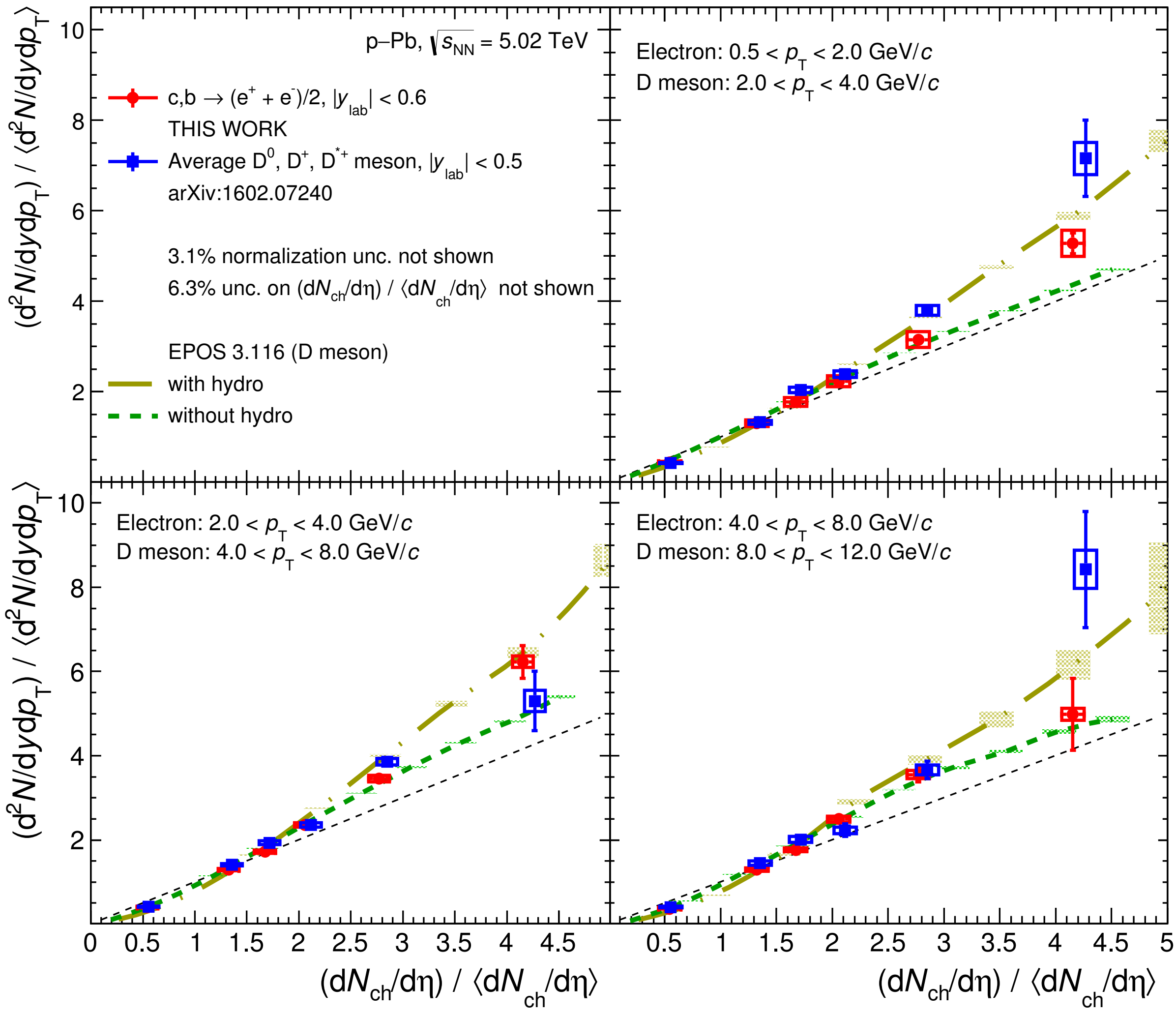

Figure 4.22: Comparison of the self-normalized yields of electrons from heavy-flavor hadron decays with those from the average of D^+, D^0 and D^{*+} mesons using $N_{\rm tr}$ mid-rapidity multiplicity estimator. Also comparisons to theoretical calculations with EPOS 3.116 including hydro [122, 126] are shown for D mesons.

is speculative and further measurements regarding collective behavior (of heavy-flavor) in p-Pb collisions are necessary for stronger conclusions.

4.4.3 Discussion

The yields of electrons from heavy-flavor hadron decays have a substantial contribution from semi-leptonic decays of beauty hadrons for $p_{\rm T} > 4\,\mathrm{GeV}/c$ (More than 50% according to [64]). The self-normalized yields show no dependence on the transverse momentum within their uncertainties. Although the self-normalized yield of electrons is reduced with respect to the self-normalized D-meson yields in the bottom-right panel of Figure 4.22, the statistical uncertainties are too large to be able to interpret the difference as a reduction for the self-normalized yields of electrons from heavy-flavor hadron decays. Thus, within the measured uncertainties no trend for a deviation for the multiplicity dependence of the self-normalized yield of electrons from

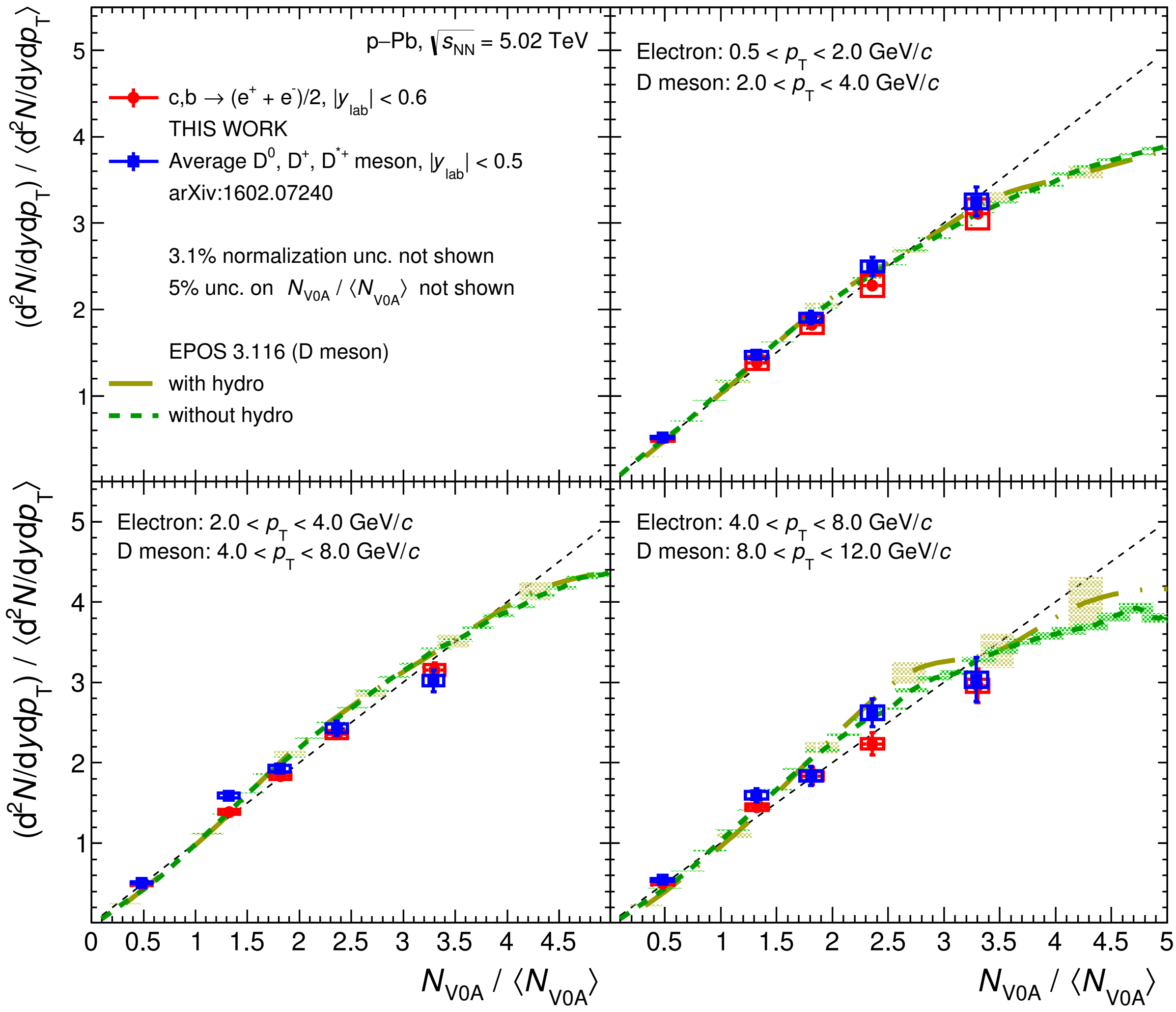

Figure 4.23: Comparison of the self-normalized yields of electrons from heavy-flavor hadron decays with those from the average of D^+, D^0 and D^{*+} mesons using N_{V0A} backward rapidity multiplicity estimator. Also comparisons to theoretical calculations with EPOS 3.116 including hydro [122, 126] are shown for D mesons.

beauty hadron decays is observed. The dependence on the beauty flavor was studied before only in pp collision via the self-normalized yields of non-prompt J/ψ's which are the decay product of beauty hadrons and discriminated statistically by their decay length [118]. Also in this measurement no significant dependence on the beauty flavor could be observed.

The analysis of the self-normalized yields of electrons as a function of the charged-particle multiplicity at mid-rapidity is limited by the available statistics. To improve uncertainties of the current measurement and be able to measure at higher values of multiplicity, more statistics is needed e.g. by using a trigger which selects high-multiplicity events.

5 Conclusion

In this work the first measurement of the cross section of electrons from heavy-flavor hadron decays in p-Pb collisions at $\sqrt{s_{\mathrm{NN}}} = 5.02\,\mathrm{TeV}$ with ALICE at the LHC is presented. For the first time in this type of measurement the electron background was estimated via the tagging of the photonic background instead of the calculation of a background cocktail, which was used in previous analyses with ALICE. The new method yields to a reduction of the systematic uncertainties of up to 80%, in particular at low p_{T}, compared to results in pp collisions at $\sqrt{s} = 7\,\mathrm{TeV}$. A reference production cross section for pp collisions at $\sqrt{s} = 5.02\,\mathrm{TeV}$ was determined by interpolation of measured cross sections at $\sqrt{s} = 2.76\,\mathrm{TeV}$ and $\sqrt{s} = 7\,\mathrm{TeV}$, assuming a power law function for the p_{T}-dependent cross sections as function of $\sqrt{s}$. The nuclear modification factor R_{pPb} was obtained dividing the cross section measured in p-Pb collisions by the interpolated cross section of the pp reference and scaled by the number of nucleons in a lead nucleus. R_{pPb} is found to be compatible with unity in the transverse-momentum range $0.5 < p_{\mathrm{T}} < 8\,\mathrm{GeV}/c$ within uncertainties, indicating that the production cross section of electrons from heavy-flavor hadron decays in p-Pb collisions scale with the number of binary nucleon-nucleon collisions. It can be concluded that CNM effects in measurements of electrons from heavy-flavor hadron decays measured in Pb-Pb collisions are small. Thus, the suppression seen in the yield of electrons and muons from heavy-flavor hadron decays in Pb-Pb collisions is the result of the energy-loss of charm and beauty quarks in the QGP medium formed.

The new method of background subtraction allowed to study the dependence of heavy-flavor production on the charged-particle multiplicity. The first measurement of self-normalized yields of electrons from heavy-flavor hadron decays as function of the charged-particle multiplicity is presented. The results indicate a linear dependence of the relative heavy-flavor yields as function of the relative multiplicity estimated at backward rapidity and at mid-rapidity. The data exhibit a scaling of the heavy-flavor production cross section with the charged-particle multiplicity which is proportional to the number of binary collisions in p-Pb collisions. The results are compatible with observations from a similar measurement of self-normalized D-meson yields. A p_{T}-dependence for the relative electron yields as function of multiplicity would give a hint for a different behavior for beauty production as function of multiplicity. However, within the uncertainties no change of the relative electron yields as function of p_{T} were observed, indicating a similar multiplicity dependence for beauty and charm production. The same conclusion was drawn from the measurement of the multiplicity dependence of non-prompt J/ψ with ALICE in pp collisions at $\sqrt{s} = 7\,\mathrm{TeV}$. This work presents the first observation of the same multiplicity dependence of charm and beauty production in p-Pb collisions at $\sqrt{s_{\mathrm{NN}}} = 5.02\,\mathrm{TeV}$, indicating similarity between the multiplicity dependence of heavy-flavor production in high-multiplicity pp collisions and p-Pb collisions.

Due to the substantial uncertainties on the nuclear modification factor an enhancement of the yield of electrons from heavy-flavor hadron decays in p-Pb collisions at $\sqrt{s_{\mathrm{NN}}} = 5.02\,\mathrm{TeV}$ cannot be excluded. R_{pPb} is compared to different theoretical model calculations applying various possible CNM effects. All models agree with the experimental data within the uncertainties. With the current measurement of R_{pPb} none of the models can be excluded, which is partly due to the fact, that differences between different model calculations are only seen at very low p_{T}, where the measurements are dominated by the systematic uncertainties. A large fraction of the uncertainties of the R_{pPb} measurement was identified to come from the reference, which is interpolated from results measured in pp collisions using the cocktail based background subtraction.

The multiplicity dependence of the relative electron yield is different in the two rapidity ranges in which the charged-particle multiplicity is estimated. The relative electron yield is in good agreement with a linear increase as function of the charged-particle multiplicity estimated at backward rapidity. The relative electron yield as function of the charged-particle multiplicity estimated at mid-rapidity shows a faster-than-linear increase in agreement with the results of the D-meson measurement. Results on the pseudo-rapidity dependence of the charged-particle multiplicity suggest different scaling behaviors at mid-rapidity and backward rapidity, which could explain the difference observed in the increase of the relative yields. Theoretical model calculations from EPOS 3 applying initial conditions and a viscous hydrodynamic expansion are in good agreement with the multiplicity dependence for D mesons. The model calculations including radial flow are in a better agreement with the D-meson measurement and are able to reproduce the faster-than-linear increase for the mid-rapidity multiplicity estimation and the linear increase for the backward rapidity multiplicity estimation. The difference is explained in EPOS by a reduced influence of flow on charged particle production at backward rapidity.

Possible improvements on the uncertainties of the nuclear modification factor were studied, leading to the conclusion that a new reference could reduce the current uncertainties. Under the assumption that the new method of estimating the electron background leads to similar uncertainties for the measurements in pp collisions as for the measurement in p-Pb collisions, a new interpolated reference was calculated. The possible improvements of the uncertainties of R_{pPb} are estimated, which would still be large compared to the small difference of the theoretical model calculations. Also a possible enhancement of the R_{pPb} would still be compatible with the calculated reduced uncertainties.

The measurements of the self-normalized yields of electrons from heavy-flavor hadron decays suffer from large statistical uncertainties in the highest multiplicity. To measure the faster-than-linear increase of the self-normalized yields as a function of the charged-particle multiplicity with smaller uncertainties, more statistics are needed. A measurement of events selected with a high-multiplicity trigger could improve the uncertainties significantly and further constrain model calculations from EPOS 3, which can reproduce the faster-than-linear increase by applying a viscous hydrodynamic evolution. In p-Pb collisions indications for collective behavior are observed, which might also influence heavy-flavor quark kinematics. However, it is still not clear if the observations in p-Pb collisions originate from a collective expansion or from effects predicted by Color Glass Condensate model calculations. Thus, further development on the understanding of the potential collectivity in p-Pb collisions is needed to make definite conclusions on the results of relative electron yields as function of charged-particle multiplicity.

Bibliography

[1] P. W. Higgs, “Broken Symmetries and the Masses of Gauge Bosons,” *Phys. Rev. Lett.* **13** (1964) 508–509.

[2] F. Englert and R. Brout, “Broken Symmetry and the Mass of Gauge Vector Mesons,” *Phys. Rev. Lett.* **13** (1964) 321–323.

[3] **ATLAS** Collaboration, G. Aad *et al.*, “Observation of a new particle in the search for the Standard Model Higgs boson with the ATLAS detector at the LHC,” *Phys. Lett.* **B716** (2012) 1–29, `arXiv:1207.7214 [hep-ex]`.

[4] **CMS** Collaboration, S. Chatrchyan *et al.*, “Observation of a new boson at a mass of 125 GeV with the CMS experiment at the LHC,” *Phys. Lett.* **B716** (2012) 30–61, `arXiv:1207.7235 [hep-ex]`.

[5] D. J. Gross and F. Wilczek, “Ultraviolet Behavior of Nonabelian Gauge Theories,” *Phys. Rev. Lett.* **30** (1973) 1343–1346.

[6] H. D. Politzer, “Reliable Perturbative Results for Strong Interactions?,” *Phys. Rev. Lett.* **30** (1973) 1346–1349.

[7] **Particle Data Group** Collaboration, K. A. Olive *et al.*, “Review of Particle Physics,” *Chin. Phys.* **C38** (2014) 090001.

[8] V. N. Gribov and L. N. Lipatov, “Deep inelastic e p scattering in perturbation theory,” *Sov. J. Nucl. Phys.* **15** (1972) 438–450. [Yad. Fiz.15,781(1972)].

[9] Y. L. Dokshitzer, “Calculation of the Structure Functions for Deep Inelastic Scattering and e+ e- Annihilation by Perturbation Theory in Quantum Chromodynamics.,” *Sov. Phys. JETP* **46** (1977) 641–653. [Zh. Eksp. Teor. Fiz.73,1216(1977)].

[10] G. Altarelli and G. Parisi, “Asymptotic Freedom in Parton Language,” *Nucl. Phys.* **B126** (1977) 298–318.

[11] S. Godfrey and S. L. Olsen, “The Exotic XYZ Charmonium-like Mesons,” *Ann. Rev. Nucl. Part. Sci.* **58** (2008) 51–73, `arXiv:0801.3867 [hep-ph]`.

[12] **LHCb** Collaboration, R. Aaij *et al.*, “Observation of $J/\psi p$ Resonances Consistent with Pentaquark States in $\Lambda_b^0 \to J/\psi K^- p$ Decays,” *Phys. Rev. Lett.* **115** (2015) 072001, `arXiv:1507.03414 [hep-ex]`.

[13] E. Eichten, K. Gottfried, T. Kinoshita, J. B. Kogut, K. D. Lane, and T.-M. Yan, “The Spectrum of Charmonium,” *Phys. Rev. Lett.* **34** (1975) 369–372. [Erratum: Phys. Rev. Lett.36,1276(1976)].

[14] S. Borsanyi, Z. Fodor, C. Hoelbling, S. D. Katz, S. Krieg, and K. K. Szabo, “Full result for the QCD equation of state with 2+1 flavors,” *Phys. Lett.* **B730** (2014) 99–104, `arXiv:1309.5258 [hep-lat]`.

[15] J. D. Bjorken, "Highly Relativistic Nucleus-Nucleus Collisions: The Central Rapidity Region," *Phys. Rev.* **D27** (1983) 140–151.

[16] Y. Aoki, G. Endrodi, Z. Fodor, S. D. Katz, and K. K. Szabo, "The Order of the quantum chromodynamics transition predicted by the standard model of particle physics," *Nature* **443** (2006) 675–678, `arXiv:hep-lat/0611014 [hep-lat]`.

[17] Z. Fodor and S. D. Katz, "Lattice determination of the critical point of QCD at finite T and mu," *JHEP* **03** (2002) 014, `arXiv:hep-lat/0106002 [hep-lat]`.

[18] F. Karsch and E. Laermann, "Thermodynamics and in medium hadron properties from lattice QCD," `arXiv:hep-lat/0305025 [hep-lat]`.

[19] F. Karsch, "Lattice QCD at high temperature and density," *Lect. Notes Phys.* **583** (2002) 209–249, `arXiv:hep-lat/0106019 [hep-lat]`.

[20] **HotQCD** Collaboration, A. Bazavov *et al.*, "Equation of state in (2+1)-flavor QCD," *Phys. Rev.* **D90** (2014) 094503, `arXiv:1407.6387 [hep-lat]`.

[21] **HotQCD** Collaboration, A. Bazavov *et al.*, "Fluctuations and Correlations of net baryon number, electric charge, and strangeness: A comparison of lattice QCD results with the hadron resonance gas model," *Phys. Rev.* **D86** (2012) 034509, `arXiv:1203.0784 [hep-lat]`.

[22] U. W. Heinz and M. Jacob, "Evidence for a new state of matter: An Assessment of the results from the CERN lead beam program," `arXiv:nucl-th/0002042 [nucl-th]`.

[23] **STAR** Collaboration, J. Adams *et al.*, "Experimental and theoretical challenges in the search for the quark gluon plasma: The STAR Collaboration's critical assessment of the evidence from RHIC collisions," *Nucl. Phys.* **A757** (2005) 102–183, `arXiv:nucl-ex/0501009 [nucl-ex]`.

[24] **ALICE** Collaboration, K. Aamodt *et al.*, "Elliptic flow of charged particles in Pb-Pb collisions at 2.76 TeV," *Phys. Rev. Lett.* **105** (2010) 252302, `arXiv:1011.3914 [nucl-ex]`.

[25] M. L. Miller, K. Reygers, S. J. Sanders, and P. Steinberg, "Glauber modeling in high energy nuclear collisions," *Ann. Rev. Nucl. Part. Sci.* **57** (2007) 205–243, `arXiv:nucl-ex/0701025 [nucl-ex]`.

[26] B. Alver, M. Baker, C. Loizides, and P. Steinberg, "The PHOBOS Glauber Monte Carlo," `arXiv:0805.4411 [nucl-ex]`.

[27] R. D. Woods and D. S. Saxon, "Diffuse Surface Optical Model for Nucleon-Nuclei Scattering," *Phys. Rev.* **95** (1954) 577–578.

[28] F.-M. Liu and S.-X. Liu, "Quark-gluon plasma formation time and direct photons from heavy ion collisions," *Phys. Rev.* **C89** no. 3, (2014) 034906, `arXiv:1212.6587 [nucl-th]`.

[29] **ALICE** Collaboration, B. Abelev *et al.*, "Pion, Kaon, and Proton Production in Central Pb–Pb Collisions at $\sqrt{s_{NN}} = 2.76$ TeV," *Phys. Rev. Lett.* **109** (2012) 252301, `arXiv:1208.1974 [hep-ex]`.

[30] M. Luzum and P. Romatschke, “Conformal Relativistic Viscous Hydrodynamics: Applications to RHIC results at s(NN)**(1/2) = 200-GeV,” *Phys. Rev.* **C78** (2008) 034915, `arXiv:0804.4015 [nucl-th]`. [Erratum: Phys. Rev.C79,039903(2009)].

[31] J. C. Collins, D. E. Soper, and G. F. Sterman, “Factorization of Hard Processes in QCD,” *Adv. Ser. Direct. High Energy Phys.* **5** (1989) 1–91, `arXiv:hep-ph/0409313 [hep-ph]`.

[32] **TASSO** Collaboration, R. Brandelik *et al.*, “Evidence for Planar Events in e+ e- Annihilation at High-Energies,” *Phys. Lett.* **B86** (1979) 243–249.

[33] **ALICE** Collaboration, B. B. Abelev *et al.*, “Transverse momentum dependence of inclusive primary charged-particle production in p-Pb collisions at $\sqrt{s_{\rm NN}} = 5.02$ TeV,” *Eur. Phys. J.* **C74** no. 9, (2014) 3054, `arXiv:1405.2737 [nucl-ex]`.

[34] K. J. Eskola, H. Paukkunen, and C. A. Salgado, “EPS09: A New Generation of NLO and LO Nuclear Parton Distribution Functions,” *JHEP* **04** (2009) 065, `arXiv:0902.4154 [hep-ph]`.

[35] K. Rith, “Present Status of the EMC effect,” *Subnucl. Ser.* **51** (2015) 431–449, `arXiv:1402.5000 [hep-ex]`.

[36] J. L. Albacete and C. Marquet, “Gluon saturation and initial conditions for relativistic heavy ion collisions,” *Prog. Part. Nucl. Phys.* **76** (2014) 1–42, `arXiv:1401.4866 [hep-ph]`.

[37] J. W. Cronin, H. J. Frisch, M. J. Shochet, J. P. Boymond, R. Mermod, P. A. Piroue, and R. L. Sumner, “Production of Hadrons with Large Transverse Momentum at 200-GeV, 300-GeV, and 400-GeV,” *Phys. Rev.* **D11** (1975) 3105.

[38] R. Sharma, I. Vitev, and B.-W. Zhang, “Light-cone wave function approach to open heavy flavor dynamics in QCD matter,” *Phys. Rev.* **C80** (2009) 054902, `arXiv:0904.0032 [hep-ph]`.

[39] Z.-B. Kang, I. Vitev, E. Wang, H. Xing, and C. Zhang, “Multiple scattering effects on heavy meson production in p+A collisions at backward rapidity,” *Phys. Lett.* **B740** (2015) 23–29, `arXiv:1409.2494 [hep-ph]`.

[40] T. Matsui and H. Satz, “J/ψ Suppression by Quark-Gluon Plasma Formation,” *Phys. Lett.* **B178** (1986) 416–422.

[41] **NA50** Collaboration, M. C. Abreu *et al.*, “The Dependence of the anomalous J/ψ suppression on the number of participant nucleons,” *Phys. Lett.* **B521** (2001) 195–203.

[42] A. Capella, A. B. Kaidalov, and D. Sousa, “Why is the J/ψ suppression enhanced at large transverse energy?,” *Phys. Rev.* **C65** (2002) 054908, `arXiv:nucl-th/0105021 [nucl-th]`.

[43] R. L. Thews, M. Schroedter, and J. Rafelski, “Enhanced J/ψ production in deconfined quark matter,” *Phys. Rev.* **C63** (2001) 054905, `arXiv:hep-ph/0007323 [hep-ph]`.

[44] A. Andronic, P. Braun-Munzinger, K. Redlich, and J. Stachel, “Statistical hadronization of heavy quarks in ultra-relativistic nucleus-nucleus collisions,” *Nucl. Phys.* **A789** (2007) 334–356, `arXiv:nucl-th/0611023 [nucl-th]`.

[45] R. Rapp, D. Blaschke, and P. Crochet, “Charmonium and bottomonium production in heavy-ion collisions,” *Prog. Part. Nucl. Phys.* **65** (2010) 209–266, `arXiv:0807.2470 [hep-ph]`.

[46] M. Cacciari, M. Greco, and P. Nason, “The P(T) spectrum in heavy flavor hadroproduction,” *JHEP* **05** (1998) 007, `arXiv:hep-ph/9803400 [hep-ph]`.

[47] M. Cacciari, S. Frixione, and P. Nason, “The p(T) spectrum in heavy flavor photoproduction,” *JHEP* **03** (2001) 006, `arXiv:hep-ph/0102134 [hep-ph]`.

[48] M. Cacciari, S. Frixione, N. Houdeau, M. L. Mangano, P. Nason, and G. Ridolfi, “Theoretical predictions for charm and bottom production at the LHC,” *JHEP* **10** (2012) 137, `arXiv:1205.6344 [hep-ph]`.

[49] B. A. Kniehl, G. Kramer, I. Schienbein, and H. Spiesberger, “Reconciling open charm production at the Fermilab Tevatron with QCD,” *Phys. Rev. Lett.* **96** (2006) 012001, `arXiv:hep-ph/0508129 [hep-ph]`.

[50] E. Braaten and M. H. Thoma, “Energy loss of a heavy fermion in a hot plasma,” *Phys. Rev.* **D44** (1991) 1298–1310.

[51] Y. L. Dokshitzer and D. E. Kharzeev, “Heavy quark colorimetry of QCD matter,” *Phys. Lett.* **B519** (2001) 199–206, `arXiv:hep-ph/0106202 [hep-ph]`.

[52] R. Baier, Y. L. Dokshitzer, A. H. Mueller, S. Peigne, and D. Schiff, “Radiative energy loss of high-energy quarks and gluons in a finite volume quark - gluon plasma,” *Nucl. Phys.* **B483** (1997) 291–320, `arXiv:hep-ph/9607355 [hep-ph]`.

[53] M. G. Mustafa, “Energy loss of charm quarks in the quark-gluon plasma: Collisional versus radiative,” *Phys. Rev.* **C72** (2005) 014905, `arXiv:hep-ph/0412402 [hep-ph]`.

[54] S. Wicks, W. Horowitz, M. Djordjevic, and M. Gyulassy, “Heavy quark jet quenching with collisional plus radiative energy loss and path length fluctuations,” *Nucl. Phys.* **A783** (2007) 493–496, `arXiv:nucl-th/0701063 [nucl-th]`.

[55] **PHENIX** Collaboration, A. Adare *et al.*, “Energy Loss and Flow of Heavy Quarks in Au+Au Collisions at s(NN)**(1/2) = 200-GeV,” *Phys. Rev. Lett.* **98** (2007) 172301, `arXiv:nucl-ex/0611018 [nucl-ex]`.

[56] N. Armesto, M. Cacciari, A. Dainese, C. A. Salgado, and U. A. Wiedemann, “How sensitive are high-p(T) electron spectra at RHIC to heavy quark energy loss?,” *Phys. Lett.* **B637** (2006) 362–366, `arXiv:hep-ph/0511257 [hep-ph]`.

[57] H. van Hees, V. Greco, and R. Rapp, “Heavy-quark probes of the quark-gluon plasma at RHIC,” *Phys. Rev.* **C73** (2006) 034913, `arXiv:nucl-th/0508055 [nucl-th]`.

[58] G. D. Moore and D. Teaney, “How much do heavy quarks thermalize in a heavy ion collision?,” *Phys. Rev.* **C71** (2005) 064904, `arXiv:hep-ph/0412346 [hep-ph]`.

[59] **ALICE** Collaboration, J. Adam *et al.*, “Centrality dependence of high-$p_{\rm T}$ D meson suppression in Pb-Pb collisions at $\sqrt{s_{\rm NN}}$ = 2.76 TeV,” `arXiv:1506.06604 [nucl-ex]`.

[60] **CMS Collaboration** Collaboration, "J/ψ results from CMS in PbPb collisions, with 150mub-1 data," Tech. Rep. CMS-PAS-HIN-12-014, CERN, Geneva, 2012. `https://cds.cern.ch/record/1472735`.

[61] M. Djordjevic, M. Djordjevic, and B. Blagojevic, "RHIC and LHC jet suppression in non-central collisions," *Phys. Lett.* **B737** (2014) 298–302, `arXiv:1405.4250 [nucl-th]`.

[62] **ALICE** Collaboration, J. Adam *et al.*, "D-meson production in p-Pb collisions at $\sqrt{s_{\rm NN}} = 5.02\,$TeV TeV and in pp collisions at $\sqrt{s} = 7$ TeV," `arXiv:1605.07569 [nucl-ex]`.

[63] **ALICE** Collaboration, B. B. Abelev *et al.*, "Beauty production in pp collisions at $\sqrt{s} =$ 2.76 TeV measured via semi-electronic decays," *Phys. Lett.* **B738** (2014) 97–108, `arXiv:1405.4144 [nucl-ex]`.

[64] **ALICE** Collaboration, B. Abelev *et al.*, "Measurement of electrons from beauty hadron decays in pp collisions at $\sqrt{s} = 7$ TeV," *Phys. Lett.* **B721** (2013) 13–23, `arXiv:1208.1902 [hep-ex]`.

[65] **PHENIX** Collaboration, S. S. Adler *et al.*, "Single electrons from heavy flavor decays in p+p collisions at s**(1/2) = 200-GeV," *Phys. Rev. Lett.* **96** (2006) 032001, `arXiv:hep-ex/0508034 [hep-ex]`.

[66] **PHENIX** Collaboration, A. Adare *et al.*, "Measurement of high-p(T) single electrons from heavy-flavor decays in p+p collisions at s**(1/2) = 200-GeV," *Phys. Rev. Lett.* **97** (2006) 252002, `arXiv:hep-ex/0609010 [hep-ex]`.

[67] **STAR** Collaboration, H. Agakishiev *et al.*, "High $p_{\rm T}$ non-photonic electron production in $p + p$ collisions at $\sqrt{s} = 200$ GeV," *Phys. Rev.* **D83** (2011) 052006, `arXiv:1102.2611 [nucl-ex]`.

[68] **STAR** Collaboration, B. I. Abelev *et al.*, "Transverse momentum and centrality dependence of high-p_T non-photonic electron suppression in Au+Au collisions at $\sqrt{s_{NN}} = 200\,$GeV," *Phys. Rev. Lett.* **98** (2007) 192301, `arXiv:nucl-ex/0607012 [nucl-ex]`. [Erratum: Phys. Rev. Lett.106,159902(2011)].

[69] **ALICE** Collaboration, J. Adam *et al.*, "Measurement of electrons from heavy-flavour hadron decays in p-Pb collisions at $\sqrt{s_{\rm NN}} = 5.02$ TeV," *Phys. Lett.* **B754** (2016) 81–93, `arXiv:1509.07491 [nucl-ex]`.

[70] **CMS** Collaboration, S. Chatrchyan *et al.*, "Jet and underlying event properties as a function of charged-particle multiplicity in proton–proton collisions at $\sqrt{s} = 7$ TeV," *Eur. Phys. J.* **C73** no. 12, (2013) 2674, `arXiv:1310.4554 [hep-ex]`.

[71] **ALICE** Collaboration, B. Abelev *et al.*, "Underlying Event measurements in pp collisions at $\sqrt{s} = 0.9$ and 7 TeV with the ALICE experiment at the LHC," *JHEP* **07** (2012) 116, `arXiv:1112.2082 [hep-ex]`.

[72] **ATLAS** Collaboration, G. Aad *et al.*, "Observation of Associated Near-Side and Away-Side Long-Range Correlations in $\sqrt{s_{NN}} = 5.02$ TeV Proton-Lead Collisions with the ATLAS Detector," *Phys. Rev. Lett.* **110** no. 18, (2013) 182302, `arXiv:1212.5198 [hep-ex]`.

[73] **ALICE** Collaboration, K. Aamodt *et al.*, “Harmonic decomposition of two-particle angular correlations in Pb-Pb collisions at $\sqrt{s_{NN}} = 2.76$ TeV,” *Phys. Lett.* **B708** (2012) 249–264, `arXiv:1109.2501 [nucl-ex]`.

[74] K. Dusling and R. Venugopalan, “Comparison of the color glass condensate to dihadron correlations in proton-proton and proton-nucleus collisions,” *Phys. Rev.* **D87** no. 9, (2013) 094034, `arXiv:1302.7018 [hep-ph]`.

[75] **ALICE** Collaboration, B. B. Abelev *et al.*, “Multiplicity Dependence of Pion, Kaon, Proton and Lambda Production in p-Pb Collisions at $\sqrt{s_{NN}} = 5.02$ TeV,” *Phys. Lett.* **B728** (2014) 25–38, `arXiv:1307.6796 [nucl-ex]`.

[76] **ALICE** Collaboration, J. Adam *et al.*, “Measurement of D-meson production versus multiplicity in p-Pb collisions at $\sqrt{s_{NN}} = 5.02$ TeV,” `arXiv:1602.07240 [nucl-ex]`.

[77] O. S. Brüning, P. Collier, P. Lebrun, S. Myers, R. Ostojic, J. Poole, and P. Proudlock, *LHC Design Report*. CERN, Geneva, 2004. `https://cds.cern.ch/record/782076`.

[78] O. S. Brüning, P. Collier, P. Lebrun, S. Myers, R. Ostojic, J. Poole, and P. Proudlock, *LHC Design Report*. CERN, Geneva, 2004. `https://cds.cern.ch/record/815187`.

[79] M. Benedikt, P. Collier, V. Mertens, J. Poole, and K. Schindl, *LHC Design Report*. CERN, Geneva, 2004. `https://cds.cern.ch/record/823808`.

[80] L. Evans and P. Bryant, “LHC Machine,” *JINST* **3** (2008) S08001.

[81] Wikimedia Commons, “Map of the CERN accelerator complex,” 2011. `https://commons.wikimedia.org/wiki/File:Cern-accelerator-complex.svg`.

[82] **ATLAS** Collaboration, G. Aad *et al.*, “The ATLAS Experiment at the CERN Large Hadron Collider,” *JINST* **3** (2008) S08003.

[83] **CMS** Collaboration, S. Chatrchyan *et al.*, “The CMS experiment at the CERN LHC,” *JINST* **3** (2008) S08004.

[84] **TOTEM** Collaboration, G. Anelli *et al.*, “The TOTEM experiment at the CERN Large Hadron Collider,” *JINST* **3** (2008) S08007.

[85] **LHCf** Collaboration, O. Adriani *et al.*, “The LHCf detector at the CERN Large Hadron Collider,” *JINST* **3** (2008) S08006.

[86] **ALICE** Collaboration, P. Cortese *et al.*, “ALICE: Physics performance report, volume I,” *J. Phys.* **G30** (2004) 1517–1763.

[87] **ALICE** Collaboration, K. Aamodt *et al.*, “The ALICE experiment at the CERN LHC,” *JINST* **3** (2008) S08002.

[88] **ALICE** Collaboration, E. Abbas *et al.*, “Centrality dependence of the pseudorapidity density distribution for charged particles in Pb-Pb collisions at $\sqrt{s_{\mathrm{NN}}} = 2.76$ TeV,” *Phys. Lett.* **B726** (2013) 610–622, `arXiv:1304.0347 [nucl-ex]`.

[89] **ALICE** Collaboration, B. B. Abelev *et al.*, “Performance of the ALICE Experiment at the CERN LHC,” *Int. J. Mod. Phys.* **A29** (2014) 1430044, `arXiv:1402.4476 [nucl-ex]`.

[90] R. Fruhwirth, “Application of Kalman filtering to track and vertex fitting,” *Nucl. Instrum. Meth.* **A262** (1987) 444–450.

[91] M. Gyulassy and X.-N. Wang, “HIJING 1.0: A Monte Carlo program for parton and particle production in high-energy hadronic and nuclear collisions,” *Comput. Phys. Commun.* **83** (1994) 307, `arXiv:nucl-th/9502021 [nucl-th]`.

[92] R. Brun *et al.*, *GEANT: Detector Description and Simulation Tool; Oct 1994*. CERN Program Library. CERN, Geneva, 1993. `http://cds.cern.ch/record/1082634`. Long Writeup W5013.

[93] T. Sjostrand, S. Mrenna, and P. Z. Skands, “PYTHIA 6.4 Physics and Manual,” *JHEP* **05** (2006) 026, `arXiv:hep-ph/0603175 [hep-ph]`.

[94] P. Z. Skands, “Tuning Monte Carlo Generators: The Perugia Tunes,” *Phys. Rev.* **D82** (2010) 074018, `arXiv:1005.3457 [hep-ph]`.

[95] C. Lippmann, “Particle identification,” *Nucl. Instrum. Meth.* **A666** (2012) 148–172, `arXiv:1101.3276 [hep-ex]`.

[96] **ALICE** Collaboration, B. Abelev *et al.*, “Measurement of electrons from semileptonic heavy-flavour hadron decays in pp collisions at $\sqrt{s} = 7$ TeV,” *Phys. Rev.* **D86** (2012) 112007, `arXiv:1205.5423 [hep-ex]`.

[97] **PHENIX** Collaboration, A. Adare *et al.*, “Cold-nuclear-matter effects on heavy-quark production in d+Au collisions at $\sqrt{s_{NN}} = 200$ GeV,” *Phys. Rev. Lett.* **109** no. 24, (2012) 242301, `arXiv:1208.1293 [nucl-ex]`.

[98] **ALICE** Collaboration, B. B. Abelev *et al.*, “Measurement of electrons from semileptonic heavy-flavor hadron decays in pp collisions at $\sqrt{s} = 2.76$ TeV,” *Phys. Rev.* **D91** no. 1, (2015) 012001, `arXiv:1405.4117 [nucl-ex]`.

[99] **ALICE** Collaboration, J. Adam *et al.*, “Multiplicity dependence of charged pion, kaon, and (anti)proton production at large transverse momentum in p-Pb collisions at $\sqrt{s_{\mathrm{NN}}} = 5.02$ TeV,” `arXiv:1601.03658 [nucl-ex]`.

[100] C. Tsallis, “Possible Generalization of Boltzmann-Gibbs Statistics,” *J. Statist. Phys.* **52** (1988) 479–487.

[101] E. L. Bratkovskaya, W. Cassing, and U. Mosel, “Meson m(T) - scaling in heavy ion collisions at SIS energies,” *Phys. Lett.* **B424** (1998) 244–252, `arXiv:nucl-th/9712046 [nucl-th]`.

[102] P. K. Khandai, P. Shukla, and V. Singh, “Meson spectra and m_T scaling in $p + p$, d+Au, and Au + Au collisions at $\sqrt{s_{NN}} = 200$ GeV,” *Phys. Rev.* **C84** (2011) 054904, `arXiv:1110.3929 [hep-ph]`.

[103] F. Bossu, Z. C. del Valle, A. de Falco, M. Gagliardi, S. Grigoryan, and G. Martinez Garcia, “Phenomenological interpolation of the inclusive J/ψ cross section to proton-proton collisions at 2.76 TeV and 5.5 TeV,” `arXiv:1103.2394 [nucl-ex]`.

[104] **ALICE** Collaboration, J. Adam *et al.*, "Rapidity and transverse-momentum dependence of the inclusive J/ψ nuclear modification factor in p-Pb collisions at $\sqrt{s_{\rm NN}} = 5.02$ TeV," *JHEP* **06** (2015) 055, `arXiv:1503.07179 [nucl-ex]`.

[105] **ALICE** Collaboration, M. K. Koehler, "Dielectron measurements in pp, p-Pb and Pb-Pb collisions with ALICE at the LHC," *Nucl. Phys.* **A931** (2014) 665–669, `arXiv:1407.7809 [nucl-ex]`.

[106] G. D'Agostini, *Bayesian reasoning in high-energy physics: principles and applications*. CERN, Geneva, 1999. `http://cds.cern.ch/record/395902`.

[107] J. F. Grosse-Oetringhaus, *Measurement of the Charged-Particle Multiplicity in Proton-Proton Collisions with the ALICE Detector*. PhD thesis, Münster U., 2009. `https://inspirehep.net/record/887184/files/CERN-THESIS-2009-033.pdf`.

[108] R. Barlow, "Systematic errors: Facts and fictions," in *Advanced Statistical Techniques in Particle Physics. Proceedings, Conference, Durham, UK, March 18-22, 2002*, pp. 134–144. 2002. `arXiv:hep-ex/0207026 [hep-ex]`. `http://www.ippp.dur.ac.uk/Workshops/02/statistics/proceedings//barlow.pdf`.

[109] **ATLAS** Collaboration, G. Aad *et al.*, "Measurements of the electron and muon inclusive cross-sections in proton-proton collisions at $\sqrt{s} = 7$ TeV with the ATLAS detector," *Phys. Lett.* **B707** (2012) 438–458, `arXiv:1109.0525 [hep-ex]`.

[110] **ALICE** Collaboration, B. Abelev *et al.*, "Measurement of charm production at central rapidity in proton-proton collisions at $\sqrt{s} = 2.76$ TeV," *JHEP* **07** (2012) 191, `arXiv:1205.4007 [hep-ex]`.

[111] **ALICE** Collaboration, B. B. Abelev *et al.*, "Measurement of visible cross sections in proton-lead collisions at $\sqrt{s_{\rm NN}}$ = 5.02 TeV in van der Meer scans with the ALICE detector," *JINST* **9** no. 11, (2014) P11003, `arXiv:1405.1849 [nucl-ex]`.

[112] **ALICE** Collaboration, B. Abelev *et al.*, "Production of muons from heavy flavour decays at forward rapidity in pp and Pb-Pb collisions at $\sqrt{s_{NN}}$ = 2.76 TeV," *Phys. Rev. Lett.* **109** (2012) 112301, `arXiv:1205.6443 [hep-ex]`.

[113] A. M. Sickles, "Possible Evidence for Radial Flow of Heavy Mesons in d+Au Collisions," *Phys. Lett.* **B731** (2014) 51–56, `arXiv:1309.6924 [nucl-th]`.

[114] S. Sakai. Private communication, June, 2015.

[115] I. Vitev. Private communication, May, 2015.

[116] **ALICE** Collaboration, J. Adam *et al.*, "Centrality dependence of particle production in p-Pb collisions at $\sqrt{s_{\rm NN}}$= 5.02 TeV," *Phys. Rev.* **C91** no. 6, (2015) 064905, `arXiv:1412.6828 [nucl-ex]`.

[117] **ALICE** Collaboration, B. Abelev *et al.*, "J/ψ Production as a Function of Charged Particle Multiplicity in *pp* Collisions at $\sqrt{s} = 7$ TeV," *Phys. Lett.* **B712** (2012) 165–175, `arXiv:1202.2816 [hep-ex]`.

[118] **ALICE** Collaboration, J. Adam *et al.*, “Measurement of charm and beauty production at central rapidity versus charged-particle multiplicity in proton-proton collisions at $\sqrt{s} = 7$ TeV,” *JHEP* **09** (2015) 148, `arXiv:1505.00664 [nucl-ex]`.

[119] T. Sjostrand and M. van Zijl, “A Multiple Interaction Model for the Event Structure in Hadron Collisions,” *Phys. Rev.* **D36** (1987) 2019.

[120] T. Sjostrand, S. Mrenna, and P. Z. Skands, “A Brief Introduction to PYTHIA 8.1,” *Comput. Phys. Commun.* **178** (2008) 852–867, `arXiv:0710.3820 [hep-ph]`.

[121] E. G. Ferreiro and C. Pajares, “High multiplicity pp events and J/ψ production at LHC,” *Phys. Rev.* **C86** (2012) 034903, `arXiv:1203.5936 [hep-ph]`.

[122] K. Werner, B. Guiot, I. Karpenko, and T. Pierog, “Analysing radial flow features in p-Pb and p-p collisions at several TeV by studying identified particle production in EPOS3,” *Phys. Rev.* **C89** no. 6, (2014) 064903, `arXiv:1312.1233 [nucl-th]`.

[123] **ALICE** Collaboration, B. Abelev *et al.*, “Pseudorapidity density of charged particles in p + Pb collisions at $\sqrt{s_{NN}} = 5.02$ TeV,” *Phys. Rev. Lett.* **110** no. 3, (2013) 032301, `arXiv:1210.3615 [nucl-ex]`.

[124] S. Roesler, R. Engel, and J. Ranft, “The Monte Carlo event generator DPMJET-III,” in *Advanced Monte Carlo for radiation physics, particle transport simulation and applications. Proceedings, Conference, MC2000, Lisbon, Portugal, October 23-26, 2000*, pp. 1033–1038. 2000. `arXiv:hep-ph/0012252 [hep-ph]`. `http://www-public.slac.stanford.edu/sciDoc/docMeta.aspx?slacPubNumber=SLAC-PUB-8740`.

[125] G. Bencedi. Private communication, April, 2016.

[126] H. J. Drescher, M. Hladik, S. Ostapchenko, T. Pierog, and K. Werner, “Parton based Gribov-Regge theory,” *Phys. Rept.* **350** (2001) 93–289, `arXiv:hep-ph/0007198 [hep-ph]`.

[127] **ALICE** Collaboration, B. Abelev *et al.*, “Long-range angular correlations on the near and away side in p-Pb collisions at $\sqrt{s_{NN}} = 5.02$ TeV,” *Phys. Lett.* **B719** (2013) 29–41, `arXiv:1212.2001 [nucl-ex]`.

Acknowledgments

I would like to thank Prof. Peter Braun-Munzinger for giving me the opportunity to participate and do a PhD on LHC physics and supporting me together with Tetyana in the background the whole time.
My highest appreciation and gratefulness goes to Silvia and Ralf, who have been a tremendous support during all those years. Ralf, thank you for being solid as a rock during stressful times and your infinite patience. Silvia, thank you for your endless energy and support, for pushing me forward the whole time.
A big shout-out to the ALICE group at GSI. I feel very lucky having been member of this particular group. I am very thankful for the warm and welcoming atmosphere, the lovely excursions and annual events, and plentiful discussions during lunch or coffee breaks on physics and non-physics topics with all members of the group. Thank you all for the nice time!
Andrea, Anton, Benjamin, Jochen, Kai, Ralf, and Silvia. Thank you so much for the valuable comments and suggestions in help of the preparation of my thesis.
A big thank you goes to all present and former members of the group for organizing and inviting to various events and activities outside of work in the last years.
Thank you MinJung for inviting me to Incheon. Also many thanks to you, MinJung, Soyeon, and JongHan for making my time in Korea a wonderful experience.
A big thank you to all the people in the HFE/HF working group and Collaboration for providing me with helpful feedback during the analysis, for conference contributions and during the paper preparation. A special thanks goes to Yvonne, Cris and Shingo for the good collaboration on the publication.
Thank you Denis, Karin, Peter and Sandra for the support on all the non-physics related topics.
I want to thank all people involved in HGS-HIRe/H-QM for the organization of the soft-skill courses and lecture weeks and the provided funding.

Danke Niklas und Marcus, ihr wart immer für mich da.

Curriculum vitæ

Name:	Jan Wagner
Date and place of birth:	31. Mai 1988 in Groß-Gerau, Deutschland
Citizenship:	German

Education

TU Darmstadt, Darmstadt (12/2012 - 09/2016)
Physics, Doctoral candidate (Dr. rer. nat)
Thesis: *Electrons from decays of open charm and beauty hadrons in p-Pb collisions at* $\sqrt{s_{\mathrm{NN}}} = 5.02\,TeV$

TU Darmstadt, Darmstadt (04/2011 - 09/2012)
Physics, Master of Science (M.Sc.)
Thesis: *Polarization studies of J/psi mesons measured with ALICE at the LHC*

TU Darmstadt, Darmstadt (10/2007 - 05/2011)
Physics, Bachelor of Science (B.Sc.)
Thesis: *Energy separation of the 1+/1- Parity doublet in 20Ne*

Immanuel-Kant- Schule, Rüsselsheim (06/2007)
Allgemeine Hochschulreife (Abitur)

Publications with significant contribution

- "*Measurement of electrons from heavy-flavour hadron decays in p-Pb collisions at* $\sqrt{s_{\mathrm{NN}}} = 5.02\,TeV$", Phys.Lett. B754 (2016) 81-93

Conferences and workshops

- "*Heavy flavour multiplicity dependence in pPb with ALICE at the LHC*": talk at Strangeness in Quark Matter 2016 (06/2016), Proceedings accepted
- "*Measurement of electrons from charm and beauty-hadron decays in p-Pb collisions at* $\sqrt{s_{\mathrm{NN}}} = 5.02\,TeV$ *with ALICE at the LHC*": talk at Hot Quarks 2014 (09/2014), J.Phys.Conf.Ser. 612 (2015) no.1, 012031
- "*Measurement of electrons from charm and beauty-hadron decays in p-Pb collisions at* $\sqrt{s_{\mathrm{NN}}} = 5.02\,TeV$ *with ALICE at the LHC*": poster at Quark Matter 2014 (05/2014)
- "*Measurement of electrons from charm and beauty-hadron decays in p-Pb collisions at* $\sqrt{s_{\mathrm{NN}}} = 5.02\,TeV$ *with ALICE at the LHC*": poster at LHCC 2014 (03/2014)

- "*Heavy flavor electron analysis in p-Pb collisions with the ALICE detector at the LHC*": poster at Ecole Joliot Curie (09/2013)
- "*Validity of the VDM in describing the* $\eta \rightarrow e^+e^-\gamma$ *decay process*": research project at HGS-HIRe Summer Student program at GSI (08/2010 – 09/2010)

Erklärung zur Dissertation

Hiermit versichere ich, die vorliegende Dissertation ohne Hilfe Dritter nur mit den angegebenen Quellen und Hilfsmitteln angefertigt zu haben. Alle Stellen, die aus Quellen entnommen wurden, sind als solche kenntlich gemacht. Diese Arbeit hat in gleicher oder ähnlicher Form noch keiner Prüfungsbehörde vorgelegen.

Darmstadt, den October 26, 2016

(Jan Wagner)